

Max-Planck Institut für Kolloid und Grenzflächenforschung

Development of
MWL-AUC / CCD-C-AUC / SLS-AUC
Detectors
for the Analytical Ultracentrifuge

Dissertation
zur Erlangung des akademischen Grades
„doctor rerum naturalium“
(Dr. rer. nat.)
in der Wissenschaftsdisziplin „Kolloidchemie“

eingereicht an der
Mathematisch-Naturwissenschaftlichen Fakultät
Universität Potsdam

von
Engin Karabudak

Potsdam, im Mai 2009

This work is licensed under a Creative Commons License:
Attribution - Noncommercial - Share Alike 3.0 Germany
To view a copy of this license visit
<http://creativecommons.org/licenses/by-nc-sa/3.0/de/deed.en>

Published online at the
Institutional Repository of the University of Potsdam:
URL <http://opus.kobv.de/ubp/volltexte/2009/3992/>
URN [urn:nbn:de:kobv:517-opus-39921](http://nbn-resolving.org/urn:nbn:de:kobv:517-opus-39921)
<http://nbn-resolving.org/urn:nbn:de:kobv:517-opus-39921>

TABLE OF CONTENTS:

CHAPTER 1 : THESIS INTRODUCTION.....	1
CHAPTER 2 : GENERAL REVIEW OF AUC	6
2.1. GENERAL ANALYTICAL ULTRACENTRIFUGATION.....	6
2.2. INSTRUMENTATION FOR COMMERCIAL AUC	8
2.2.1. <i>Mechanical Parts</i>	8
2.2.1.1. Rotors	8
2.2.1.2. Cells.....	9
2.2.2. <i>Electronic Parts</i>	11
2.2.3. <i>Optical Parts</i>	12
2.2.3.1. Absorbance Optics.....	13
2.2.3.2. Interference Optics	14
2.3. THEORY OF ANALYTICAL ULTRACENTRIFUGE.....	16
2.4. OTHER DETECTORS FOR XL-AUC.....	19
2.4.1. <i>Schlieren Optics</i>	20
2.4.2. <i>Fluorescence Detector</i>	21
2.4.3. <i>Turbidity Detector</i>	21
2.5. TYPES OF EXPERIMENTS WITH AUC.....	22
2.5.1. <i>Sedimentation Velocity Experiment</i>	22
2.5.2. <i>Sedimentation Equilibrium Experiment</i>	23
2.5.3. <i>Band (Zone) Centrifugation</i>	24
CHAPTER 3 : STATIC LIGHT SCATTERING DETECTOR FOR ANALYTICAL ULTRACENTRIFUGATION (SLS-AUC).....	26
3.1. INTRODUCTION	26
3.2. EXPERIMENTAL TESTS	27
3.2.1. <i>LAAPD with home-made power supply</i>	27
3.2.2. <i>Modifying the commercial power supply of the LAAPD</i>	29
3.2.3. <i>First Prototype of SLS-AUC</i>	29
3.2.4. <i>Tests with the prototype SLS-AUC</i>	30
CHAPTER 4 : CCD CAMERA DETECTOR FOR THE ANALYTICAL ULTRACENTRIFUGE (CCD- C-AUC)	31
4.1. INTRODUCTION	31
4.2. EXPERIMENTAL TESTS	32
4.2.1. <i>Resolution Test</i>	33
4.2.2. <i>Monochromator of the Optima XL-I</i>	34
4.2.3. <i>Illumination test with SK2048DDE inside AUC with Xenon flash lamp</i>	36
4.2.4. <i>Owl Camera inside AUC with Xenon flash lamp</i>	36
4.2.5. <i>Tests with Constant Light Sources in the Optima XL-I</i>	36
4.2.6. <i>Illumination tests on the Optical Bench with 75 W light</i>	37
4.2.7. <i>Construction of prototype test setup</i>	37
4.2.8. <i>Constant Light Source from Aviv Biomedical</i>	39
4.2.9. <i>Constant Light Source, Test Setup with Monochromator</i>	40
4.2.10. <i>First Prototype CCD-C-AUC, taking UV/Vis spectra</i>	41
CHAPTER 5 : MULTIWAVELENGTH DETECTOR FOR ANALYTICAL ULTRACENTRIFUGE (MWL-AUC)	45
5.1. INTRODUCTION	45
5.2. IMPROVEMENT OF THE MULTIWAVELENGTH DETECTOR.....	46
5.2.1. <i>Flash Lamp</i>	46
5.2.2. <i>Detector Arm and Spectrometer Mount</i>	47
5.2.3. <i>Imaging Optics</i>	48
5.2.4. <i>Optical Tests</i>	48
5.3. RESULTS	49
5.3.1. <i>General Aspects</i>	49
5.3.2. <i>Radial Resolution</i>	52
5.3.3. <i>Wavelength Accuracy</i>	53

5.3.4.	<i>Absorbance Accuracy and Linearity</i>	55
5.3.5.	<i>Intrinsic Noise of the Data</i>	57
5.4.	DISCUSSION	59
CHAPTER 6 : BIOLOGICAL APPLICATION OF MWL-AUC: PROTEIN MIXTURE.....		60
6.1.	INTRODUCTION	60
6.2.	RESULTS AND DISCUSSION	60
CHAPTER 7 : INDUSTRIAL APPLICATION OF MWL-AUC: INVESTIGATION OF B-CAROTENE- GELATIN COMPOSITE PARTICLES.....		67
7.1.	INTRODUCTION	67
7.2.	MATERIAL AND METHODS.....	68
7.3.	RESULTS AND DISCUSSION	69
CHAPTER 8 : APPLICATION OF MWL-AUC IN CHEMISTRY: CDTE NANOPARTICLES.....		76
8.1.	INTRODUCTION	76
8.2.	POLYDISPERSE TGA-CAPPED CdTe NANOCRYSTALS	77
8.2.1.	<i>Experimental</i>	77
8.2.1.1.	Analysis Method of the MWL-AUC data	78
8.2.2.	<i>Results and Discussions:</i>	79
8.2.2.1.	Raw MWL-AUC Data:	79
8.2.2.2.	Analysis without Diffusion Correction	79
8.2.2.3.	Analysis with Diffusion Correction	87
8.2.2.4.	Growth mechanisms of CdTe nanoparticles	89
8.3.	MONODIPERSE TGA-CAPPED CdTe NANOCRYSTALS	98
8.3.1.	<i>Results and Discussion</i>	98
8.3.1.1.	Raw MWL-AUC of a monodisperse sample	98
8.3.1.2.	Determination of CdTe mixture composition by spectrum of the sample.....	98
8.3.1.3.	Comparison of MWL-AUC results and Spectral Deconvolution results	99
CHAPTER 9 : CONCLUSION.....		101
APPENDIX.....		105
ABBREVIATIONS		108
REFERENCES.....		109

List of Figures:

FIGURE 2-1: GENERAL SCHEMATIC FOR AN AUC	6
FIGURE 2-2: ROTORS	8
FIGURE 2-3 : CELL ASSEMBLY OF AUC CELL.....	10
FIGURE 2-4 : VARIOUS AUC CENTERPIECES	10
FIGURE 2-5: ELECTRONICS OF AUC	12
FIGURE 2-6 : SCHEMATICS OF ABSORBANCE OPTICS	13
FIGURE 2-7 : SCHEMATICS OF INTERFERENCE DETECTOR.....	15
FIGURE 2-8: SCHEMATIC OF USER-MADE XL-SO AUC.....	20
FIGURE 2-9: AU-FDS PHOTOGRAPH AND DATA.....	21
FIGURE 2-10: DIFFERENT TYPES OF AUC EXPERIMENT	23
FIGURE 3-1: LAAPD TEST SETUP FOR SLS-AUC	27
FIGURE 3-2: PICTURE OF SLS-AUC DETECTOR PARTS.....	28
FIGURE 3-3: PHOTOGRAPH OF SLS-AUC WHICH IS PLACED IN THE OPTIMA XL-I	30
FIGURE 4-1: SCHEMATIC OF SK2048 DDE LINE CAMERA RESOLUTION TEST	33
FIGURE 4-2 : ORIGINAL TECHNICAL DRAWING OF MONOCHROMATOR OF OPTIMA XL-I (GIEBELER 1992) REPRODUCED BY PERMISSION OF THE ROYAL SOCIETY OF CHEMISTRY.....	34
FIGURE 4-3: TESTING OF SK2048DDE WITH PULSED LIGHT FROM AUC.....	35
FIGURE 4-4: ILLUMINATION TEST OF THE CAMERA ON OPTICAL BENCH	37
FIGURE 4-5: PHOTOGRAPH OF PROTOTYPE TEST SETUP OF CCD-C-AUC	38
FIGURE 4-6: PROTOTYPE CONSTANT LIGHT SOURCE FROM AVIV BIOMEDICAL.....	39
FIGURE 4-7: PHOTO AND DATA OF MONOCHROMATIC TEST OF CCD-C-AUC	40
FIGURE 4-8: CCD-C-AUC FINAL PROTOTYPE SETUP.....	42
FIGURE 4-9: UV/VIS SPECTRA WITH PROTOTYPE CCD-C-AUC	43
FIGURE 5-1: SCHEMATICS OF THE MWL DETECTOR ARM.	46
FIGURE 5-2: PHOTOGRAPHS OF MWL-AUC	47
FIGURE 5-3: INTENSITY DISTRIBUTIONS OF USB2000 SPECTROMETER.....	50
FIGURE 5-4 : OPTICAL TESTS OF MWL-AUC AND OPTIMA XL-I WITH SLIT	51
FIGURE 5-5 : STEP MOTOR TESTS OF MWL-AUC AND OPTIMA XL-I.....	53
FIGURE 5-6 : WAVELENGTH ACCURACY OF THE OPTIMA XL-I AND THE MWL-AUC.	54
FIGURE 5-7: ABSORBANCE ACCURACY OF THE MWL-AUC AT DIFFERENT WAVELENGTHS.....	55
FIGURE 5-8 : INTENSITY PROFILE OF LINEARITY TESTS.....	56
FIGURE 5-9: NOISE COMPARISON BETWEEN THE OPTIMA XL-I AND THE MWL-AUC	57
FIGURE 6-1: COMPARISON OF OPTIMA XL-I AND MWL-AUC IN C(S) AND GLOBAL FIT OF ALDOLASE	60
FIGURE 6-2: THREE WAVELENGTHS, GLOBAL MULTISIGNAL ANALYSIS OF MWL-AUC AND OPTIMA XL-I	61
FIGURE 6-3: REFERENCE INTENSITY OF MWL-AUC AND WAVELENGTH SCAN OF OPTIMA XL-I AND MWL-AUC.....	63
FIGURE 6-4: MWL-AUC AND XL-I ANALYSIS RESIDUALS OF 280 NM ANALYSIS	64
FIGURE 7-1: UV/VIS SPECTRA OF SHELL β -CAROTENE/GELATIN SAMPLE	68
FIGURE 7-2 : STRUCTURE OF β -CAROTENE MICROPARTICLE SYSTEM.....	69
FIGURE 7-3: 3D SEDIMENTATION OF β -CAROTENE MICROSYSTEM	70
FIGURE 7-4: SEDIMENTATION COEFFICIENT DISTRIBUTIONS AT DIFFERENT WAVELENGTHS.....	72
FIGURE 7-5: UV/VIS SPECTRA OF SEDIMENTING β -CAROTENE MICROSYSTEM.....	73
FIGURE 7-6: STRUCTURE MODEL OF THE β -CAROTENE MICROPARTICLE SYSTEM ON THE BASIS OF THE PRESENTED AUC RESULTS.	74
FIGURE 8-1: PRESENTATION OF CdTe EXPERIMENT.....	77
FIGURE 8-2 : RAW MWL-AUC DATA: CdTe NANOPARTICLES SEDIMENTATING WITH BAND CENTRIFUGATION METHOD; (SPEED 55K, 20 RADIAL SCANS 50 μ M STEP SIZE).....	78
FIGURE 8-3 : ANALYSIS OF MWL-AUC DATA, REFERENCE INTENSITY AND PSD	80
FIGURE 8-4: COMBINED 3D DATA, WITH AXIS, PARTICLE SIZE, ABS, WAVELENGTH	82
FIGURE 8-5: SPECTRAL COMPARISON OF SAMPLE	83
FIGURE 8-6: COMPARISON OF THE RESULTS WITH THEORY	85
FIGURE 8-7 : MIXTURE EFFECT OF CdTe	85
FIGURE 8-8 : RESULT OF 2DSA ANALYSIS	87
FIGURE 8-9: DIFFUSION-CORRECTED RESULTS OF THE CdTe EXPERIMENT	88
FIGURE 8-10: DENSITY MODEL OF CdTe/TGA	90
FIGURE 8-11: MOLECULAR WEIGHT OF 24 SPECIES (0-23)	93
FIGURE 8-12: ONE OF THE POSSIBLE MECHANISMS OF CdTe NANOPARTICLE CRYSTALLIZATION	93
FIGURE 8-13: RAW MWL-AUC DATA OF MONODISPERSE SAMPLE.....	97
FIGURE 8-14: SPECTRAL DECONVOLUTION OF MONODISPERSE CdTe SAMPLE.....	99
FIGURE 8-15: COMPARISON OF SPECTRA DECONVOLUTION RESULT AND RAW MWL-AUC RESULTS.....	100

List of Equations:

EQUATION 2-1: CALCULATION OF ABSORPTION	14
EQUATION 2-2: CALCULATION OF THE CONCENTRATION FROM INTERFERENCE FRINGE SHIFT $J(r)$	16
EQUATION 2-3: EQUATION OF CENTRIFUGAL FORCE	16
EQUATION 2-4 : EQUATION OF BUOYANT FORCE.....	17
EQUATION 2-5: EQUATION OF FRICTIONAL FORCE	17
EQUATION 2-6: BALANCE OF FORCES INSIDE AUC	17
EQUATION 2-7: REARRANGEMENT OF EQUATION 2.6.....	17
EQUATION 2-8: EQUATION OF SVEDBERG UNIT	18
EQUATION 2-9: FRICTION COEFFICIENT DUE TO STOKES-EINSTEIN EQUATION	18
EQUATION 2-10: FRICTION COEFFICIENT DUE TO STOKES EQUATION	18
EQUATION 2-11: EQUATION OF PARTICLE SIZE VALID FOR HARD SPHERES.....	18
EQUATION 2-12: LAMM EQUATION.....	19
EQUATION 2-13: S VALUE FORMULA FOR SV EXPERIMENT.....	22
EQUATION 2-14: SITUATION NEEDED FOR SE EXPERIMENTS.....	24
EQUATION 2-15: MOLAR MASS OF THE SAMPLE IN SE EXPERIMENTS.....	24
EQUATION 3-1: SIMPLE MOLAR MASS CALCULATION EQUATION OF STATIC LIGHT SCATTERING	27
EQUATION 8-1: FORMULA FOR CALCULATION OF THE SEDIMENTATION COEFFICIENT.....	79
EQUATION 8-2: CALCULATION OF PARTICLE SIZE FROM THE SEDIMENTATION COEFFICIENT.....	79
EQUATION 8-3: PARTICLE SIZE RANGE CORRECTION EQUATION FOR SMALL PARTICLES AT SCAN 18	82
EQUATION 8-4: SVEDBERG EQUATION.....	90
EQUATION 8-5: CALCULATION OF DIFFUSION COEFFICIENT	90
EQUATION 8-6: FRICTION COEFFICIENT EQUATION	91
EQUATION 8-7: EQUATION OBTAINED FROM FIGURE 8-12	92
EQUATION 8-8: EQUATION OF TOTAL PARTICLE MASS DUE TO GROWTH MECHANISM (FIGURE 8-12).....	95

Chapter 1 : Thesis Introduction

Analytical ultracentrifugation (AUC) has made an important contribution to polymer and particle characterization since its invention by Svedberg (Svedberg and Nichols 1923; Svedberg and Pederson 1940) in 1923. In 1926, Svedberg won the Nobel price for his scientific work on disperse systems including work with AUC. The first important discovery performed with AUC was to show the existence of macromolecules. Since that time AUC has become an important tool to study polymers in biophysics and biochemistry.

AUC is an absolute technique that does not need any standard. Molar masses between 200 and 10^{14} g/mol and particle size between 1 and 5000 nm can be detected by AUC. Sample can be fractionated into its components due to its molar mass, particle size, structure or density without any stationary phase requirement as it is the case in chromatographic techniques. This very property of AUC earns it an important status in the analysis of polymers and particles. The distribution of molar mass, particle sizes and densities can be measured with the fractionation.

Different types of experiments can give complementary physicochemical parameters. For example, sedimentation equilibrium experiments can lead to the study of pure thermodynamics. For complex mixtures, AUC is the main method that can analyze the system. Interactions between molecules can be studied at different concentrations without destroying the chemical equilibrium (Kim et al. 1977). Biologically relevant weak interactions can also be monitored ($K \approx 10\text{-}100 \text{ M}^{-1}$).

An analytical ultracentrifuge experiment can yield the following information:

- Molecular weight of the sample
- Number of the components in the sample if the sample is not a single component
- Homogeneity of the sample
- Molecular weight distribution if the sample is not a single component
- Size and shape of macromolecules & particles
- Aggregation & interaction of macromolecules
- Conformational changes of macromolecules

- Sedimentation coefficient and density distribution

Such an extremely wide application area of AUC allows the investigation of all samples consisting of a solvent and a dispersed or dissolved substance including gels, micro gels, dispersions, emulsions and solutions. Another fact is that solvent or pH limitation does not exist for this method. A lot of new application areas are still flourishing, although the technique is 80 years old. In 1970s, 1500 AUC were operational throughout the world. At those times, due to the limitation in detection technologies, experimental results were obtained with photographic records. As time passed, faster techniques such as size exclusion chromatography (SEC), light scattering (LS) or SDS-gel electrophoresis occupied the same research fields with AUC. Due to these relatively new techniques, AUC began to lose its importance. In the 1980's, only a few AUC were in use throughout the world. In the beginning of the 1990's a modern AUC -the Optima XL-A - was released by Beckman Instruments (Giebel 1992). The Optima XL-A was equipped with a modern computerized scanning absorption detector. The addition of Rayleigh Interference Optics is introduced which is called XL-I AUC. Furthermore, major development in computers made the analysis easier with the help of new analysis software.

Today, about 400 XL-I AUC exist worldwide. It is usually applied in the industry of pharmacy, biopharmacy and polymer companies as well as in academic research fields such as biochemistry, biophysics, molecular biology and material science. About 350 core scientific publications which use analytical ultracentrifugation are published every year (source: SciFinder 2008) with an increasing number of references (436 reference in 2008).

A tremendous progress has been made in method and analysis software after digitalization of experimental data with the release of XL-I. In comparison to the previous decade, data analysis became more efficient and reliable. Today, AUC labs can routinely use sophisticated data analysis methods for determination of sedimentation coefficient distributions (Demeler and van Holde 2004; Schuck 2000; Stafford 1992), molar mass distributions (Brookes and Demeler 2008; Brookes et al. 2006; Brown and Schuck 2006), interaction constants (Cao and Demeler 2008; Schuck 1998; Stafford and Sherwood 2004), particle size distributions with Angstrom resolution (Cölfen and Pauck 1997) and the simulations determination of size and shape distributions from sedimentation velocity experiments (Brookes and Demeler 2005; Brookes et al. 2006). These methods are also available in powerful software packages that combines various methods, such as, Ultrascan (Demeler 2005), Sedfit/Sedphat (Schuck

1998; Vistica et al. 2004) and Sedanal (Stafford and Sherwood 2004). All these powerful packages are free of charge. Furthermore, Ultrascan's source code is licensed under the GNU Public License (<http://www.gnu.org/copyleft/gpl.html>). Thus, Ultrascan can be further improved by any research group. Workshops are organized to support these software packages.

Despite of the tremendous developments in data analysis, hardware for the system has not developed much. Although there are various user developed detectors in research laboratories, they are not commercially available. Since 1992, only one new optical system called "the fluorescence optics" (Schmidt and Reisner, 1992, MacGregor *et al.* 2004, MacGregor, 2006, Laue and Kroe, in press) has been commercialized. However, except that, there has been no commercially available improvement in the optical system. The interesting fact about the current hardware of the XL-I is that it is 20 years old, although there has been an enormous development in microelectronics, software and in optical systems in the last 20 years, which could be utilized for improved detectors.

As examples of user developed detector, Bhattacharyya (Bhattacharyya 2006) described a Multiwavelength-Analytical Ultracentrifuge (MWL-AUC), a Raman detector and a small angle laser light scattering detector in his PhD thesis. MWL-AUC became operational, but a very high noise level prevented to work with real samples. Tests with the Raman detector were not successful due to the low light intensity and thus high integration time is required. The small angle laser light scattering detector could only detect latex particles but failed to detect smaller particles and molecules due to low sensitivity of the detector (a photodiode was used as detector).

The primary motivation of this work is to construct a detector which can measure new physico-chemical properties with AUC with a nicely fractionated sample in the cell. The final goal is to obtain a multiwavelength detector for the AUC that measures complementary quantities. Instrument development is an option for a scientist only when there is a huge potential benefit but there is no available commercial enterprise developing appropriate equipment, or if there is not enough financial support to buy it. The first case was our motivation for developing detectors for AUC.

Our aim is to use today's technological advances in microelectronics, programming, mechanics in order to develop new detectors for AUC and improve the existing MWL detector to routine operation mode. The project has multiple aspects which can be listed as mechanical, electronical, optical, software, hardware, chemical, industrial and biological. Hence, by its nature it is a multidisciplinary project. Again by its nature it contains the structural problem of its kind; the problem of determining the exact discipline to follow at each new step. It comprises the risk of becoming lost in some direction. Having that fact in mind, we have chosen the simplest possible solution to any optical, mechanical, electronic, software or hardware problem we have encountered and we have always tried to see the overall picture.

In this research, we have designed CCD-C-AUC (CCD Camera UV/Vis absorption detector for AUC) and SLS-AUC (Static Light Scattering detector for AUC) and tested them. One of the SLS-AUC designs produced successful test results, but the design could not be brought to the operational stage. However, the operational state Multiwavelength Analytical Ultracentrifuge (MWL-AUC) AUC has been developed which is an important detector in the fields of chemistry, biology and industry. In this thesis, the operational state Multiwavelength Analytical Ultracentrifuge (MWL-AUC) AUC is to be introduced. Consequently, three different applications of MWL-AUC to the aforementioned disciplines shall be presented. First of all, application of MWL-AUC to a biological system which is a mixture of proteins IgG, aldolase and BSA is presented. An application of MWL-AUC to a mass-produced industrial sample (β -carotene gelatin composite particles) which is manufactured by BASF AG, is presented. Finally, it is shown how MWL-AUC will impact on nano-particle science by investigating the quantum size effect of CdTe and its growth mechanism.

In this thesis, mainly the relation between new technological developments and detector development for AUC is investigated. Pioneering results are obtained that indicate the possible direction to be followed for the future of AUC. As an example, each MWL-AUC data contains thousands of wavelengths. MWL-AUC data also contains spectral information at each radial point. Data can be separated to its single wavelength files and can be analyzed classically with existing software packages. All the existing software packages including Ultrascan, Sedfit, Sedanal can analyze only single wavelength data, so new extraordinary software developments are needed. As a first attempt, Emre Brookes and Borries Demeler have developed mutliwavelength module in order to analyze the MWL-AUC data. This

module analyzes each wavelength separately and independently. We appreciate Emre Brookes and Borries Demeler for their important contribution to the development of the software. Unfortunately, this module requires huge amount of computer power and does not take into account the spectral information during the analysis. New software algorithms are needed which take into account the spectral information and analyze all wavelengths accordingly. We would like also invite the programmers of Ultrascan, Sedfit, Sedanal and the other programs, to develop new algorithms in this direction.

Chapter 2 : General Review of AUC

2.1. General Analytical Ultracentrifugation

Analytical Ultracentrifugation (AUC) is a very powerful absolute separation technique that uses centrifugal force to separate particles from each other where particles can be dissolved in a solution or dispersed in a liquid. Macromolecules, proteins, and colloidal systems in solution can be put in the AUC cell and be spun at a controlled rotational speed within the range of 1000–60,000 rpm (rotations per minute) in equipment such as the commercial Beckman Analytical Ultracentrifuge at controlled temperatures. This rotation results in 73–261.580 g ($g = 9.81 \text{ m s}^{-2}$) for a radial position of 6.5 cm (Planken 2008). This force is the key factor for the ability of AUC to separate even small molecules and ions.

As mentioned in first part, Svedberg, who won the Nobel Prize for his work concerning gold nanoparticles and biopolymer, first invented the analytical ultracentrifuge in 1924 (Svedberg 1926). Matthew Meselson and Frank Stahl proved the semi-conservative replication mechanism of DNA owing to an analytical ultracentrifuge (AUC) experiment in 1958 (Meselson and Stahl 1958). A chronological list of important experiments in the history of AUC can be found in (Schachman 1992).

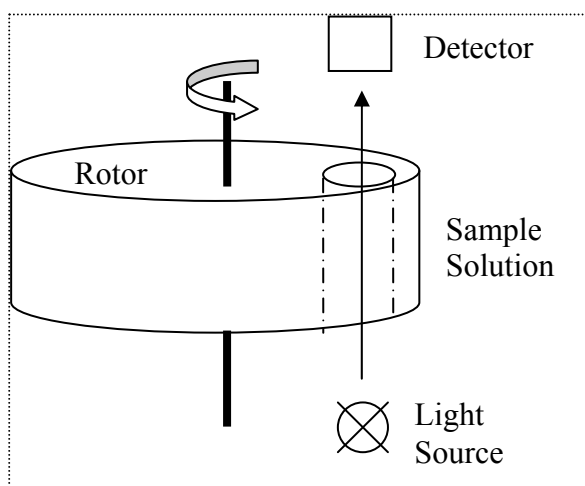


Figure 2-1: General schematic for an AUC

AUC is classified as an analytical instrument because it has optical detectors. The optical detector of AUC relies on visualization of particle concentration in determined radial

position, time and temperature. The light that passes through the AUC cell and reaches the detector and its interaction with the particle that sediment is the basic principle of optical detection. Commercial ultracentrifuges use UV/Vis absorption and interference optics. There are other detectors that have been developed for AUC by various scientists. Turbidity detectors (Mächtle and Börger 2006), fluorescence detector (MacGregor et al. 2004), and Schlieren optics are some other detection systems. In the subsection on Section 2.4, these detectors will be explained in detail.

The general working principle of analytical ultracentrifugation as sketched in Figure 2-1 is as follows: While the rotor is spinning up to 60,000 rpm, the optical detector detects the light that comes from the light source of the detector and passes through the cell. In order to prevent aerodynamic turbulence and friction that come out due to the high rotation speed, AUC works in a vacuum environment. On the other hand, the system, with its all mechanical parts including cells, rotor, motor and optical systems, needs to be precise and vigorous so as to overcome difficulties of vibration and mechanical stretching. These mechanical details are explained in the following subsections of this chapter.

The direct output of an AUC experiment is the radial concentration distribution of the sample at the given time or the time-dependent concentration distribution at given radius. Either of the output is subsequently used to calculate the sedimentation coefficient (S), molecular mass (M) or hydrodynamic radii. Mathematically, the sedimentation coefficient corresponds to the particle speed divided by the acceleration that is applied to the system (Svedberg and Pederson 1940). Molecular mass can also be directly available from the sedimentation equilibrium. In addition, particle size distribution and molar mass distribution can be derived from sedimentation coefficient distribution. The details of deriving the sedimentation coefficient are explained in the subsection 2.3 on the theory of analytical ultracentrifugation.

There are different types of experiments that can be performed with AUC, such as sedimentation velocity, sedimentation equilibrium, zone centrifugation, density gradient, and synthetic boundary experiments. Details of different types of experiments are explained further in this chapter.

2.2. Instrumentation for commercial AUC

From the very beginning, designing and construction of an analytical ultracentrifuge rely on very sophisticated and multidisciplinary engineering problems. First of all, the optical system needs to get data while the rotor is rotating at high speeds up to 60,000 rpm while the motor control electronics keep the fast rotation speed constant. On the other hand, mechanical parts need to cope with enormous gravitational forces. Consequently, while designing an analytical ultracentrifuge, one has to deal with precise optical design, software engineering, and mechanical engineering problems as well as analog and digital electronic problems. In this subsection, the commercial Beckman Optima XL-I is introduced in terms of its mechanics, optics, electronics and software.

2.2.1. Mechanical Parts

Despite all the technological developments, the analytical ultracentrifuge is still a mechanical instrument. Mechanical parts of the AUC are the motor, rotors, cells, and vacuum chamber. The main force that differentiates the particles from each other is centrifugal force which is created by mechanical rotation of a rotor. Among mechanical parts, the rotors and cells needed to be resisted the high gravitational force to which they are exposed due to the rotation.

2.2.1.1. Rotors

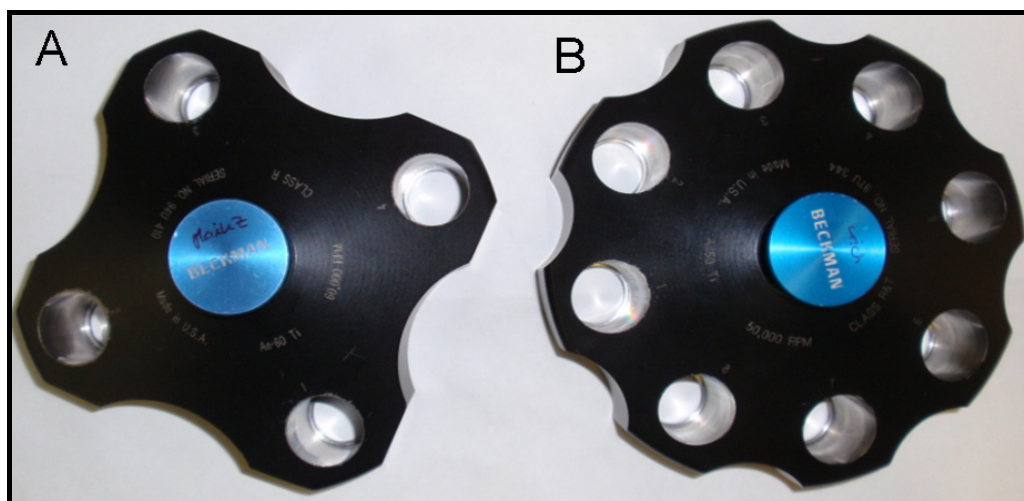


Figure 2-2: Rotors

A: 4-hole rotor; B: 8-hole rotor

The rotor is the most crucial and also risky mechanical part of an AUC. Light needs to pass through the rotor and the sample cell during an experiment. The rotors need to be able to rotate in a range of 1000 rpm to 60,000 rpm (16–1000 rotations per second). If the rotor cannot resist the high level of centrifugal force due to the rotation, or if any crack has been formed in it, the rotor may explode and the mechanical parts of the rotor might skitter like a bomb during the experiment. The most dangerous situation that may happen during an AUC experiment is the explosion of the rotor. Consequently, rotor engineering and testing are among the key engineering tasks of AUC.

Historically, rotors were first made of steel, then of aluminum (Mächtle and Börger 2006). Today, Beckman uses single-piece titanium rotors. There are two types of rotor available, four-hole and eight-hole rotors. These rotors are illustrated in Figure 2-2. One of the holes being used for counterbalancing, a four-hole rotor can take three sample cells and an eight-hole rotor can take seven sample cells. The counterbalance cell is a reference cell that makes radial calibration and angular calibration possible. Radial calibration is performed in order to calibrate the exact radial position for optical detectors whereas angular calibration is used to determine the exact angular position of each cell in comparison to the counterbalance cell during centrifugation.

Four-hole rotors have a speed limit of 60,000 rpm whereas eight-hole rotors have a speed limit of 50,000 rpm. It is important to pay attention to the speed limit because it determines the lifetime of the rotors. The heavy metallic titanium rotors usually expand by up to a couple of millimeters in radius during centrifugation. Such working conditions can form cracks; therefore, after some period of operation all rotors need to be tested by a specialist trained by the manufacturer. Any crack formation is dangerous because it may cause rotor explosions. The Beckman Optima XL-I automatically records each rotor's working history including its operating time at each speed. In addition, users need to keep a log book about history of each rotor's working conditions. These are the most important safety issues for the user.

2.2.1.2. Cells

Cells are the other important mechanical parts of analytical centrifugation. An AUC cell must be able to withstand enormous centrifugal forces. At the same time, it is necessary for a cell to be transparent to light. In addition, a cell needs to hold the sample solution without any leakage which might occur due to the hydrodynamic pressure in the sample cell. Due to this

requirement the sample holder (cell) of the analytical ultracentrifuge is special with respect to other analytical techniques.



Figure 2-3 : Cell assembly of AUC cell

A: Cell housing; B: Window Holder, C: Window liner; D: Window; E: Centerpiece gasket; F: Centerpiece; G: Centerpiece gasket; H: Window; I: Window Liner; J: Window Holder; K: Screw ring gasket; L: Screw Ring

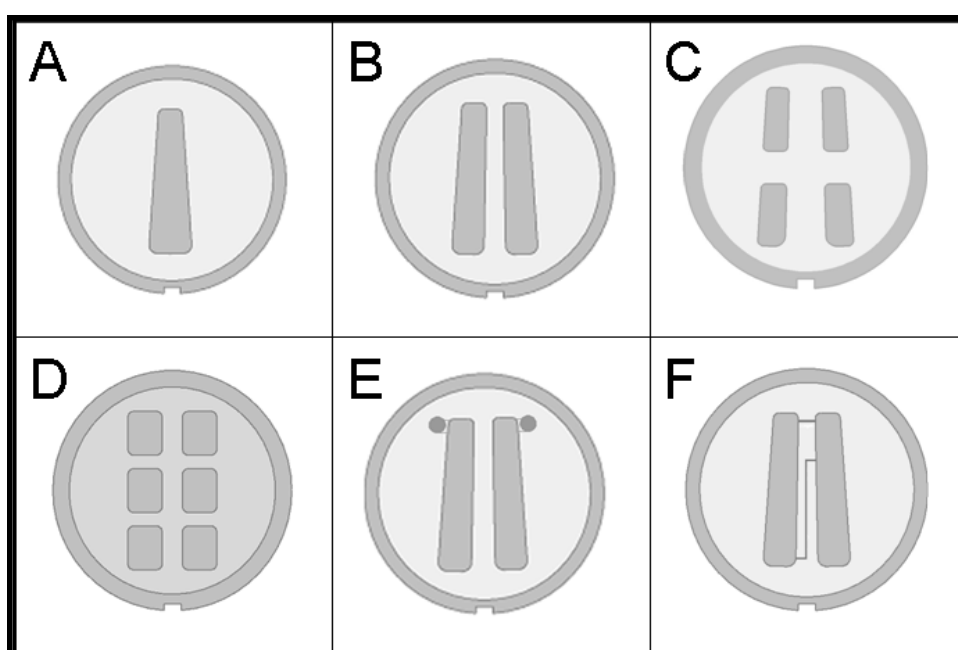


Figure 2-4 : Various AUC centerpieces

A: Single Channel centerpiece; B: Double Sector centerpiece; C: Four-sector equilibrium cell; D: Six-sector equilibrium cell; E: Vinograd cell; F: Meniscus-matching centerpiece designed by Walter Stafford (SpinAnalytical 2008).

From the optical engineering point of view, the cell window is the most important part of the cell. Cell window needs to be transparent to the light and should be resistant to any deformation or breakage, which could occur due to hydrodynamic pressure of the sample solvent. Hence, selection of the material for the cell window is important. The material needs to be strong and transparent at the same time.

Two materials used commercially for cell windows are quartz and sapphire. The usual thickness of windows is about 6 mm. Quartz has a higher UV/Vis transparency and lower cost. Hence, for UV/Vis absorption experiments, quartz is generally preferred. Sapphire windows have greater mechanical resistance and are therefore preferred for interference experiments.

From the scientific and experimental point of view, the centerpiece is the most important part of a cell. Centerpiece design is the most varied mechanical part of the AUC. Scientists have designed and used various different centerpieces for specific usage. (Beams and Dixon 1953; Kegeles 1952; Vinograd et al. 1963) The most common centerpiece is double-sector centerpiece. In this centerpiece, one sector is filled with the sample and the other sector is filled with reference solution. Four- and six-sector centerpieces are used in sedimentation equilibrium experiments. A greater number of sectors allow investigation of more sample solutions in one experiment. Vinograd centerpieces are used to make band centrifugation (Vinograd et al. 1963) where the sample sector is filled with solution of a higher density (density difference must be higher than 0.0001 g/ml) and the reservoir of the Vinograd cell is filled with the concentrated sample. The reservoir is transferred to sample column by centrifugal force via capillaries and layered on the solvent as a thin band allowing that the sample sediments as a band. The meniscus-matching centerpiece was discovered by Walter Stafford and is used to ensure that the meniscus position of the sample and the reference sector becomes identical. Various types of centerpieces are shown in Figure 2-4 .

Material is another important property of centerpieces. Commercially, aluminum alloy, titanium and reinforced epoxy and Kel-F are used for centerpieces. In experiments, the solvent should not react with the centerpiece material. Thus, for different solvents, different centerpiece materials are needed. Before an experiment, the reactivity of different solvents to the centerpiece material must be checked from solvent tables.

2.2.2. Electronic Parts

Electronic parts of the Beckman Optima XL-I include control panel, electronic boards, power supplies, computer connections and the multiplexer. The control panel is required to control the machine manually. An AD/DA card is responsible for controlling the detectors. The control board controls the other functions including vacuum, temperature and speed. The

main board supplies power for the motor, detectors etc. The electronic structure of the Beckman Optima XL- I reflects 1990s technology. Its electronic equipment is quite old in comparison to current technology. The main electronic parts can also be seen in Figure 2-5. The computer connection is used to control the XL-I from a computer.



Figure 2-5: Electronics of AUC

(a) Control panel; (b) Data Acquisition AD/DA board; (c) CRT Control board; (d) Instrument Control Electronics; (e) Computer connection; (f) Detector electronics

The multiplexer unit is another significant electronic unit enabling cell operation. The multiplexer unit is responsible for triggering the Xenon flash lamp or interference laser when a specific cell passes through the light source. The multiplexer measures rotation speed by a hall sensor which receives a signal in each rotation. A small magnet ring is attached to the rotor and when a specific angle of the magnet ring passes through the hall sensor, the sensor produces a signal. The multiplexer also calculates the time to trigger the flash lamp or interference laser.

2.2.3. Optical Parts

Detectors are utilized to detect radial concentration profiles. There exist two commercial optical detectors available; absorbance and interference optics.

2.2.3.1. Absorbance Optics

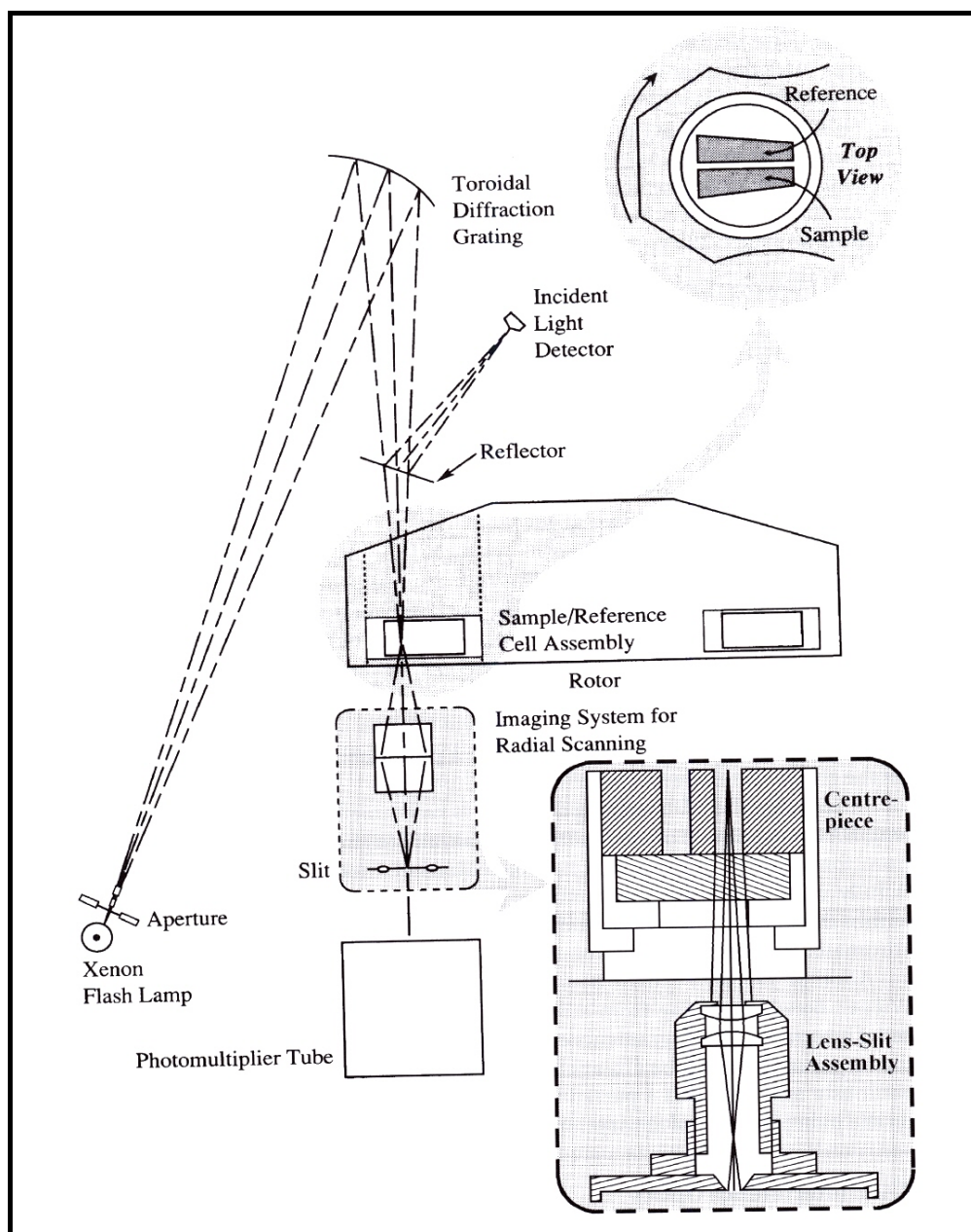


Figure 2-6 : Schematics of absorbance optics

reproduced from (Ralston 1993)

Absorbance optics measures the UV/Vis absorbance in the range of 200 nm to 800 nm. The standard system can only scan one wavelength at once. Therefore, it is necessary to select the wavelength before measurement (Figure 2-6). The system uses a Xenon flash lamp that can flash at 100 Hz. The electronic multiplexer triggers the Xenon lamp when the desired cell

comes under the absorbance optics. Light from the Xenon light source passes an aperture and is reflected by a toroidal diffraction grating. This diffraction grating makes the light monochromatic to the selected wavelength. After that the parallel light passes to a reflector. The reflector reflects 8% of the light it receives to the incident light detector. The incident light detector is used to detect the intensity variations of the Xenon light source between different flashes. An imaging system for radial scanning is used to scan the radial position. Light that passes through a specific radial position is selected by the lens-slit assembly. After the lens-slit assembly, light reaches the detector sub-unit, which is a photomultiplier tube. Afterwards the photomultiplier tube detects the intensity that reaches it. The absorbance is then calculated by the Lambert-Beer Law.

$$A = \lg \frac{I_0}{I} = \varepsilon * c * a$$

Equation 2-1: Calculation of absorption

A : Absorption; I : intensity that passes through sample sector; I_0 : intensity passing through reference sector; ε : extinction coefficient; a : thickness of the cell.

Advantages of absorption optics are selectivity and sensitivity. However limited number of samples can be detected, because samples have to absorb at UV/Vis region in order to be detected. Main drawback of UV/Vis detector is the time that is required to scan the cell, because it scans the cell stepwise.

2.2.3.2. Interference Optics

The interference detector is of interest in terms of its principles. It uses the principle of a Rayleigh interferometer (Lloyd 1974). Monochromatic parallel light passes from double-sector cell (675 nm red laser, 30 mW). Afterwards, the parallel light beams are combined by cylindrical lens to produce the interference pattern, and then the light reaches to a CDD line camera. By this effect, one can detect particles during sedimentation, if the particle forms enough refractive index difference.

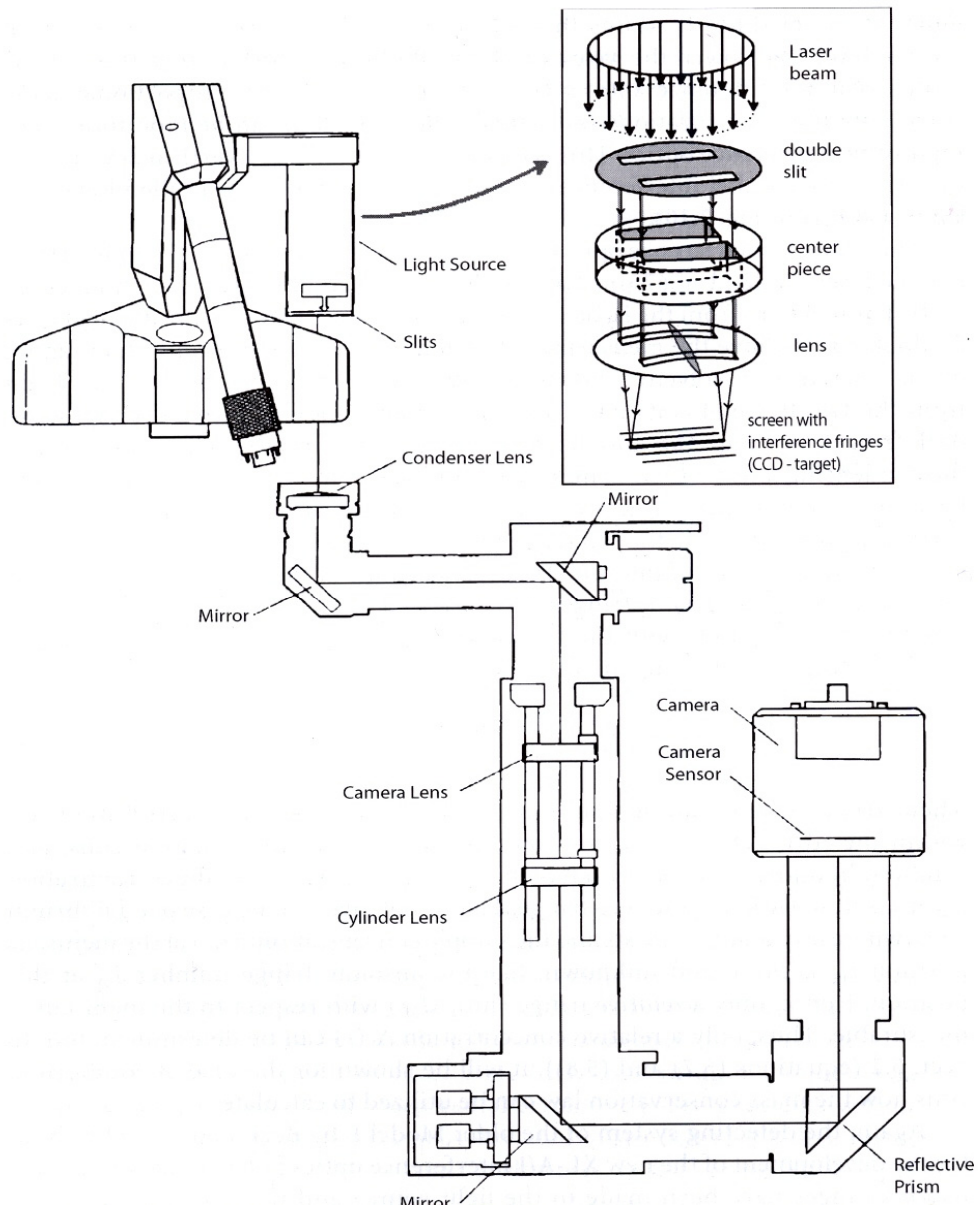


Figure 2-7 : Schematics of Interference Detector

reproduced from (Ralston 1993)

The interference system uses a solid state laser source (675 nm, 30 mW). This solid state laser works inside the vacuum. The laser assembly shapes the laser light and forms two parallel beams. The two parallel beams pass from the double sector cell and reach the condenser lens which is situated between vacuum and air. The system uses four different 90° mirrors, cylindrical lens and camera lens since there is not much space directly under the vacuum chamber. Interference detector sensitivity can be increased by using a lower wavelength laser and replacement of the CCD line camera with a modern one.

At the interference detector, the interference pattern is seen as fringes which shift due to differences in refractive index. If particles sediment and form a refractive index gradient in 6th digit, this can be detected by fringe shift. Concentration of a specific point can be calculated with the help of Equation 2-2.

$$J(r) = \frac{a(dn/dc)}{\lambda} c_r(r)$$

Equation 2-2: Calculation of the concentration from interference fringe shift J(r)

Here Cr: concentration at measured point; λ : wavelength of light; J(r): vertical fringe shift; a: constant relating concentration to fringe shift, $\Delta n = (dc/dt) * c$ = refractive index difference between cells

However, the interference detector is not selective; it detects any refractive index gradient in the cell. This gradient can be formed by a single component system or multi-component system. Sometimes, the density gradient can be formed by the solvent or a salt that is in the solution. Briefly, the key point for an interference detector is selecting the correct reference solvent.

2.3. Theory of Analytical Ultracentrifuge

Particles are confronted with three major types of forces during centrifugation.

1st force: Centrifugal (sedimenting) force F_s given by the equation:

$$F_s = m_p \omega^2 r = \frac{M}{N} \omega^2 r$$

Equation 2-3: Equation of centrifugal force

Where m_p is the mass of particle; ω is angular velocity; r is the radius; M is molar mass of the particle, N is the Avogadro's number.

2nd force: The buoyancy force F_b calculated by:

$$F_b = -m_s \omega^2 r = -m_p \bar{v} \rho_s \omega^2 r = \frac{M}{N} \bar{v} \rho_s \omega^2 r$$

Equation 2-4 : Equation of buoyant force

Where m_s is the mass of displaced solvent; ω is the angular velocity; r is the radius; $\bar{v} = (\rho_p)^{-1}$ is partial specific volume of solute, which is reciprocal of particle density.

3rd force: Frictional force F_f

$$F_f = -fu$$

Equation 2-5: Equation of frictional force

Where f is the frictional coefficient, u is the sedimentation velocity of solute.

These three forces balance each other (Equation 2-6) in less than 10^{-6} seconds (Ralston 1993) and the particle reaches a constant speed.

$$F_s + F_b + F_f = 0$$

Equation 2-6: Balance of forces inside AUC

Or equivalently:

$$\frac{M}{N} \omega^2 r - \frac{M}{N} \bar{v} \rho_s \omega^2 r - fu = 0$$

Equation 2-7: Rearrangement of equation 2.6

Equation 2-7 above can be rearranged to obtain the sedimentation coefficient:

$$\frac{M(1 - \bar{v}\rho_s)}{Nf} = \frac{u}{\omega^2 r} = s$$

Equation 2-8: Equation of Svedberg Unit

The sedimentation coefficient s is called “the Svedberg unit” for honoring the Swedish scientist Svedberg (30 August 1884–25 February 1971). s has a unit of 10^{-13} seconds.

f is a friction parameter of frictional coefficient (f/f_0). It can be written in two equivalent forms. The first form can be derived from the Stokes-Einstein equation as follows:

$$f = \frac{kT}{D} = \frac{RT}{ND}$$

Equation 2-9: Friction coefficient due to Stokes-Einstein Equation

Where D is diffusion coefficient; k is Boltzmann constant; R is gas constant; T is temperature. The second form can be derived from the Stokes equation as follows:

$$f = 3\pi\eta_s d_p$$

Equation 2-10: Friction coefficient due to Stokes Equation

Where d_p is the diameter of particle (Equation 2-10 assumes that the particle is a hard sphere); η_s is viscosity of the medium.

If Equation 2-8 and Equation 2-9 are substituted into Equation 2-10, we obtain:

$$d_p = \sqrt{\frac{18\eta_s s}{(\rho_p - \rho_s)}}$$

Equation 2-11: Svedberg equation of particle size valid for hard spheres

Thus, Svedberg equations (Equation 2-8 and Equation 2-11) are derived for the calculation of sedimentation coefficient and particle size. To fit to the experimental data of AUC, a more

general equation is needed that includes concentration change and diffusion with a parameter of time as well. This equation (Equation 2-12) was derived by O. Lamm (Lamm 1929):

$$\frac{dc}{dt} = D \underbrace{\left(\frac{\partial^2 c}{\partial r^2} + \frac{1}{r} \frac{\partial c}{\partial r} \right)}_{\text{Diffusion term}} - \omega^2 s \underbrace{\left(r \frac{\partial c}{\partial r} + 2c \right)}_{\text{Sedimentation Term}}$$

Equation 2-12: Lamm Equation

The Lamm equation (Equation 2-12) is the main equation that describes the AUC data. There is no analytical solution available to the Lamm equation (Equation 2-12). Therefore, software programs use numerical solutions to the Lamm equation (Equation 2-12) in order to fit the AUC data.

2.4. Other Detectors for XL-AUC

Analytical Ultracentrifugation (AUC) is a very powerful absolute fractionating technique. Like all analytical techniques, Analytical Ultracentrifugation relies on a detection system. In this case, it must allow the visualization of the concentration in the ultracentrifuge cell, namely, the distribution of the solute under study as a function of time and/or radial distance from the centre of rotation. Historically, absorption was among the first principles used to follow sedimentation processes, and was soon followed by systems based on refractometry, including Rayleigh interference, Schlieren optics, and Lavrenko optics (Lavrenko et al. 1999; Schachman 1992; Scholtan and Lange 1972; Svedberg and Pederson 1940). Modern commercial machines (like the Beckman Optima XL-I) are equipped with UV/Vis absorption optics as well as a Rayleigh interference system. The limited detection capacity available imposes practical limitations on exploring all the possibilities of the method, because in principle every kind of sample consisting of a solvent and a dissolved or dispersed phase can be investigated in an AUC. Therefore, development of detectors for Analytical Ultracentrifuges has always been an important issue to expand the capabilities of this powerful fractionating technique. Turbidity optics was developed for the determination of particle size distributions (Mächtle 1992; Müller 1989; Scholtan and Lange 1972).

Fluorescence optics have also been described, one of which has recently become commercially available (MacGregor et al. 2004; Schmidt and Riesner 1992).

2.4.1. Schlieren Optics

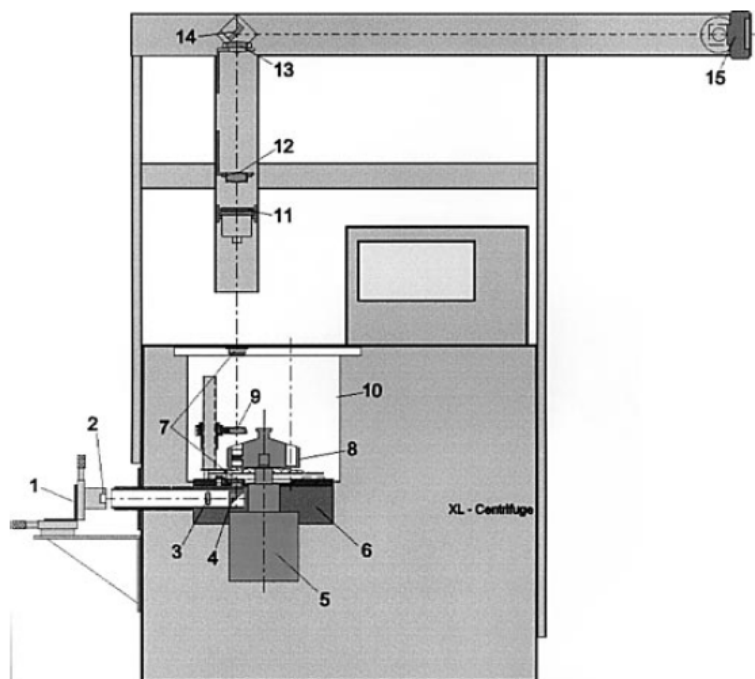


Figure 2-8: Schematic of user-made XL-SO AUC

Physical set-up and optical light path in the XL-SO AUC: 1 flash lamp, 2 Schlieren slit, 3 collimating lens, 4 90° glass prism, 5 XL drive, 6 heat sink, 7 vacuum-sealed window, 8 eight-cell rotor, 9 condensing lens, 10 vacuum chamber, 11 phase plate, 12 camera lens, 13 cylindrical lens, 14 deflecting mirror, 15 70 mm film reflex camera with no objective (reproduced from (Mächtle 1999b)).

Schlieren optics was an existing detector already at the era of Beckman model E Analytical Ultracentrifuge. Nowadays, there is no commercially available Schlieren optics. Some users have developed their own Schlieren detectors for the Beckman XL-I. In Figure 2-8, a user-made Schlieren optics is shown. Schlieren optics is similar in optical components to interference optics, and it has some advantages over interference optics. First, Schlieren optics can work with monosector cells. Secondly, it can detect more acute density gradients than interference optics (Mächtle and Börger 2006). The main advantage of Schlieren optics is the variable sensitivity by variation of the phase plate angle.

2.4.2. Fluorescence Detector

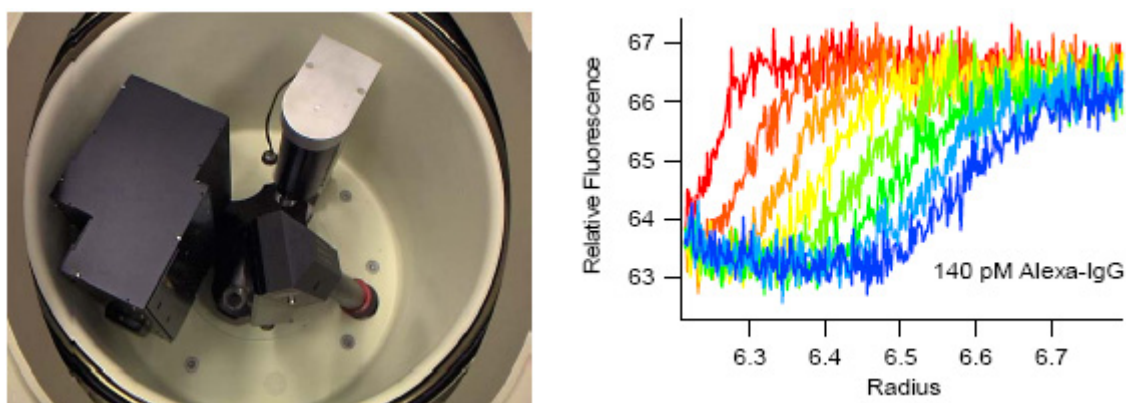


Figure 2-9: AU-FDS photograph and data
reproduced from (AvivBiomedical 2008)

A fluorescence detector for the Beckman XL-I was developed in 2004 (MacGregor et al. 2004). This detector is the first commercial detector in the era of the Beckman XL-I that was not developed and produced by Beckman. The detector was developed commercially by Aviv Biomedical Company. The fluorescence detector detects fluorescence sample with an extreme sensitivity. As it can be seen in Figure 2-9, it can detect up to pico molar range, which is an extreme level that no other detector has ever reached. One has to admit the fact that the main disadvantage of fluorescence detector is its requirement of labeling.

The fluorescence detector system uses a 488 nm CW solid laser for excitation. It collects all wavelengths higher than 505 nm as fluorescence signals. Radial resolution is 50 μm due to spot size. Scan time is about 60 seconds. The system can work as an add-on to existing Beckman hardware and software (AvivBiomedical 2008).

2.4.3. Turbidity Detector

The turbidity detector is not available commercially. To the best of our knowledge, there exist only three user-made turbidity detectors (Mächtle 1984, 1999a). The turbidity detector is like an absorption detector that sits at a constant radial position. The turbidity detector has the advantage of being able to cope with very high concentrations, which is usually the case in industrial colloidal products. The turbidity detector signal should be corrected with the

MIE theory of light scattering, since the light-scattering phenomenon also affects the signal of turbidity.

2.5. Types of Experiments with AUC

2.5.1. Sedimentation Velocity Experiment

In a sedimentation velocity experiment, a sample-filled cell is directly accelerated to the speed where sample notably sediments. The maximum speed limit of the Beckman Optima XL-I is 60,000 rpm. However, the maximum speed for a sample is usually determined by the sedimentation speed of the sample and the detector speed. Absorbance optics takes a scan of a cell in about 1.5 minutes whereas interference optics takes a scan of a cell at about 10 seconds. On the other hand, at least 50 scans should be taken during centrifugation for an efficient data analysis. Hence it is necessary to calculate the optimization of maximum possible speed to make enough scans during sedimentation. In sediment velocity experiments, sedimentation is dominant compared to diffusion. As a result, in the Lamm equation (Equation 2-12), the diffusion term is not very effective.

The sedimentation coefficient (s) and the sedimentation coefficient distribution due to sedimentation velocity experiments can be obtained by using the following formula:

$$s = \frac{\ln(r / r_m)}{\omega^2 t}$$

Equation 2-13: s value formula for SV Experiment

where s is sedimentation coefficient, r is the radius point of measurement point, r_m is the radius of meniscus, $\omega^2 t$ is the time integral.

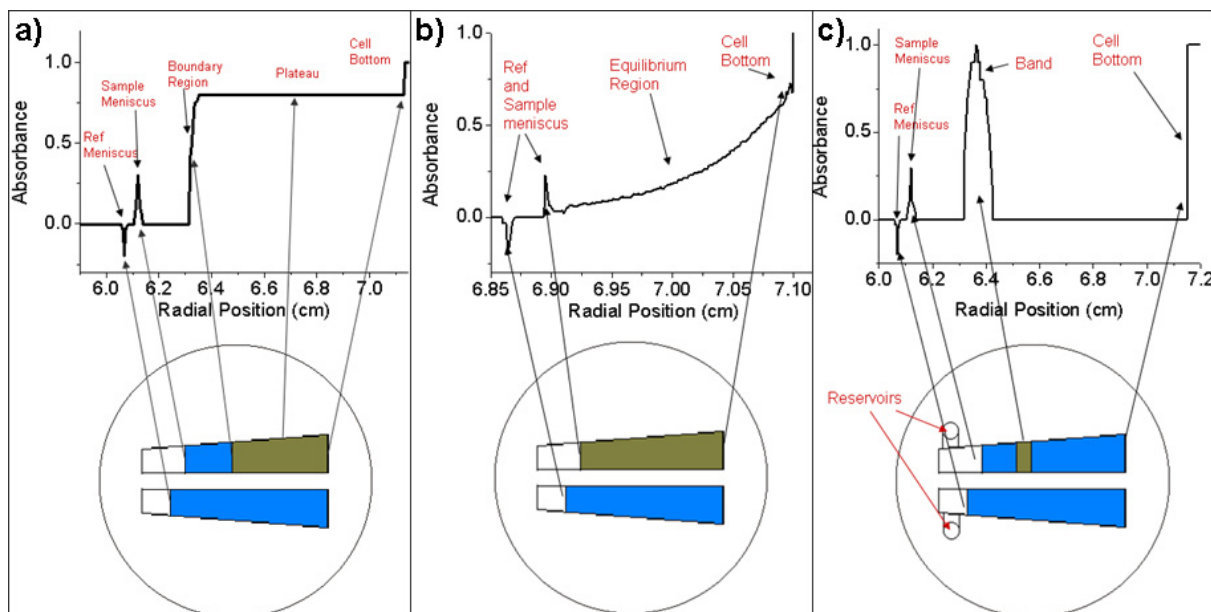


Figure 2-10: Different Types of AUC experiment

a) Sedimentation Velocity; b) Sedimentation Equilibrium; c) Band(zone) Centrifugation

In sedimentation velocity experiments, initially particles are homogeneously distributed to all radial positions. When a centrifugal field is applied to the system, all particles start to sediment in the direction of the radial increase. After exhaustion of particles near the cell meniscus, a boundary is formed. With respect to different sedimentation speeds of different particles, the boundary may be sharp, or wide. Since the experiment finishes after all the particles have sedimented, sedimentation velocity experiments are short experiments in time scale in comparison with sedimentation equilibrium experiments (see 2.5.2). Schematics of such an experiment can be seen in Figure 2-10(a).

2.5.2. Sedimentation Equilibrium Experiment

Sedimentation equilibrium experiments are quite long experiments in comparison with sedimentation velocity experiments, lasting from 10 hours to 200 hours. In this type of experiment, the particle-filled cell accelerates to moderate speeds at which sedimentation is counter-balanced by diffusion. Hence, particles do not sediment fast. One needs to wait until diffusion equilibrates to sedimentation. In long time intervals, scans are taken in order to reach the point where there is no more change in the scan. The schematic of a sedimentation equilibrium experiment is shown in Figure 2-10(b). The final state necessary for sedimentation equilibrium is the state of equilibrium at which there is no longer any change

in the concentration at any radial points. Hence this can be expressed mathematically as follows:

$$\frac{dc}{dr} = 0$$

Equation 2-14: Situation needed for SE experiments

where c denotes the concentration.

Further substituting the conditions of Lamm equation (Equation 2-12), molar mass can be obtained (Equation 2-15).

$$M = \frac{2RT}{(1 - v\rho)\omega^2} \frac{d \ln c}{dr^2}$$

Equation 2-15: Molar mass of the sample in SE experiments

The sedimentation equilibrium experiment is a key experiment for determining the absolute molar mass and the reversible interactions of biological polymers and proteins. Before the invention of gel electrophoresis it was the one of the most important methods to study proteins (Mächtle and Börger 2006).

2.5.3. Band (Zone) Centrifugation

Band (zone) centrifugation is not a commonly used centrifugation method. It was invented by Jerome Vinograd (Vinograd et al. 1963). The schematic of a Vinograd cell centerpiece and experiment can be seen in Figure 2-10(c). In a Vinograd cell, a reservoir is seen, which can be filled with a maximum 15 μ l sample solution. There is a micro-capillary between the reservoir and the sample cell sector. The micro-capillary allows the reservoir to transfer a sample to the sample sector at about 3000 rpm. Hence, while accelerating to maximum speed that sample sediments in required speed, at about 3000 rpm, the sample reservoir is being transferred to the sample column. As particles start to sediment, they start to move in a radial direction. Due to the diversity in their speeds, particles physically differentiate from each

other. Hence, it is band sedimentation rather than being boundary sedimentation, which is the case for sedimentation velocity experiments.

In band centrifugation, particles are physically separated from each other, which could be considered as the most advantageous part of band centrifugation owing to the fact that it allows the user to take the spectra of different species. At each radial position, there is a different particle. Particles are not overlaid to each other as they are at boundary sedimentation.

Chapter 3 :Static Light Scattering Detector for Analytical Ultracentrifugation (SLS-AUC)

3.1. Introduction

AUC is being ideal light scattering device as sample is free from disturbing dust and large sample aggregates. In order to have the advantage of AUC and static light scattering at the same time, we intended to develop a small angle SLS (static light scattering) detector yielding M (molar mass) independent of Θ (scattering angle). Light scattering is a well known technique and a static light detector can detect M and R_g (radius of gyration). On the other hand, AUC technique can give us sedimentation coefficient distribution (S-distribution). Hence, combining AUC and SLS would provide data on M -distribution and S-distribution which also would give diffusion coefficient. As M is proportional to cube of particle size, particle size of particles can also independently determined with both techniques.

Previous tests for developing the SLS detector were performed by Bhattacharyya (Bhattacharyya 2006). Bhattacharyya concluded that for SLS development, intensity must always be taken from the same position of cell window, because cell window scatters the light and its scattering amplitude changes among different positions. So reference intensity can only be taken from the same sector after all sedimentation is finished. Bhattacharyya has used standard photodiode detector to detect scattered light. In order to develop a light scattering detector for AUC, detector is selected as a Large Area Avalanche Photodiode (LAAPD) which was obtained from Advanced Photonix Inc. (California). The part number of the diode is 394-70-74-591, and it has an active area of detection of about 10 mm. Avalanche photodiode has higher sensitivity due to its working principle, that is called avalanche effect.

Our idea is to replace the SLS-AUC with the interference detector (Figure 2-7). In particular, the plan was to replace the laser of the interference system with a new laser whose beam profile is much better. Instead of interference camera and optics, it was planned to construct a SLS-AUC.

$$I / I_o = K_c \overline{M_w}$$

Equation 3-1: Simple molar mass calculation equation of static light scattering

Where I_o is the incident light, and I is the scattered light, K_c is constant depends on setup, $\overline{M_w}$ is the average molar mass

The simplest molar mass calculation of the particle can be calculated using Equation 3-1. K_c needs to be determined for each different setup.

3.2. Experimental Tests

3.2.1. LAAPD with home-made power supply

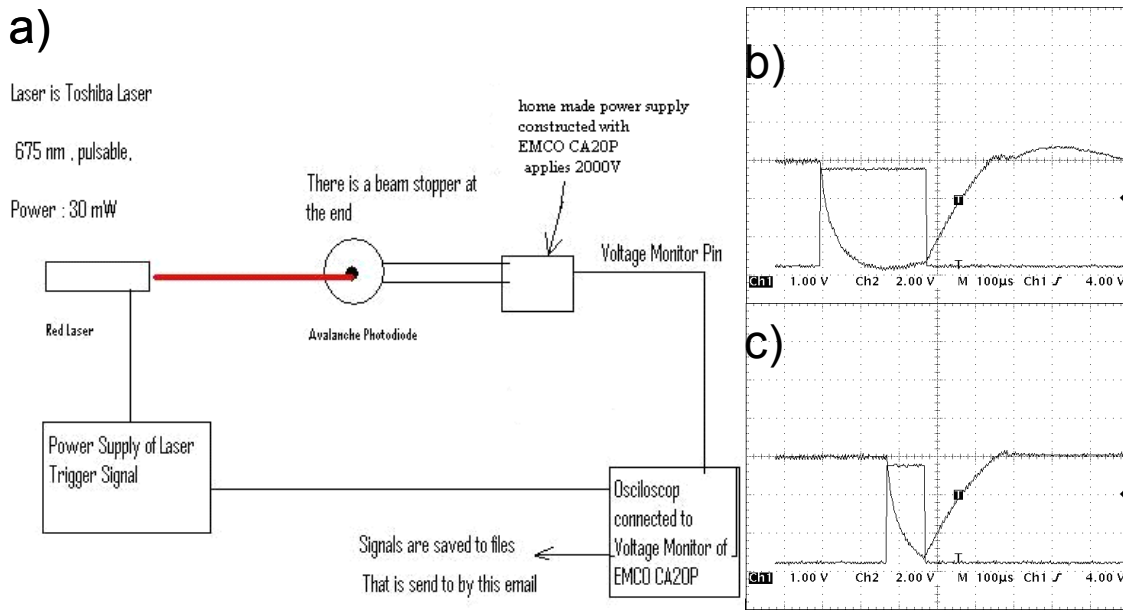


Figure 3-1: LAAPD test setup for SLS-AUC

(a) First design that is tested; (b) Signal read with trigger of 300 μs; (c) Signal read with trigger of 100 μs.

First, setup shown in Figure 3-1(a) was constructed. All the detection system was placed inside the AUC. Home made power supply for the LAAPD is constructed, since the mechanical space restriction in the Optima XL-I did not allow us to use a commercial power supply. The commercial laser of the Optima XL-I had been changed for another pulsed solid-state laser with 675 nm, 30 mW (Toshiba laser) (Bhattacharyya 2006). The optical lens had been replaced by an Avalanche Photodiode (APD). A beam stop was placed at the center of

the APD. An external signal generator triggers both the laser and the LAAPD at the same time. Photodiode is replaced with APD, because APD is more compact and sensitive. Also APD does not need any lens in comparison to photodiode. Therefore optical setup is more reliable and easy to construct.

Figure 3-1(a) shows that the APD does not respond properly to fast light pulses. Figure 3-1(b) and Figure 3-1(c) show the plots of the oscilloscope data. The square pulse plot is the signal from the signal generator that triggers the laser and the LAAPD. The other plot is the signal that is read from the LAAPD. The LAAPD does not respond properly to the signal, although its response time was 18 ns in the datasheet. After discussing the subject with Advanced Photonix, it was decided to send the APD to be tested at Advanced Photonix laboratories in California.

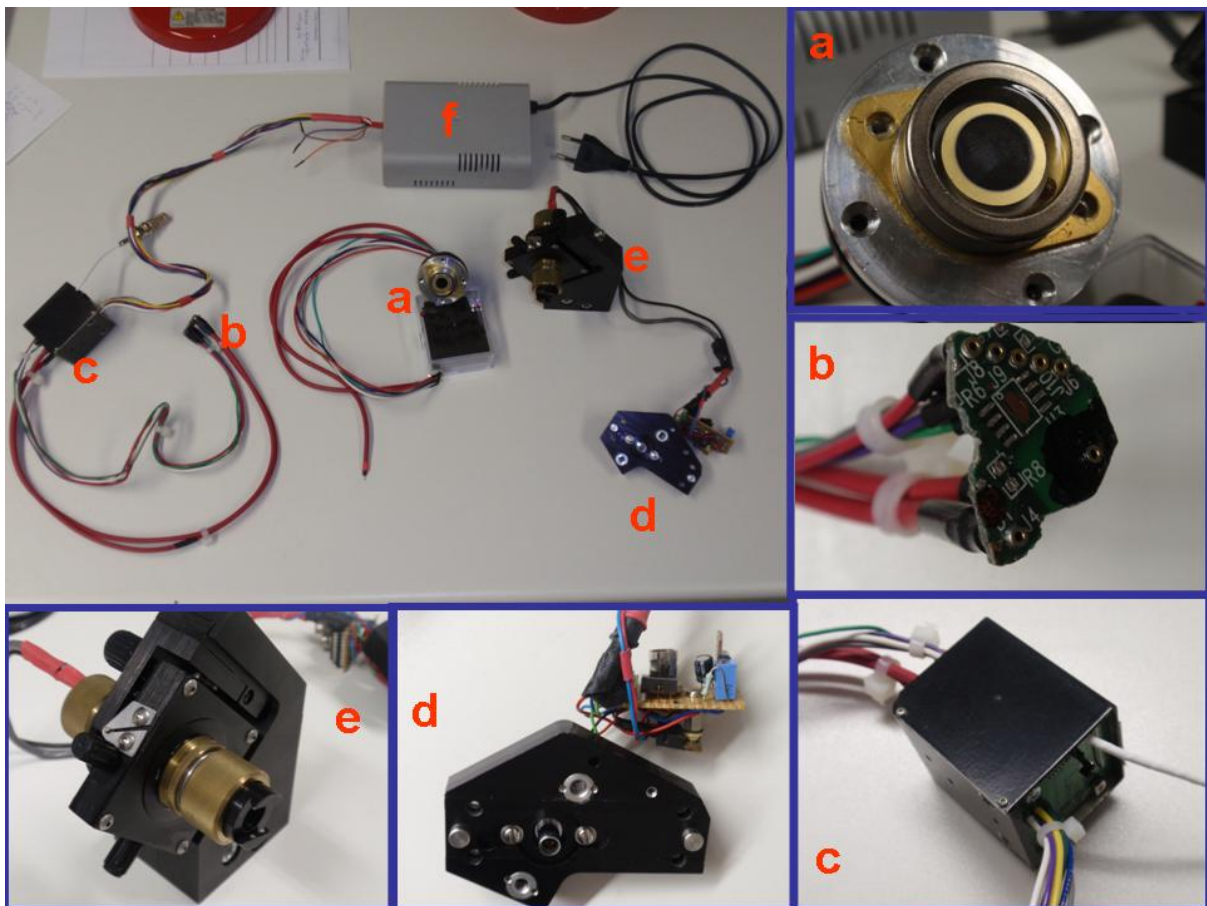


Figure 3-2: Picture of SLS-AUC detector parts

(a) Large Area Avalanche Photodiode attached to the mechanical adaptor of the condenser lens of the interference detector system; (b) Extension board; (c) Commercial high voltage power supply of Large Avalanche Photodiode; (d) Mechanical adaptation and power supply of solid laser; (e) Solid state laser; (f) circuit board that supports power supply of LAAPD.

3.2.2. Modifying the commercial power supply of the LAAPD

After the discussion with the manufacturer of the LAAPD, it was concluded that LAAPD was working properly but the power supply was insufficient. Advanced Photonix offered us an LAAPD with a power supply, but due to the space restrictions in AUC, it decided to have a special modification at the power supply of the LAAPD. The power supply has to be 50 cm away from the LAAPD, since there is not enough space for a power supply if it is directly attached to the LAAPD. With the help of this small modification, LAAPD could be screwed in the place of the condenser lens, with the high voltage power supply outside. However, this modification was not that easy, because the cables need to carry 2000 Volts.

3.2.3. First Prototype of SLS-AUC

Photos of the setup in parts are shown in Figure 3-2. The large picture shows the whole setup, including cables. The Large Area Avalanche photodiode (LAAPD) that is attached to the mechanical adapter is numbered as 1. With this mechanical adaptor the APD can be replaced with a condenser lens of interference optics (Figure 2-7). Five cables of 50 cm are attached to the APD. The ends of these cables can be plugged in to the APD with a specially ordered sit circuit (Figure 3-2(b)). The sit circuit is connected to the commercial high-voltage power supply (Figure 3-2(c)) of the LAAPD with a 50 cm cable. The high-voltage power supply is connected to the low-voltage power supply (Figure 3-2(f)) with another 50 cm cable. Hence, the detector modules which can be plugged in to each other can be replaced with the detector module of the interference optics (Figure 2-7).

The laser assembly is also shown in Figure 3-2. The laser assembly includes a solid laser (Figure 3-2(e)) of wavelength 675 nm with a power of 30 mW. The laser is placed on a mechanical part that can be adjusted according to its x, y and z axes. Together with this mechanical part, the laser can be attached to a mechanical adaptation part (Figure 3-2(e)). With the mechanical adaptation part, the solid state laser assembly can be replaced with the commercial interference laser (Figure 3-2(e)). The power supply of the solid state laser can be seen in Figure 3-2(d).

3.2.4. Tests with the prototype SLS-AUC

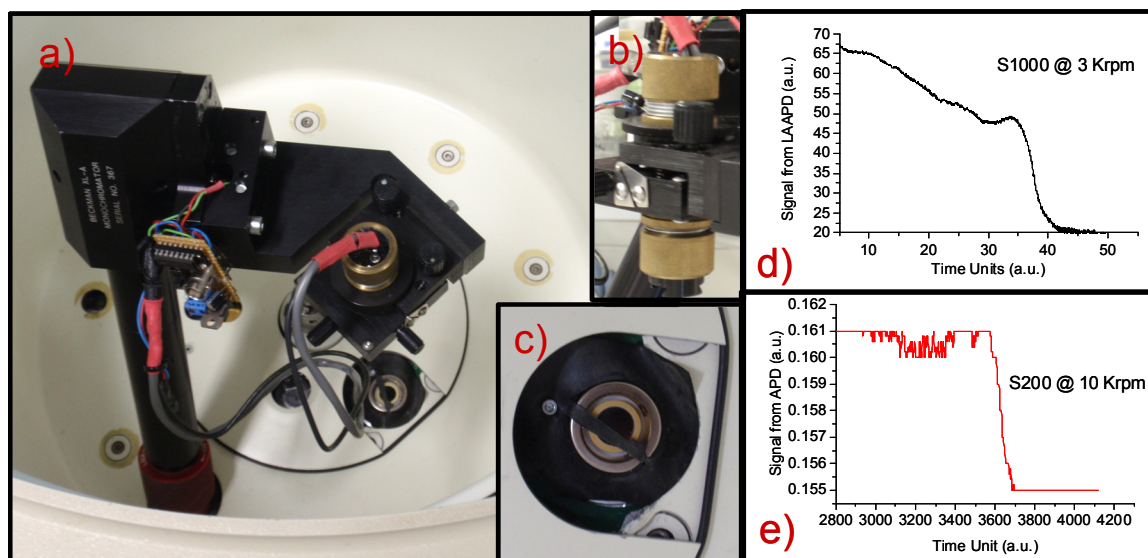


Figure 3-3: Photograph of SLS-AUC which is placed in the Optima XL-I

(a) SLS-AUC detector replaced with the interference detector; (b) SLS laser attached to the test setup (Figure 3-2); (c) Large Area Avalanche Photodiode screwed in place of the condenser lens (Figure 2-7) and covered by beam stopper. (d) Latex particle S1000 sedimenting at 3000 rpm; (e) Latex particle S200 sedimenting at 10,000 rpm.

The first prototype that was built into the Optima XL-I is shown in Figure 3-3. A solid state laser is attached to the monochromator in place of the interference laser. The laser can also be seen from a different side in Figure 3-3(b). The APD covered with the beam stop can be seen in Figure 3-3(c). Some of the data that was taken using this system is shown in Figure 3-3(d). Latex sample S1000 is shown as sedimenting at 3000 rpm (Figure 3-3(d)) and latex sample S200 is shown as sedimenting at 10,000 rpm (Figure 3-3(e)). These data prove that the system is fast enough to obtain data in real AUC working conditions (see section 7.1). Also this data proves that the detector is adaptable to the Optima XL-I. Although detector can detect latex particle sedimentation, protein BSA could not be detected. This shows that the system is not highly sensitive to detecting smaller particles. The main disadvantage of the system is that the cell windows of AUC are very thick (6mm) and also scatters light. (Mächtle and Börger 2006). It is not easy to change the window, because thick windows are needed to overcome high centrifugal forces. Finally, it was decided to improve our system's sensitivity by changing our laser for a more efficient one. For this reason, a green laser has been ordered as scattered light intensity is proportional to λ^{-4} . Further tests are beyond the scope of this thesis. Thus, SLS-AUC has not yet reached its final development. However, the test results shown in Figure 3-3 encourage us by showing that we are on the right track.

Chapter 4 : CCD Camera Detector for the Analytical Ultracentrifuge (CCD-C-AUC)

4.1. Introduction

Development of new detector electronics has motivated us to attempt to use a CCD camera UV/Vis absorption detector for AUC (CCD-C-AUC). The MWL-AUC detector detects all wavelengths at one radial position. The idea of CCD-C-AUC is to detect all radial positions at once which will make it possible to detect high-speed sedimentation and will increase the detection speed of AUC. Successful construction of the CCD-C-AUC will make it possible to detect very fast sedimentation that is not possible with the Beckman Coulter Optima XL-I and will broaden the scope of AUC. Furthermore, very large particles which sediment very fast even at the lowest speed can be detected by CCD-C-AUC. Hence, this will increase the particle-size range of AUC. Secondly, high-speed detection of CCD-C-AUC, will make it possible to see rapid chemical reactions during sedimentation, which is impossible with the Optima XL-I. Therefore, CCD-C-AUC can broaden the scope of current usage of AUC.

Also by faster detection, the time needed for an AUC experiment will decrease, because even at the highest speed, CCD-C-AUC would obtain enough scans in a short time. This is an important parameter for AUC experiments. The experimental time is crucial in AUC and with CCD-C-AUC a higher number of scans can be obtained in a short time.

It is needed to have a detector and light source that can handle the conditions of AUC. To satisfy these requirements, a detector and light source combination needs to have these following properties:

Property 1: To be fast enough.

The detector needs to work within an integration time of 1 μ s. The maximum speed of a rotor is 60,000 rpm, or 1000 rotations per second, so, in the fastest case, one rotation is 1 ms long. One rotation is needed to divide into 1000, in order to gain a signal from a 0.36° sector of a sample. Therefore, in order to catch a cell sector, detector needs to work within an integration time of 1 μ s. Any detector and light source combination needs to work in μ s range.

Property 2: To be sensitive enough

Any detector that will work in μs range needs to be sensitive enough to receive a reasonable signal at that short time scale. The detector may work in μs range, but it does not mean that the signal is meaningful. Hence, the detector needs to be sensitive enough to receive the desired signal from AUC also in the UV/Vis range.

Property 3: To have good resolution

The detector needs to have a spectral resolution of at least $10\text{ }\mu\text{m}$. If the detector detects the cell, ideally it has to have a radial resolution of $10\text{ }\mu\text{m}$, which is the best scan interval of a commercial absorption detector.

Property 4: To be mechanically adaptable to the existing Optima XL-I

The Beckman Coulter Optima XL-I is the only commercial analytical ultracentrifuge in the world at the moment. Therefore, as a last property, any design needs to be adaptable to this device, in terms of mechanical space and vacuum requirements.

These are the properties that are needed for any kind of detector and light source combination. Our aim is to design and test such a detector and light source combination. If these properties are achieved, prototype construction can be possible.

In this chapter, we summarize the tests we performed to construct the CCD-C-AUC. Our final design, the first successful design that has been tested so far, is also presented.

4.2. *Experimental Tests*

The idea of developing a line camera detector began with the Schafter & Kirchhoff SK2048DDE line camera. SK9192D line scan interface was used in order to control the line camera. The line Camera has 2048 pixels and a typical AUC cell is 1.6 cm , so it corresponds to $8\text{ }\mu\text{m}$ resolution. We began our tests using this line camera, since it was the cheapest and easiest option to start with.

4.2.1. Resolution Test

As a first step, we have constructed an optical setup to test the resolution limit of the camera. The system was constructed on an optical bench (Figure 4-1(a)). The system consisted of a white light source and a collimator quartz lens of 40 mm focal length. This lens collimates the white light to a purple single wavelength filter and single wavelength makes parallel light beam. At a distance of 160 mm from the sample, there is a focusing lens (quartz) of focal length 100 mm. This lens images the sample to the line camera.

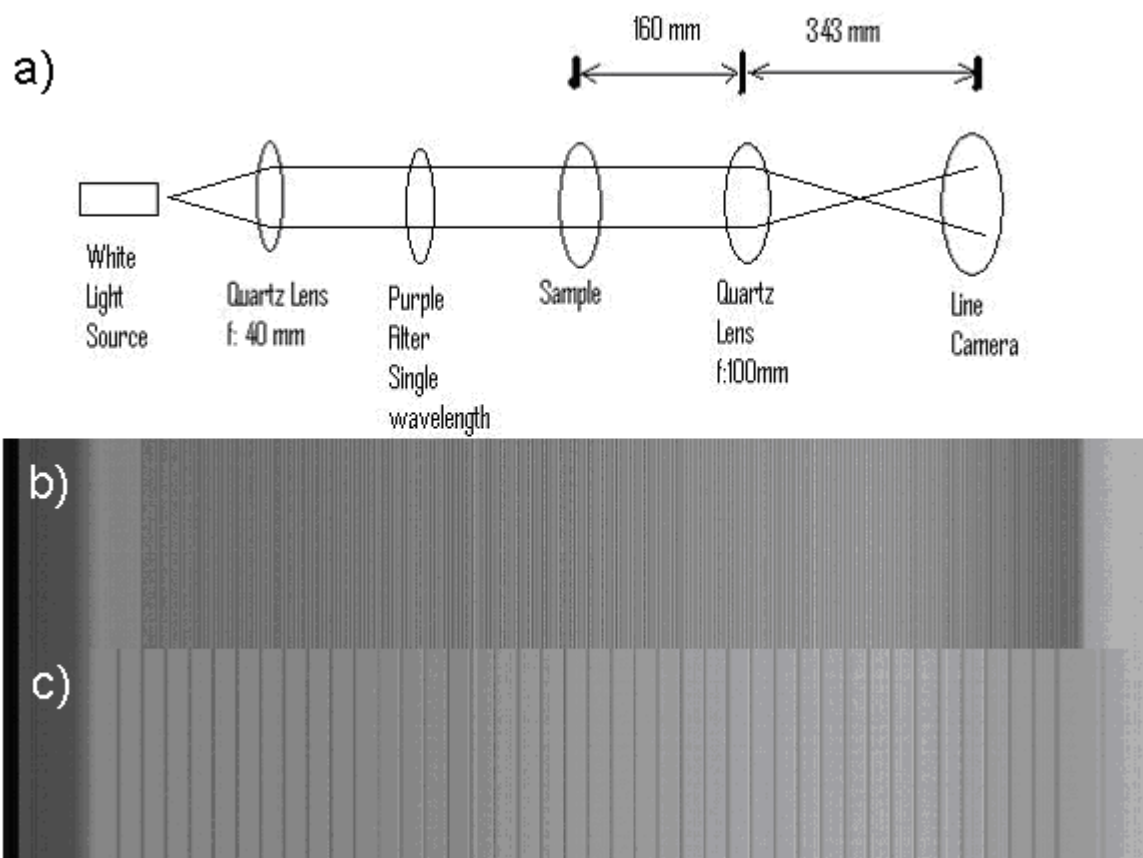


Figure 4-1: Schematic of SK2048 DDE line camera Resolution test

(a) Setup for optical resolution test; (b) SK2048DDE result with 50 μm grid; (c) SK2048DDE result with 500 μm grid.

Instead of the sample itself, we used different sizes of grids to see the resolution of the SK2048DDE line camera. Results with 50 μm grids and 500 μm grids can be seen in Figure 4-1(b) and Figure 4-1(c). The SK2048DDE showed sufficient resolution to be used in AUC. Thus, the resolution test was successful for the line camera SK2048DDE.

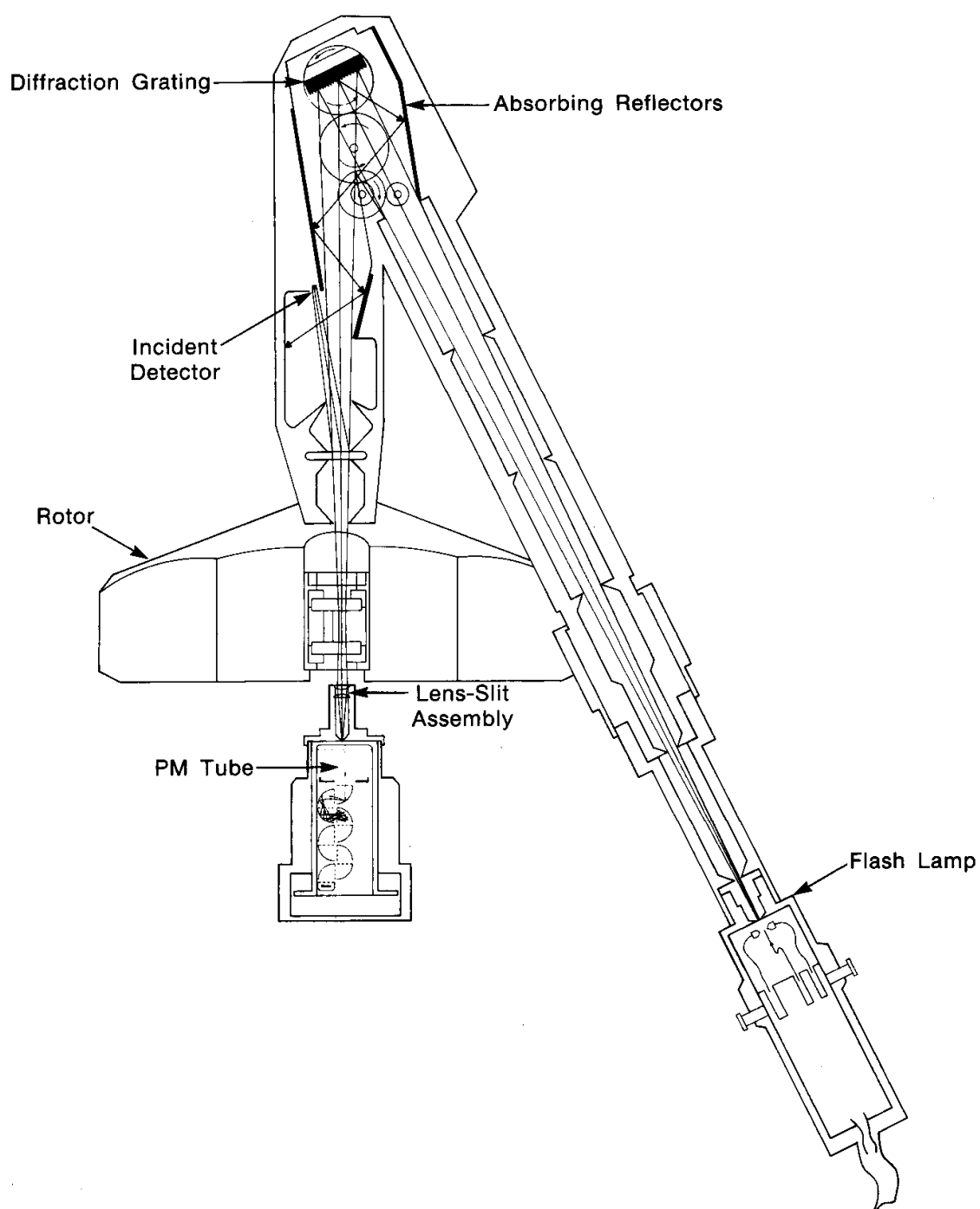


Figure 4-2 : Original Technical Drawing of Monochromator of Optima XL-I (Giebeler 1992)
Reproduced by permission of The Royal Society of Chemistry

4.2.2. Monochromator of the Optima XL-I

Before commencing the resolution test, we needed to focus on the monochromator of the Beckman Coulter Optima XL-I. Our idea was to use the monochromator of the Optima XL-I

absorption optic. This monochromator can be used to select various wavelengths from a white light source. As it can be seen in Figure 4-2, the Xenon flash lamp is attached to the monochromator. Light from the monochromator comes from a pinhole and reaches diffraction grating. After reflection from the diffraction grating, only the selected wavelength can be reflected and reaches the sample. After that, monochromatic light reaches the sample and passes through the sample to the photomultiplier tube.

The first idea was to replace the photomultiplier tube with the line camera plus imaging lens and to construct a line camera detector. In order to do that, we needed to perform a sensitivity test. The weak point of the idea of using a monochromator is that monochromatic light has a very low intensity in the Optima XL-I. Only a small fraction of the illumination from the Xenon light source enters through a small hole to the monochromator. After entering the monochromator, this small portion of the light reaches the diffraction grating. Afterwards, only one wavelength among all the wavelengths in this small portion of light leaves the diffraction grating. The thick windows of the sample cell further decrease the intensity of the incoming light. Hence, the intensity of the light that reaches the detector is extremely small in comparison to the overall optical power of the Xenon light source. Hence, the line camera needs to cope with low light conditions. In order to test this, we have performed illumination tests with the SK2048DDE camera.

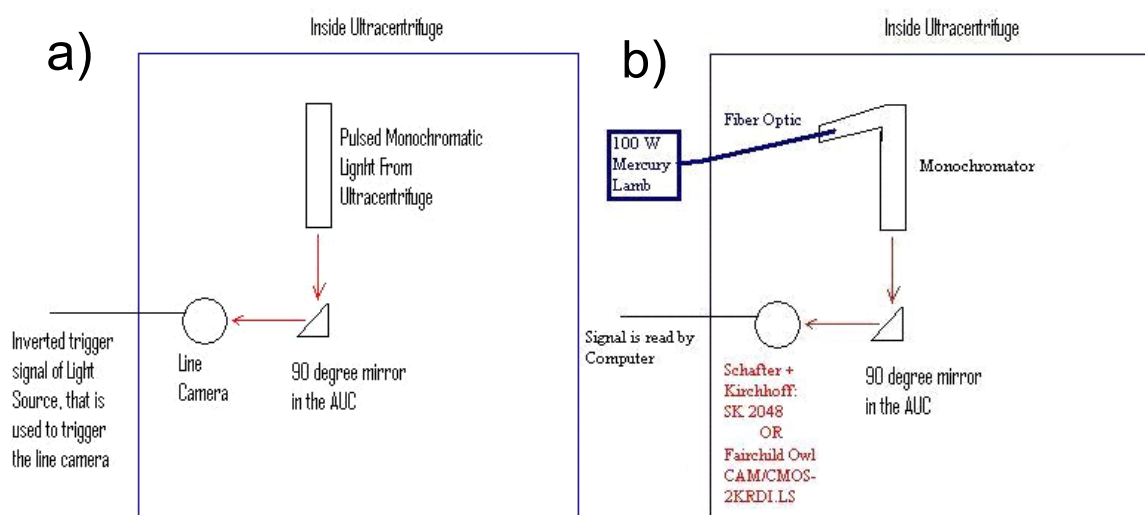


Figure 4-3: Testing of SK2048DDE with pulsed light from AUC.

(a) Setup that is used to sensitivity of line cameras with original Optima XL-I light source; (b) Setup that is used to sensitivity of line cameras with 100 W Mercury fiber-coupled lamp.

4.2.3. Illumination test with SK2048DDE inside AUC with Xenon flash lamp

After the resolution test, we have explored whether we can detect the signal of monochromatic light of the Optima XL-I. In order to test the signal detection limits, we have constructed the setup that is shown in Figure 4-3(a).

We have triggered the line camera with the same TTL pulse with a light source. However, the setup of Figure 4-3(a) has shown us that the intensity of the Xenon light source is not enough to detect via SK2048DDE.

4.2.4. Owl Camera inside AUC with Xenon flash lamp

Fairchild Imaging (Milpitas, California) was contacted, who kindly sent us a Fairchild CAM/CMOS 2KRDI Owl camera to be tested. We have tested the Owl camera within the setup of Figure 4-3(a). However, we could not see any signal even in the longest integration time (5 ms), which implies that there is not enough light intensity. Line cameras do not have any intensifiers.

4.2.5. Tests with Constant Light Sources in the Optima XL-I

As a next step, we tried changing the light source. We have tested the Owl camera and the SK2048DDE with a constant light source a 100 W Mercury lamp. The source was coupled to a fiber. We removed the original Xenon flash lamp of the Optima XL-I and replaced it with the fiber end of a 100 W Mercury lamp. We have tried to detect signals with this setup, which is shown in Figure 4-3(b). We could not detect any signal with the Owl camera and the SK2048DDE. Thus, the problem of low intensity could not be solved with this design. This was most probably due to the low coupling of the fiber to the light source and while the light is focusing to the monochromator. The reason was most probably due to home made coupling of fiber to monochromator arm.

4.2.6. Illumination tests on the Optical Bench with 75 W light

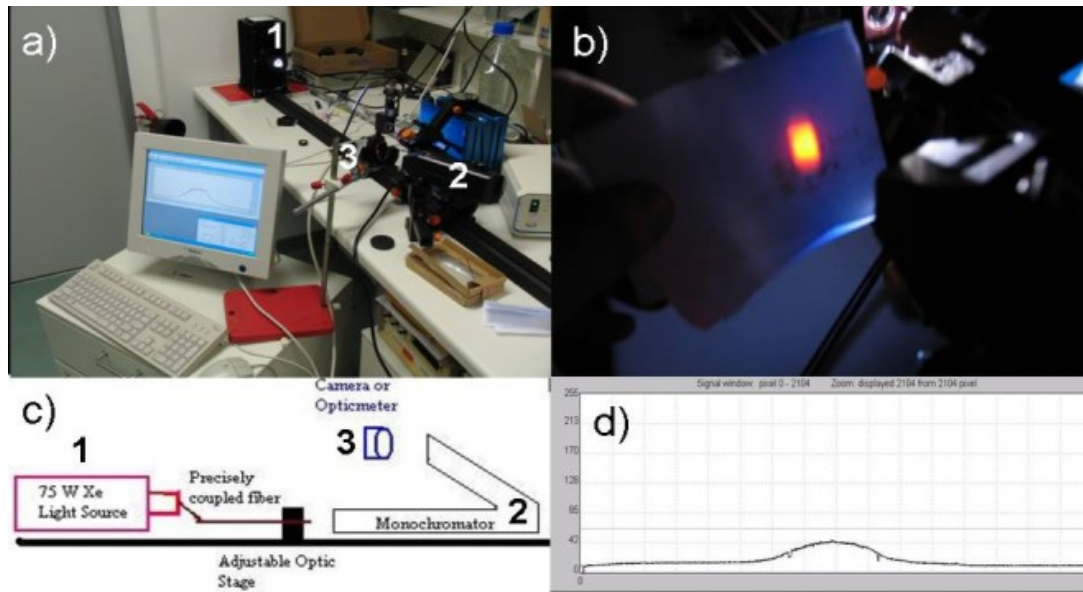


Figure 4-4: Illumination test of the camera on optical bench

(a) Illumination setup; (b) SK2048DDE result with 256 μ s integration time; (c) Schematics of setup; (d) Owl CAM/CMOS 2KRDI result with 25 μ s integration time

In order to solve the illumination problem, we decided to remove the monochromator from the system and test it on an optical bench (Figure 4-4). Schematics of the setup are shown in Figure 4-4(c), with a picture of the output monochromatic light at Figure 4-4 (b). A 75 W Xenon light with a very precisely coupled fiber is used as the light source. The adjustment of the fiber was done with an adjustable optical x-y stage. By using this configuration, with the SK 2048DDE line camera at 25 microsecond integration time, we detected some signal, which is shown in Figure 4-4(d). At 500 nm wavelength, we detected ~ 10 mW of light with the optical power meter as well. So 75 W, Xenon light source has enough intensity, it was decided to buy constant 75 W Xenon light source for AUC from Aviv Biomedical/USA.

4.2.7. Construction of prototype test setup

In order to test the new prototype with the constant light source produced by Aviv Biomedical, we have decided to construct a test setup that will simulate the AUC environment with easily accessible optical bench. The setup that we have constructed is shown in Figure 4-5. Any light source adaptable to the Optima XL-I can be attached to this

system via a light source connector (Figure 4-5(f)). The monochromator of the Optima XL-I can be attached to the monochromator connector that is shown in Figure 4-5(a). The wavelength selection pin can also be seen in the adjustment screw in Figure 4-5, the micrometer to which that pin is connected is labeled as 4. By adjusting this micrometer, a specific wavelength can be selected and determined with a spectrometer. The cell holder is used to simulate the rotor. Thus, a monosector sample cell can be put into the sample holder. The sample cell position can be adjusted by a mechanical x-y stage. There is also a hand-controlled screw to tighten the cell. Under the cell holder, there exists an optical bench. This optical bench includes one lens and one 90° mirror so that it focuses the image of the cell onto the output of the light beam (Figure 4-5(c)). The light source connector used here is identical to the Beckman light source connector. Therefore, any light source compatible with the Optima XL-I can be attached to this connector.

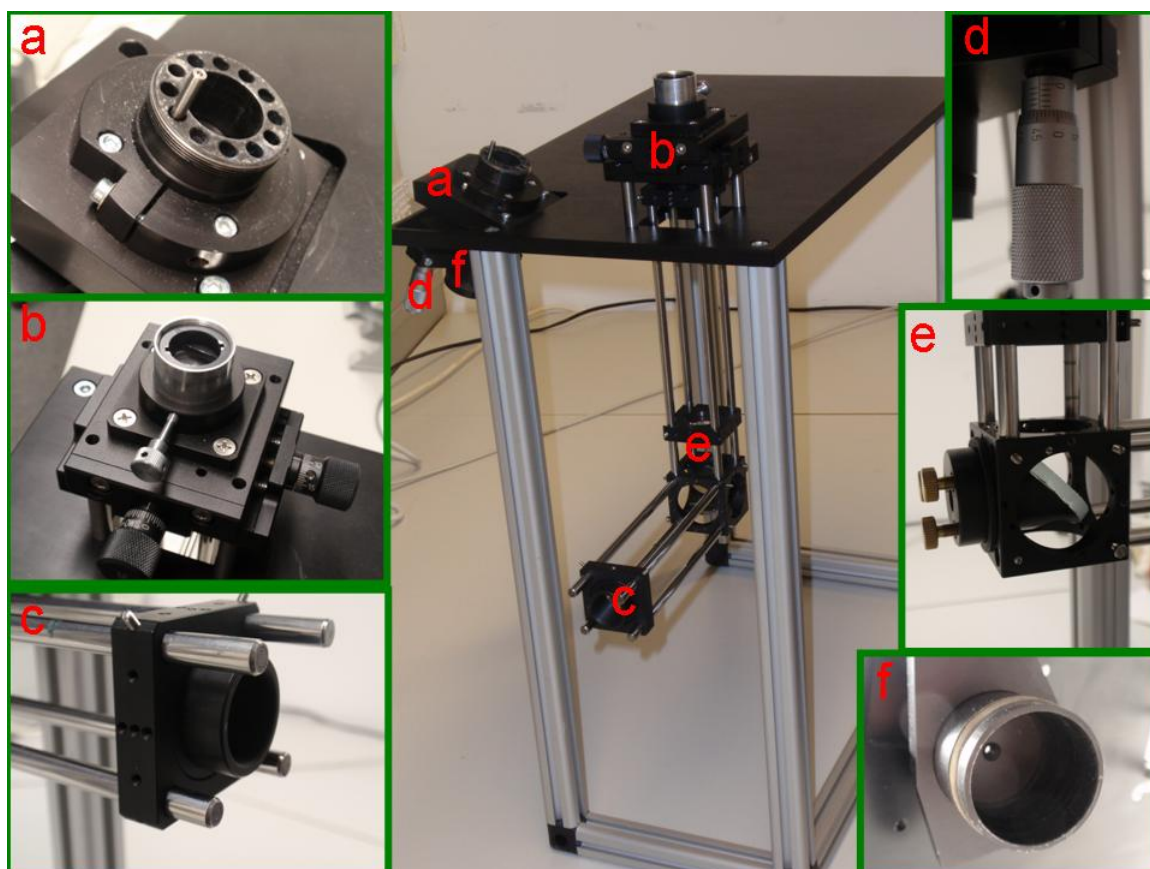


Figure 4-5: Photograph of Prototype Test Setup of CCD-C-AUC

(a) Monochromator connector point with wavelength selection pin; (b) Cell holder assembly; (c) Output of light beam; (d) Micrometer adjustment screw for adjusting wavelength; (e) 90° mirror; (f) Light source connector.

4.2.8. Constant Light Source from Aviv Biomedical

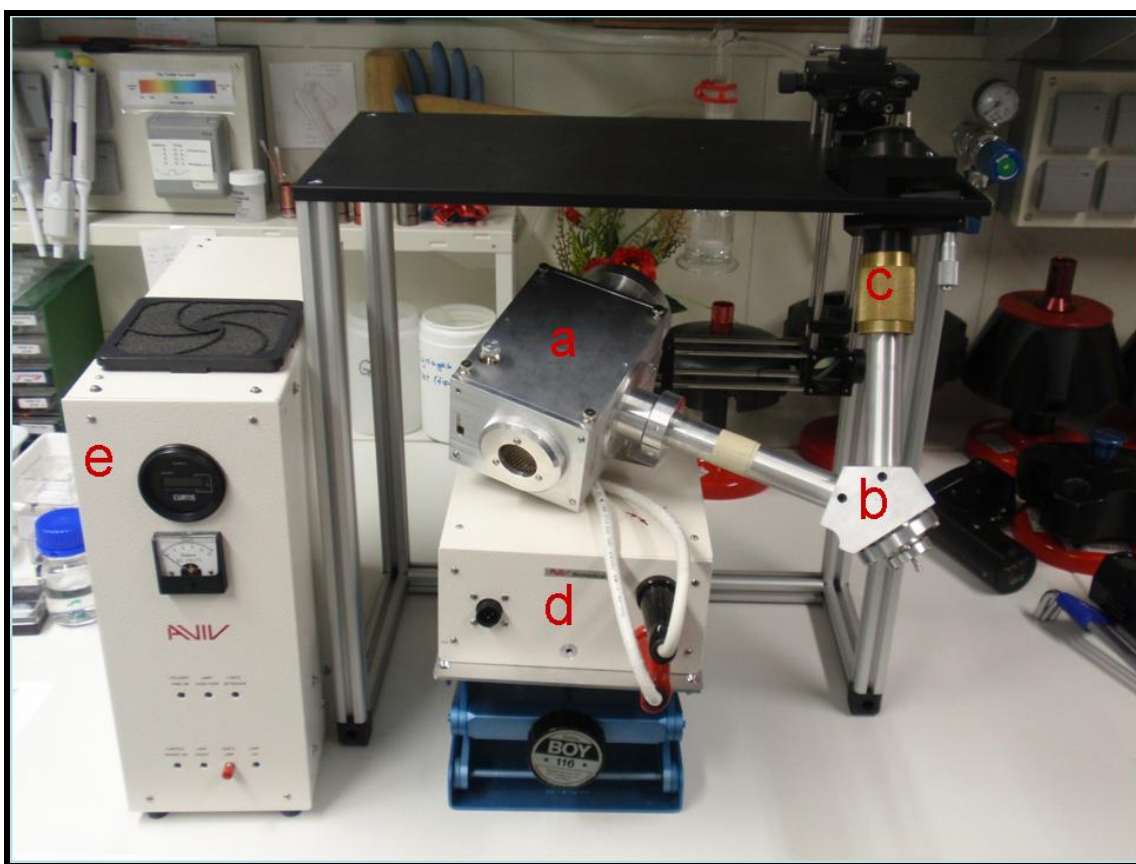


Figure 4-6: Prototype Constant Light Source from Aviv Biomedical

(a) 75 W Xenon light source container; (b) Mirror Assembly; (c) Light connector; (d) Power supply of Xenon light; (e) Controller unit of the system.

As the next step, we aimed to attach our constant light source to our test setup. The constant light source from Aviv Biomedical is shown in Figure 4-6. The Xenon light source container (Figure 4-6(a)) contains the bulb of Xenon light. There is also a cooling system which is not shown here. The mirror assembly (Figure 4-6(b)) contains an adjustable mirror, which reflects incoming light into the pin hole of the absorbance optics with an opening angle corresponding to that of the original flash lamp so that the diffraction grating of the monochromator creates parallel light (the pinhole can be seen in Figure 4-2). Due to the light connector unit (Figure 4-6(c)), the Xenon flash lamp of the Optima XL-I can be replaced by a constant light source. The power supply unit of the light source (Figure 4-6(d)) is responsible for creating the arc inside the Xenon bulb. The controller unit (Figure 4-6(e)) controls the overall system and shows the status of the bulb and power supply. Also the usage of the bulb is monitored by a counter that is existing on the controller. Overall current consumption can be also monitored. With this light source we can continuously illuminate the sample with

parallel light. In the commercial Optima XL-I, the light source is triggered with an electronic signal and it can only flash for 3–4 μs . Furthermore, the flash lamp of the Optima XL-I can only flash at a rate of 100 Hz, so this limits the time interval of measurements. However, with the help of our prototype light source, we can illuminate all cells continuously with parallel light without any time limitation.

4.2.9. Constant Light Source, Test Setup with Monochromator

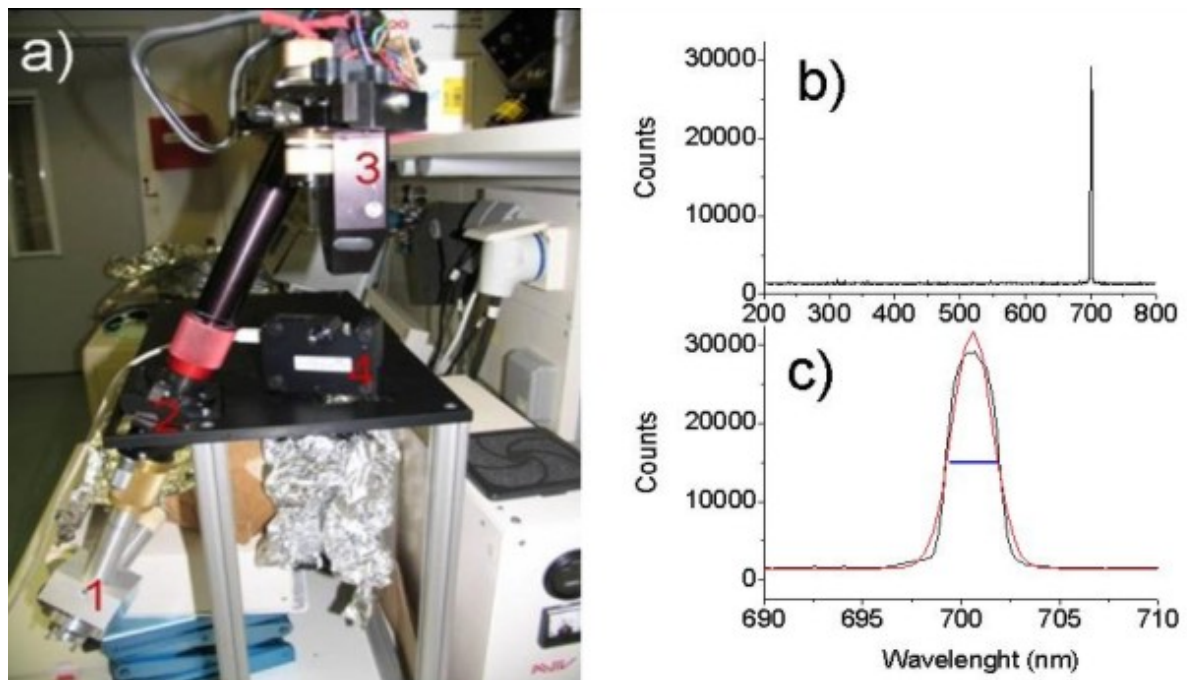


Figure 4-7: Photo and data of monochromatic test of CCD-C-AUC

(a) Monochromator test setup (a1) Aviv Biomedical Constant Light Source; (a2) Test setup; (a3) Monochromator; (a4) USB2000 spectrometer; (b) USB2000 data; (c) zoom in to graph (b); black line: raw data; red line: Gaussian fit to peak b; blue line: FWHM of 4 nm.

In order to test our constant light source, we have constructed the setup shown in Figure 4-7. The continuous light source is attached to the test setup. The light source is covered by aluminum foil in order to prevent the user from any UV exposure. The light source (Figure 4-6) is attached to the light source connector (Figure 4-5(f)). The monochromator of the Optima XL-I (Figure 4-2) is attached to the monochromator connector point (Figure 4-5(a)). The cell holder assembly (Figure 4-5(b)) is replaced by a USB2000 spectrometer (Figure 4-7 (a)). With this setup, it is possible to detect the spectrum of incoming light due to the monochromator which is illuminated by the constant light source. The monochromatic light

that comes from the monochromator can be adjusted manually by a micrometer (Figure 4-5 (d)). This micrometer moves the monochromator pin (Figure 4-5(a)) and this pin adjusts the diffraction grating of the monochromator (Figure 4-2). We have adjusted the monochromatic light close to the value of 700 nm. The intensity reading of USB2000 in counts can be seen in Figure 4-7(b). An enlargement of the peak of Figure 4-7(b) is shown in Figure 4-7(c). The black line refers to the raw data from the USB2000, where the red line is the Gaussian fit of the raw data. The short blue line shows the full width at half maximum (FWHM) of the Gaussian peak. The FWHM of the peak is found to be 4 nm. The FWHM of the absorbance optics of the Optima XL-I is given as 3 nm (Laue 1996). Hence, to obtain a FWHM of 4 nm is a reasonable result for the first experiment performed with a home-made test setup, without any fine adjustment of the optical system. Thus, we conclude that the monochromator works successfully in our setup.

4.2.10. First Prototype CCD-C-AUC, taking UV/Vis spectra

We have tested our already constant light source, test setup and monochromator and obtained reasonable results. Now it is time to test our optical bench with a real sample. After our unsuccessful test with the SK2048DDE and Owl CAM/CMOS2KRDI cameras, we decided to change the camera. The Andor i-star ICCD camera has an optical gate that can be controlled in 2 ns. Hence the camera is much faster than we need. This camera uses cathode tubes to intensify the incoming light. We contacted LOT-Oriel (Darmstadt) as the German supplier of Andor cameras and requested a trial of the Andor i-star ICCD DH734_18mm camera. We received permission to test the camera in our laboratory for one day. We prepared our constant light source, test setup, monochromator, sample cell, sample cell holder, and optical bench before the test. A photograph of the test system with the Andor i-star ICCD camera is seen in Figure 4-8. The light source is attached to the test setup (Figure 4-8(a2)). The monochromator (Figure 4-8(a3)) is attached to the test setup. The last opening of the monochromator is covered by the double slit of the interference optics (Figure 2-7), in order to make the output light very thin and much more monochromatic. We placed a gelatin-filled monosector cell into the cell holder subunit in order to see the meniscus of the sample, because the meniscus cannot be seen with liquid samples in such an orientation. We have adjusted the x-y table of the sample holder. The lens and mirror of the optical setup was been also adjusted in order to transfer the image of the cell into the center of the output of the light

beam part (Figure 4-5). As Andor i-star camera arrived, the lens of Andor i-star camera was placed at the output of light beam.

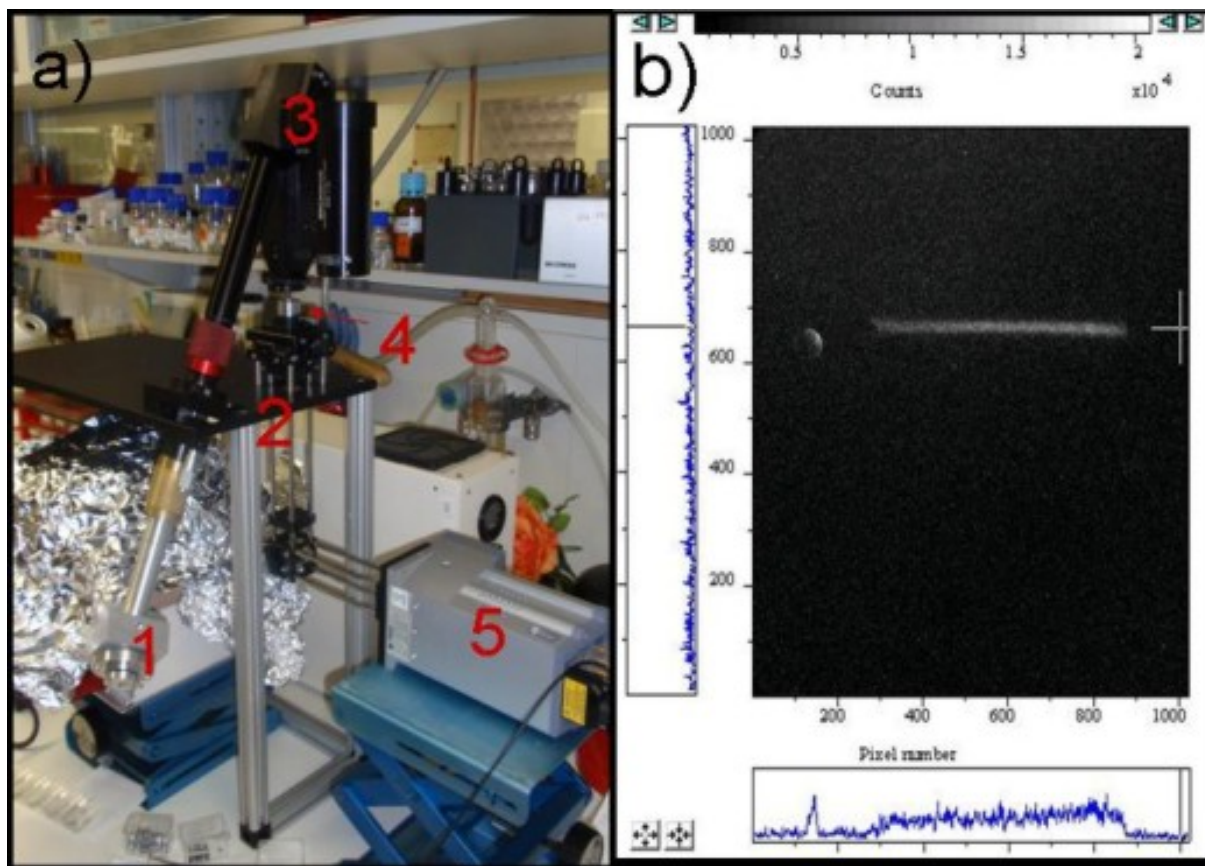


Figure 4-8: CCD-C-AUC final prototype setup

(a) Test setup with Andor Camera; (a1) Constant light source; (a2) Test setup; (a3) Monochromator; (a4) Monosector cell with a gel inside; (a5) Andor i-star DH734_18mm camera; (b) Image of gel-filled sample with integration time of 200 times 0.1 μ s, with wavelength selection of 500nm.

Figure 4-8(b) is a picture of the gelatin sample with 200 integration pulses of 1 μ s length. This picture proves that this design of the CCD-C-AUC detector is sensitive enough to detect the sample. The meniscus of the sample is also seen in the picture. This test setup also proves that the design in Figure 4-8 is fast enough to gain a meaningful signal with 1 μ s integration time. The setup itself proves that CCD-C-AUC can be built mechanically inside the Optima XL-I without any mechanical problem. Adaptation to the Optima XL-I monochromator has been also proved.

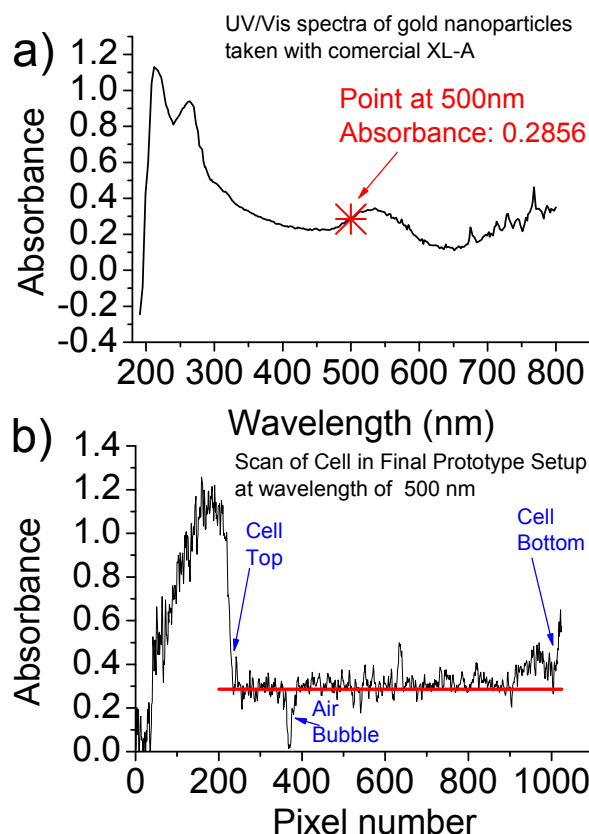


Figure 4-9: UV/Vis spectra with prototype CCD-C-AUC

(a) UV/Vis spectra of solution of gold nanoparticles with Optima XL-I; (b) Absorbance from final prototype CCD-C-AUC setup. Red line is absorbance value that we have measured with the commercial Optima XL-I; cell bottom, cell top and cell bubble can be seen.

As a final test, we tried to gain absorbance data from the CCD-C-AUC final prototype setup. We have prepared a gold nanoparticle solution, and put it into the AUC cell. The spectrum of the solution that is taken by the commercial absorbance optics of the Optima XL-I is shown in Figure 4-9(a). The absorbance value of the Optima XL-I at 500 nm is 0.2856. We then measured the intensity spectra of a water-filled cell and a sample-filled cell in our setup (Figure 4-8) and then calculated absorbance with the help of Equation 2-1.

The result of the absorbance calculation is seen in Figure 4-9(b). Cell bottom and cell top can be recognized easily in this graph. The air bubble is not at the top of the cell because there is no centrifugal force in the setup. It took 200 ms with integration pulses of 1 μ s in intervals of 1 ms to gain the absorbance data. Hence, this time, conditions were identical to the time constraints of the Optima XL-I. The thick red curve shows the absorbance value of 0.2856,

which was measured by the Optima XL-I. Figure 4-9(b) proves that our first prototype design is capable of measuring the absorbance of the sample exactly.

Chapter 5 : Multiwavelength Detector for Analytical Ultracentrifuge (MWL-AUC)

5.1. Introduction

The absorption optical system of the Optima XL-I from Beckman Coulter was introduced in 1991(section 2.2.3.1). It is based on a photomultiplier tube (PMT) which detects light at a single, pre-selected wavelength delivered by a polychromatic flash lamp. This system has remained unchanged since 1991. However, in the intervening years there has been a rapid development in the semiconductor industry. The considerable decrease of the price and the size of semiconductor products (e.g. spectrometers, counter cards, analog to digital converters) and powerful programming techniques make it possible to develop more efficient detectors. Spectrometer technology has made small, cheap, fast and precise detection systems based on CCD arrays which are commercially available. Such a detection used in analytical ultracentrifuge system would expand the possibilities of it, because multiwavelength analysis perfectly suits to the studies of multiple, interacting components (Giebeler 1992) or colloidal particles with size-dependent optical properties (quantum dots or metal nanoparticles) (Cölfen et al. 1997).

Other advantages include: the possibility of a considerable reduction in experimental time, even for a limited number of wavelengths, without a loss of information due to the very fast detection, which is as short as 10 μ s with modern spectrometers. Accordingly, there is the possibility of data averaging, and a fast detection speed for quickly sedimenting samples. If such a spectrometer could be built into a preparative ultracentrifuge, the potential price for a functional analytical ultracentrifuge is promising. Attempts to adapt such spectrometers to the special situation of the ultracentrifuge have recently been described (Bhattacharyya 2006; Bhattacharyya et al. 2006) and hold promise for future applications. The obvious advantages of multiwavelength detection were already described for the first- generation detector, together with some measurement examples and basic system performance (Bhattacharyya 2006; Bhattacharyya et al. 2006).

In this chapter, some modifications made to the original first- generation detector designed by Bhattacharyya *et al.* (Bhattacharyya 2006; Bhattacharyya et al. 2006) will be described and the performance of the current second-generation prototype design as compared with the

commercial system available in the Optima XL-I will be reported. Thus, current limitations will become apparent, indicating directions for further improvements

5.2. Improvement of the multiwavelength detector

The prototype machine, the MWL-AUC, of the first generation (Bhattacharyya et al. 2006) has been modified by simplifying the already existing hardware (Bhattacharyya 2006; Bhattacharyya et al. 2006) as described below.

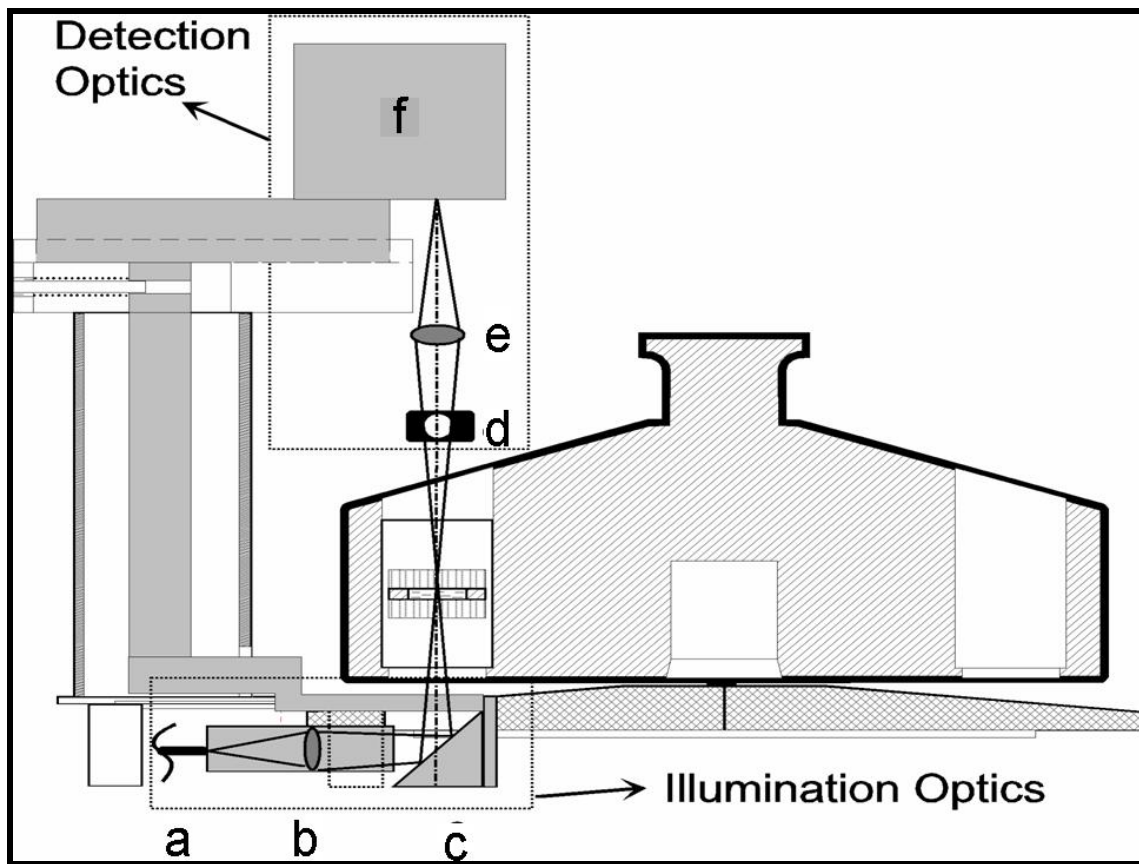


Figure 5-1: Schematics of the MWL detector arm.

a. 600 μm patch fiber UV/Vis (Ocean Optics), b. The collimating lens system (self built), $f=20.6\text{mm}$ biconvex, c. 90° Quartz Prism, d. Iris Diaphragm for reducing light intensity, e. Focusing biconvex lens (40 mm), f. Spectrometer. The light path is also shown schematically.

5.2.1. Flash Lamp

The original flash lamp of the Optima XL-I (Hamamatsu L4633-01) with a maximum repetition rate of 100 Hz and a self-built fiber coupling (Bhattacharyya et al. 2006) was replaced by a faster Xenon flash lamp module (high power Xe flash lamp L-9456-12 from Hamamatsu Phototonics GmbH, Herrsching, Germany, and a suitable power supply) which

can be directly coupled into an optical fiber via an SMA 905 adapter. It has a maximum flash rate of 530 Hz which increases the repetition rate by more than five times which results in a possible scan repetition speed of < 2 ms. The standard deviation of the light intensity as stated by the manufacturer is 1.5%. Low flash-to-flash intensity variation is important as the system does not have an intensity normalization routine.

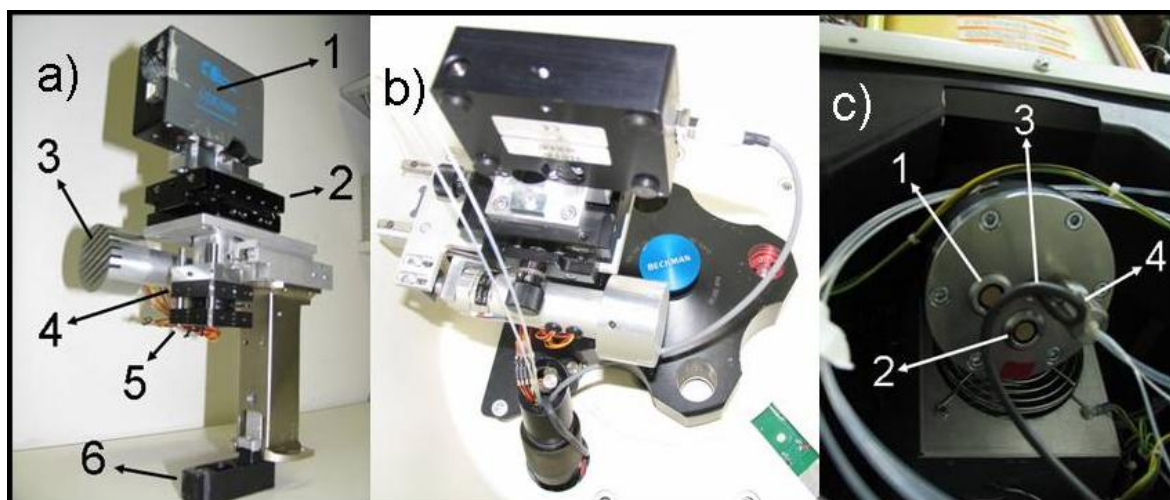


Figure 5-2: Photographs of MWL-AUC

(a) Photograph of the detector arm: 1. Spectrometer, 2. Table with the possibility of x-y movement, 3. Step motor, 4. Lens (40mm biconvex), 5. Iris 6. 90° quartz prism. (b) The arm fitted in the centrifuge. (c) Photograph of the vacuum feedthrough: 1. Electronic feedthrough for step motor, 2. Electronic feedthrough for spectrometer, 3. Electronic connection for TTL pulse for rpm measurements, 4. Optical feedthrough for fibers.

5.2.2. Detector Arm and Spectrometer Mount

In the first-generation setup, the light from the flash lamp was coupled with the centrifuge via an optical fiber and a vacuum feedthrough. It passed the measurement cell and was imaged onto a 25 μm or 50 μm slit. Then it was fed back into a fiber out of the centrifuge until it reached the entrance slit of the spectrometer (typically 25 μm). The disadvantage of this setup was that the light had to pass two narrow slits, which significantly limited the light intensity available at the detector. We have improved the design in the second-generation detector in such a way that the UV/Vis spectrometer entrance slit (Ocean Optics, USB 2000) is now mounted on top of the detector arm at the focal position of the collimating lens where the light was coupled into the fiber again in the first-generation design. The new setup is shown schematically in Figure 5-1. The advantage of this setup is the combined use of the spectrometer entrance slit (25 μm) as the radial and wavelength aperture for the spectrometer.

In this way, a much higher intensity can be obtained at the detector. The maximum intensity can actually be so high that the spectrometer is saturated over the entire wavelength detection range. This makes the application of an iris necessary limit the light intensity (4 in Figure 5-1). The entire setup of the second-generation detector arm is still modular – it can fit into every preparative and analytical Beckman ultracentrifuge. Actually, the described detector design is a modular replacement of the XL-I UV/V is absorption optics. Due to the reversible detector setup, the detector can be exchanged for the Optima XL-I detector within one hour. The hardware of the detector arm with mounted spectrometer is shown in Figure 5-2 as well as the mounted detector arm in the ultracentrifuge. The socket of the flash lamp was replaced by a mount for vacuum feedthroughs for fibers and cables as a hardware module for vacuum feedthroughs (Figure 5-2(c))

5.2.3. Imaging Optics

In order to simplify the optical alignment, the optical path has been simplified as well: instead of two collecting lenses as it is in the original first-generation design ($f=20$ mm, biconvex and $f=15$ mm, biconvex) (Bhattacharyya et al. 2006) or the two biconvex lenses of $f=60$ mm and $f=12.5$ mm described in (Bhattacharyya 2006), only one biconvex lens ($f=40$ mm) has been used at a position optimized *ex centrifugo* on an optical bench to image the centre of the ultracentrifuge cell onto the detector slit to allow a simplified detector alignment. This minimizes chromatic aberration problems, which are inevitably associated with the use of lenses for white light as well as the optical alignment procedure of the detector itself.

Briefly, the second-generation detector has a faster, more powerful flash lamp that is combined with an improved hardware optical arm design, allowing a much higher light intensity and a much simplified optical alignment than the first-generation detector (Bhattacharyya 2006). All lenses were purchased from LINOS Photonics GmbH (Göttingen, Germany).

5.2.4. Optical Tests

In order to determine the wavelength accuracy of both optical systems, an Ho_2O_3 -centerpiece was used (as supplied with the original purchase of the Optima XL-I AUC from Beckman Coulter, Palo Alto, California). Characteristic sharp peaks were expected (among others) at 361/446/537 nm (BeckmanCoulter 1991). For determining the accuracy of the absorbance

readings at different wavelengths, two kinds of reference solutions were prepared. For measuring data at 302 nm, solutions of KNO₃ (Sigma) at various concentrations were freshly prepared in water. Solutions of universal indicator pH 4-10 (Merck, Darmstadt, Germany) were prepared in buffer solution of pH 4 (Metrohm, Herisau, Switzerland). These were measured at 525 nm in the Optima XL-I and MWL-AUC. These solutions were then measured on a benchtop spectrometer (lambda 2 UV/Vis-spectrometer from Perkin Elmer, Überlingen, Germany), the Optima XL-I and the MWL-AUC. To obtain a measure of the precision of the data, we recorded radial scans and averaged them over the entire length of the solution column. No averaging was performed for the single data points. For the measurements with the benchtop spectrometer, data points were recorded every 500 ms over a total time of 60 s and averaged. Mean values and standard deviations thus obtained are reported. Data were normalized to compensate for different optical path lengths (12 mm for analytical ultracentrifuges and 10 mm for the benchtop spectrometer).

To determine the intrinsic noise and the baseline accuracy of the data at different wavelengths, an empty hole of a rotor was flashed with 1, 10 and 100 points averaging over the entire range of wavelengths available. Wavelength resolution was set to 1 nm for the Optima XL-I. All measurements were performed at 3000 rpm in a fully evacuated centrifuge chamber at 25 °C. The setting of the multiplexer of the MWL-AUC was adjusted so that only a single flash was recorded per integration interval. The intensity of light impinging on the spectrometer was limited to about 80% saturation at the most intensive peaks of the intensity spectrum.

To determine the optical resolution, a 200 µm slit vaporized onto a standard AUC cell window (provided by BASF AG) and it was imaged at several wavelengths. The slit window was mounted together with a normal window on a one-sector cell such that the slit was facing the inside surface of the centrepiece.

5.3. Results

5.3.1. General Aspects

Our modifications of the optics enhanced light intensity in the vacuum chamber to a great extend, as compared with the first-generation detector (Bhattacharyya 2006) (Figure 5-3).

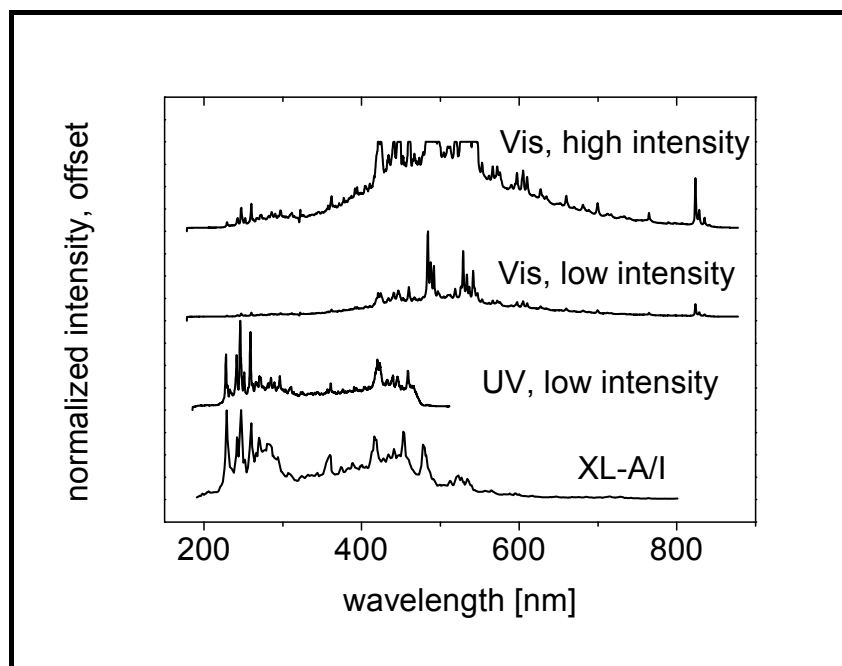


Figure 5-3: Intensity distributions of USB2000 Spectrometer

Intensity distributions for USB2000 spectrometers with different in-built diffraction gratings, as compared to the Optima XL-I. Vis, diffraction grating optimized for the visible spectral range, high/low intensity, the iris opened maximally/minimally. With the iris maximally opened, the maximum intensity of the spectrometer (4000 counts) is reached and the spectrometer is maxed out at these wavelengths. UV, diffraction grating optimized for the UV range. With the iris maximally opened, around 70% of the available channels are saturated; this data is therefore not shown. Note that the flash lamp used in the MWL-AUC is different from that of the Optima XL-I. Due to the design of the spectral dispersion/detection system in the USB2000 spectrometers, the raw intensity spectra for the different spectrometers are a convoluted function of both the emission spectrum of the flash lamp and the preinstalled diffraction grating of the spectrometer itself.

This obviously leads to a better performance of the detection systems, especially in the UV range, and allows some fine tuning of the intensity for the wavelength range that is most suitable for the experiment by adjusting the amount of light via the iris. In this respect, the spectrometer with a diffraction grating optimized for the visible region is certainly the most flexible one. However, in terms of traditional protein measurements, the UV spectrometer is more appropriate, as shown in Figure 5-3. The detected UV lamp spectra of the Optima XL-I and MWL detectors agree quite well so that a similar performance can be expected in the UV range. While the MWL UV signal decreased to zero at about 480 nm, the Optima XL-I signal only slowly decreases up to 800 nm but at a very low intensity level as compared with the UV. On the other hand, the MWL Visible signal still has sufficient intensity at wavelengths up to > 800 nm, suggesting the interesting possibility of measuring in the near-IR (>800 nm) with the existing flash lamp and spectrometer. A combination of a UV-optimized

spectrometer with one optimized for the Visible wavelength to near IR range is therefore better for the detected intensities as compared with the broadband detection of the Optima XL-I. However, it must be stated that, at maximum, 4000 counts are possible with the currently applied 12-bit USB2000 spectrometer (Ocean Optics). Application of the current modern USB4000 16-bit spectrometers (Ocean Optics) enable up to 16,000 counts, which can enable a higher flexibility and dynamic range using this spectrometer.

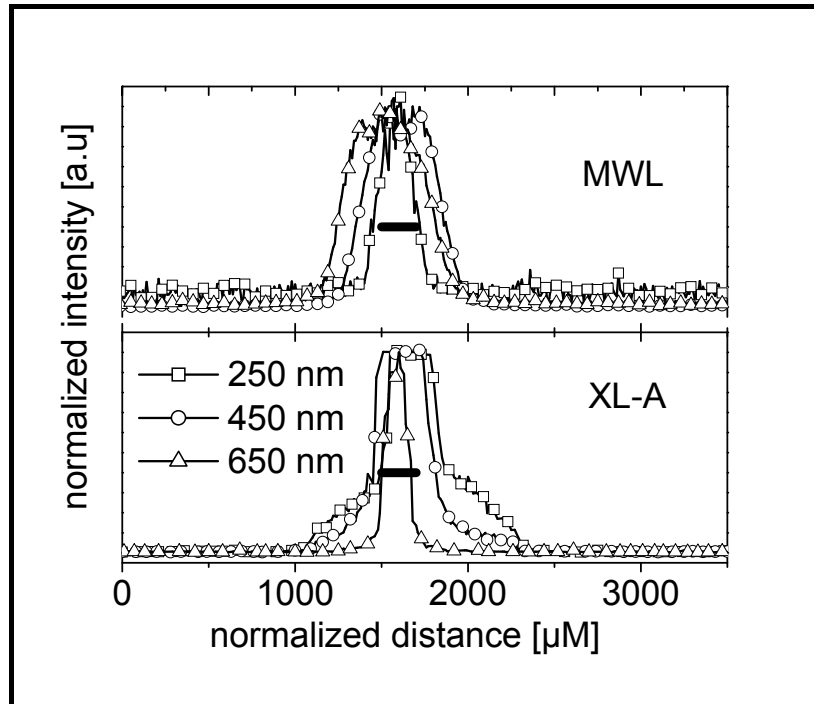


Figure 5-4 : Optical Tests of MWL-AUC and Optima XL-I with Slit

A slit of 200 μm was imaged using the MWL-AUC and the Optima XL-I at different wavelengths. The thick solid bar represents a distance of 200 μm . The wavelength resolution is dependent on wavelength. It is higher in the UV-wavelength range for the MWL-AUC, but higher in the Visible range for the XL-I.

The data density for the Optima XL-I is in the order of 0.5–0.6 points/nm, as expected from the limited precision of the gear train driving the diffraction grating, which has 4 nm accuracy.

With the USB2000 spectrometers from Ocean Optics, the total number of data points available is 2048 (3648 with the follow-up model USB 4000), therefore, as a function of the spectral range of the spectrometer, the data density is in the order of 6 points/nm and 3 points/nm for the UV- and Vis-optimized spectrometers, respectively. Although this does not reflect the actual wavelength resolution, which is limited, amongst other factors, by the band pass of the diffraction grating and its groove density, it offers plenty of data points for

averaging, thus reducing the noise of the data without affecting the accuracy of the wavelength positions.

5.3.2. Radial Resolution

In the current design of the MWL-AUC, a certain degree of wavelength dependence of the radial resolution is expected, because lens optics is used with the associated chromatic aberration problems. Such wavelength dependence of the radial resolution was indeed observed in our measurements of a 200 μm slit (Figure 5-4). The apparent radial resolution decreases with increasing wavelength, quite in contrast to the situation with the Optima XL-I, which is probably a result of optical alignments. It can also be seen from Figure 5-4 that the MWL-AUC is already capable of delivering a higher radial resolution than the Optima XL-I, especially in the UV-wavelength range most suitable for biological polymers. Note that the step motor used in the MWL-AUC (Zaber T-LA-28-SV) is capable of delivering a radial resolution of better than 1 μm . The accuracy of the radial positioning is $\pm 0.1 \mu\text{m}$, according to Zaber Technologies Inc.

A possible means to eliminate the unwanted wavelength dependence of the radial resolution would be to remove lenses altogether from the optical path. The use of a mirror-based optical system could be a useful possibility to achieve this to maintain a beam of parallel light illuminating the sample, as has already been discussed (Bhattacharyya et al. 2006), but the required mirrors with small focal lengths have to be custom made (unpublished results).

We note that the radial step size of the Optima XL-I, though set to 10 μm , corresponded on average to around 19 μm in these measurements, whereas it was 10 μm for the MWL-AUC, as set in the software. Whether this is a characteristic of the individual Optima XL-I used in these measurements or a more generalized phenomenon remains to be determined, but the 9 μm inaccuracy of the Optima XL-I is well within the radial accuracy specifications of 50 μm given by Beckman Coulter. At any rate, the radial precision of the MWL-AUC's step motor greatly exceeds that of the Optima XL-I servo motor. As shown in Figure 5-5, the radial spacing of the measurement points is very regular, especially when compared with the radial spacing of data points from the Optima XL-I. Moreover, the radial position of the data points obtained for the MWL-AUC is very reproducible without detectable radial variation, from

repeated measurements. This is a clear advantage for methods which apply pair wise subtraction of consecutive scans in order to obtain a time derivative of the concentration profiles. However, the radial accuracy was not independently determined other than from the standard radial calibration using a normal counterbalance cell. The time required to scan the whole radial length of a cell (5.8 cm–7.2 cm) is comparable for both systems. The MWL-AUC currently takes 1:17/2:00/6.51 min at 50/30/10 μm distance between consecutive data points, whereas the Optima XL-I takes 1:13/1:44/5:01 min at 50/30/10 μm .

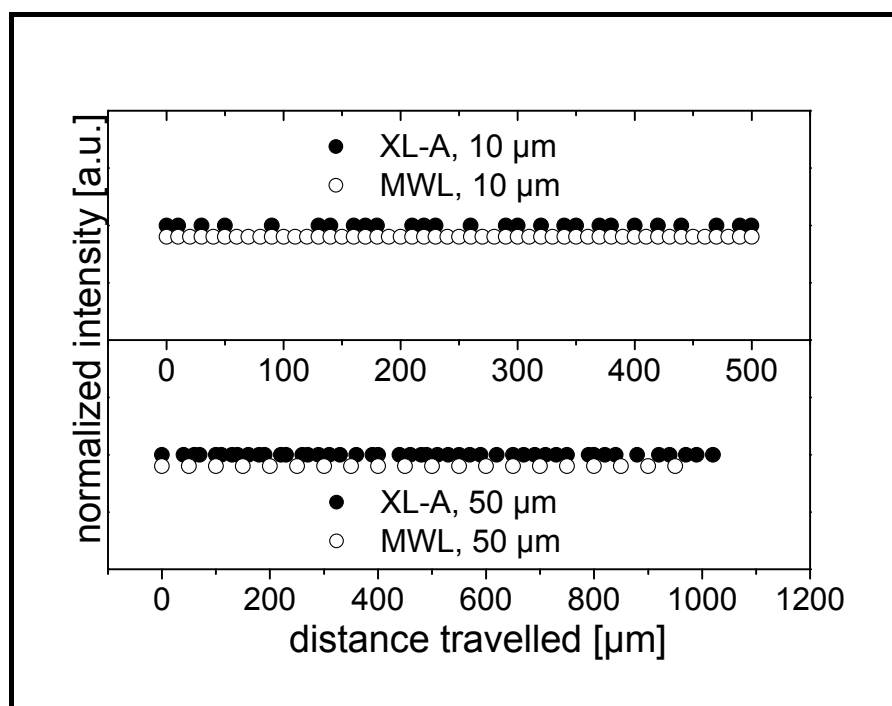


Figure 5-5 : Step motor tests of MWL-AUC and Optima XL-I

Reproducibility of the step size for the MWL and the Optima XL-I AUCs for 10 μm and 50 μm step size respectively for a scan of a cell. Not all data points of the MWL detector (50 μm) are shown for reasons of clarity.

5.3.3. Wavelength Accuracy

In contrast to the Optima XL-I, where the wavelength positions have to be calibrated internally from the intensity spectrum of the flash lamp, the USB2000 spectrometer is precalibrated by the manufacturer. The calibration constants are a characteristic of each spectrometer. As can be seen from Figure 5-6, the wavelength accuracy of the Optima XL-I and the two USB2000 spectrometers used in our MWL-AUC are comparable. Whereas the

specification of the wavelength accuracy according to the manufacturer (Beckman) is only 4 nm, the CCD array spectrometers can be tuned to a very high accuracy by choosing the correct groove density or line spacing of the grating at the expense of the wavelength range (OceanOptics 2008).

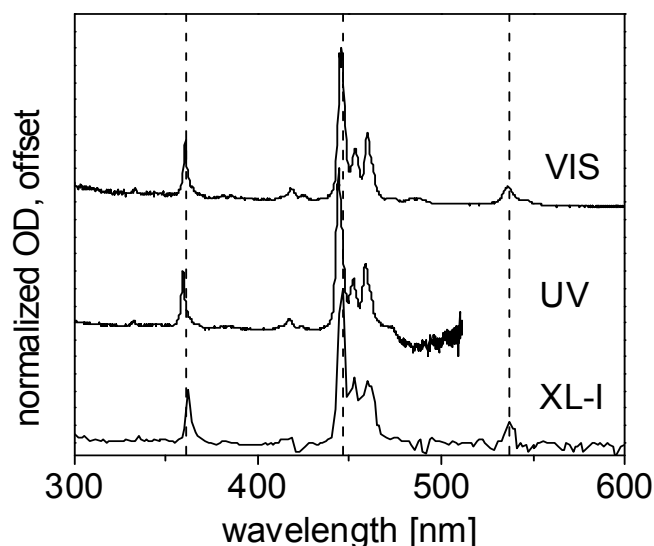


Figure 5-6 : Wavelength accuracy of the Optima XL-I and the MWL-AUC.

An Ho_2O_3 centrepiece was used to record absorbance spectra as shown. The dotted vertical lines indicate the positions for three characteristic peaks at 361, 446, and 537 nm, respectively

In the spectrometers applied in this study, a groove density of 600 was chosen together with a 25 μm slit and a wavelength range of 650–670 nm yielding a wavelength resolution of about 1.3 nm for the applied optical spectrometers (OceanOptics 2008). However, application of higher groove densities will yield a higher wavelength resolution at the expense of the wavelength range with the same 25 μm slit, like 0.3 nm for a 2400 mm^{-1} grating with a spectral range of only 140 nm (OceanOptics 2008). Nevertheless, the most reasonable compromise appears to be a wavelength range of around 600 nm combined with a wavelength resolution of 1.2–1.3 nm, which is more accurate and much more reproducible than the wavelengths from the Optima XL-I. Therefore, the capability of around 3 pixels/nm can already be used for effective data averaging without losing spectral resolution.

The USB2000 spectrometers with which the data in Figure 5-6 were recorded have been in use in our laboratory for more than two years. In principle, wavelength positions can be

expected to be stable over the life-time of the spectrometers due to the precalibration and fixed position of the diffraction grating for the USB2000 spectrometers. This clearly increases reproducibility and reliability of repeated, independent measurements with this type of optics.

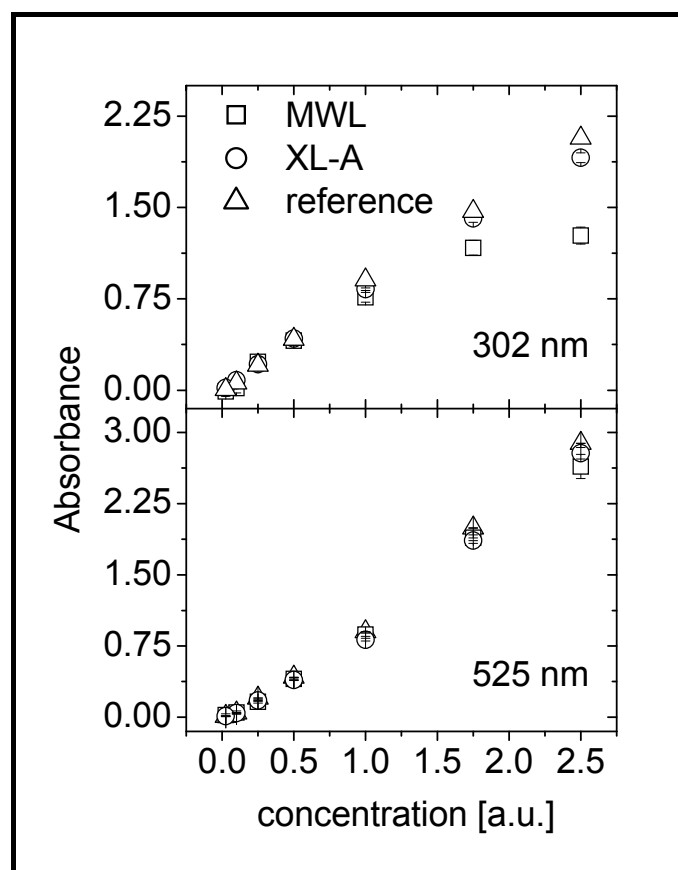


Figure 5-7: Absorbance accuracy of the MWL-AUC at different wavelengths.

The reference are data measured by a benchtop double-beam spectrometer (model lambda 2 from Perkin Elmer).

5.3.4. Absorbance Accuracy and Linearity

We measured the absorbance accuracy in two wavelength regions, in the near UV (302 nm) and in the Visible (525 nm) (Figure 5-7). This was done in order to explore that the influence different light intensities might have on the accuracy and linearity of the absorbance readings. Generally, data for the MWL-AUC and the Optima XL-I compare well with those measured from a benchtop spectrometer. Differences exist for the range of linear data. This range was found to be very much dependent on the initial light intensities, I_0 . At 302 nm, data recorded with the MWL-AUC become nonlinear at an OD of around 0.8, whereas those for the Optima XL-I are still linear well above an OD of 1. At 525 nm, data appear linear for the MWL-AUC

and the Optima XL-I up to an OD of 1.5. From the intensity spectrum for the MWL-AUC for these measurements (Figure 5-8) it is apparent that at 302 nm, I_0 at the detector was 265 counts, which is a very low value. At 525 nm, I_0 was around 3600 counts, close to the maximum number of 4000 counts. However, the light intensity can be fine-tuned to a certain degree via the iris (*section 5.2.2*) to improve I_0 and hence linearity of the data in the desired wavelength range.

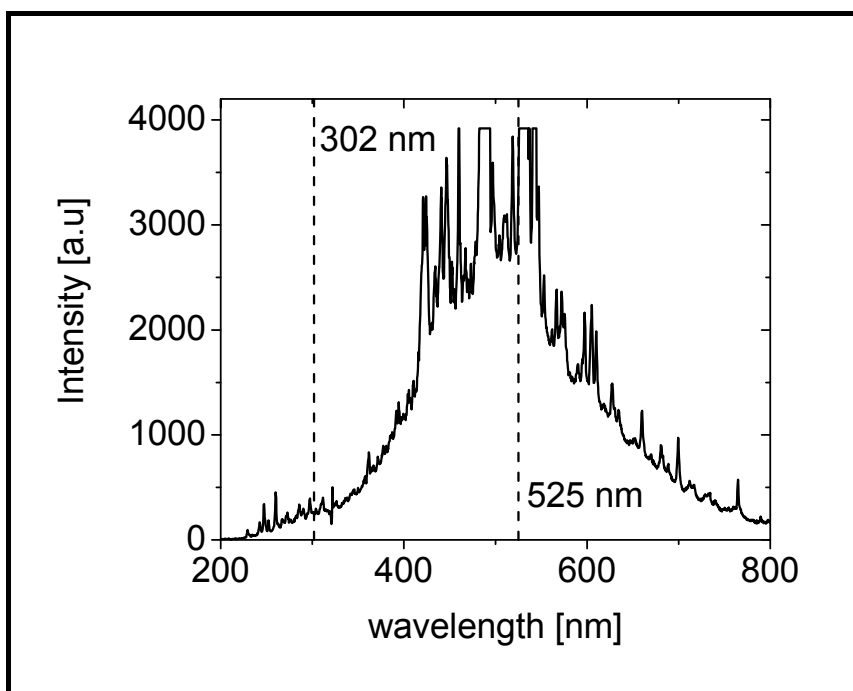


Figure 5-8 : Intensity profile of linearity tests

Reference intensities of the absorbance measurements are shown in Figure 5-6. The dotted vertical lines indicate the two wavelengths at which data were recorded.

The dark noise of the spectrometer is on the order of 5–10 counts. The standard deviation of the noise is slightly worse for the MWL-AUC than the Optima XL-I. It is in the order of ± 0.03 OD compared with ± 0.02 OD at 302 nm, whereas it was at ± 0.02 OD and ± 0.01 OD at 525 nm. The precision of the benchtop photometer was two orders of magnitude below these values at both wavelengths. The slight decrease in wavelength precision for the MWL-AUC appears to be caused by the raw intensities of the measurements, but also by other factors specific to our setup.

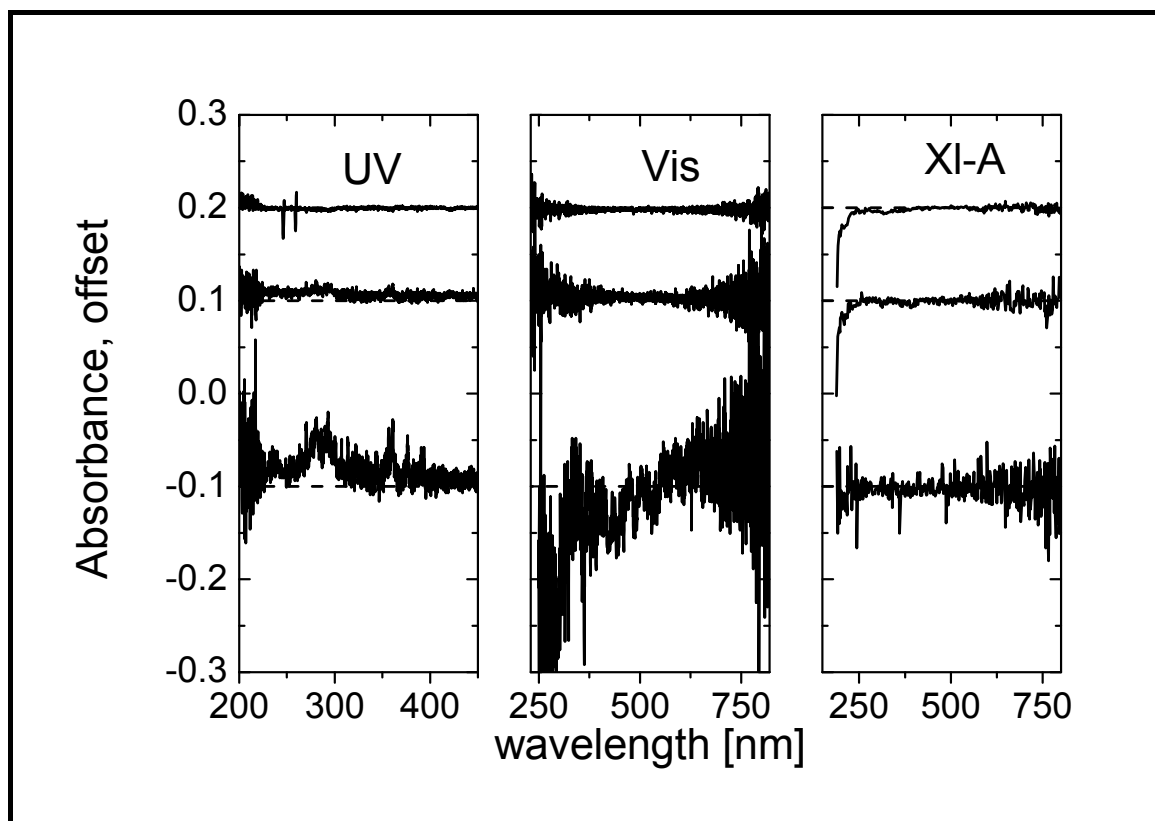


Figure 5-9: Noise comparison between the Optima XL-I and the MWL-AUC

Spectra were taken with 1/10/100 point averaging, shown as the bottom/middle/top spectrum, respectively. Dotted horizontal lines indicate the offset true baselines. Due to the higher point density for the USB2000 spectrometers, the spectra appear broader as they are in reality. Note the differences in scale of the abscissae. The respective statistical data are: UV(1): -0.016 ± 0.029 ; UV(10): 0.007 ± 0.009 ; UV(100): 0.001 ± 0.005 ; Vis(1): -0.011 ± 0.059 ; Vis(10): 0.004 ± 0.010 ; Vis(100): -0.002 ± 0.003 ; XL-I(1): -0.003 ± 0.017 ; XL-I(10): -0.001 ± 0.006 ; XL-I(100): -0.002 ± 0.004 . UV scanned 200–500 nm; Vis scanned 250–800 nm and Optima XL-I scanned 200–800 nm.

5.3.5. Intrinsic Noise of the Data

To qualitatively compare the intrinsic noise of the data at different wavelengths and the baseline accuracy, we monitored an empty hole of a rotor over the full accessible wavelength range and at a number of averages. It is possible to compare the noises of the data between XL-I and MWL-AUC if the averaging is done. But without averaging, MWL-AUC is worse than XL-I. One plausible explanation for this observation could be the absence of flash-to-flash intensity normalization for the MWL-AUC, which quickly averages out. In future designs, this normalization of the flash lamp intensity for every wavelength will be achieved by a second identical spectrometer which monitors the intensity of the lamp after a small part

of the light was diverted to this spectrometer by a beam splitter. With 10 and 100 point averaging, the noise level appears to be similar for the Optima XL-I and the MWL-AUC. Baseline stability is satisfactory in all cases, provided enough averages are being taken. The lack of baseline stability for measurements is a direct reflection of the absence of flash-to-flash normalization as well.

One of the greatest possibilities of the new MWL-AUC can also be gathered from Figure 5-9: it took only around 15 s to record a full wavelength spectrum with 100-points averaging with the USB2000 spectrometers, whereas recording the spectrum with the Optima XL-I took around 180 minutes. The reduction in experiment time without losing information is obvious. Besides the noise generated by the variation of lamp intensity, a further source of noise is that the computer for the detector control and data acquisition does not work in real time. In the present labview-based program, the lack of real time operation generates slight variations in the generation of the triggering of lamp and spectrometer, as we now use software triggering of the spectrometer which allows for faster data acquisition (down to 2 ms for the applied USB 2000) than the hardware triggering mode, which was applied in the earlier described setup (50 ms integration time)(Bhattacharyya et al. 2006). With this change, we eliminated the noise caused by the response time difference of the spectrometer and the flash lamp, which were triggered by the same pulse. As the flash of the flash lamp is very short, in the order of 3-4 μ s, slight variations of the trigger pulse timing will cause noise.

However, when using software triggering of the spectrometer with an integration that is long enough for whole rotation of the rotor even at the highest rotational speed. The timing of the spectrometer triggering with respect to the turning rotor cannot be determined anymore in contrast to hardware triggering. There is a small probability that the spectrometer starts to acquire data in the middle of a flash, which leads to a drop in the detected intensity. For further development, we are planning to solve this problem by using much faster USB 4000 spectrometers with hardware triggering as fast as 10 μ s and to calibrate the response time of the spectrometer and the flash lamp to the same trigger pulse. In addition, we will use a real-time system to ensure correct timing.

5.4. Discussion

Comparing with the results presented in an earlier contribution on a first-generation MWL detector (Bhattacharyya, 2006) progress has been made on the issue of light intensity available at the detector. With the current modifications, it is possible to bring more light into the vacuum chamber than the dynamic range of the CCD-chip can digest. This is a mandatory requirement for precise, linear, accurate – and hence useful – measurements with the MWL-AUC, and is clearly apparent from our data. Due to the very broad distributions of intensities over the available wavelength range and the clear correlation with linearity of the recorded data, we have added to the software of the MWL-AUC the feature that the spectrum of I_0 is being stored together with the corresponding measurements. This will allow for the definition of linearity ranges after the experiment has been performed. The higher dynamic range of the USB4000 spectrometers will be of great benefit in this respect, too.

Chapter 6 :Biological Application of MWL-AUC: Protein Mixture

6.1. Introduction

In this chapter, we compare the performances of the commercially available Beckman Coulter Optima XL-I and the MWL-AUC in characterizing a mixture of IgG, aldolase and BSA, three non-interacting proteins, and discuss further improvements to the existing machine. For the materials and the methods of the protein chapter, it was referred to Appendix.

6.2. Results and Discussion

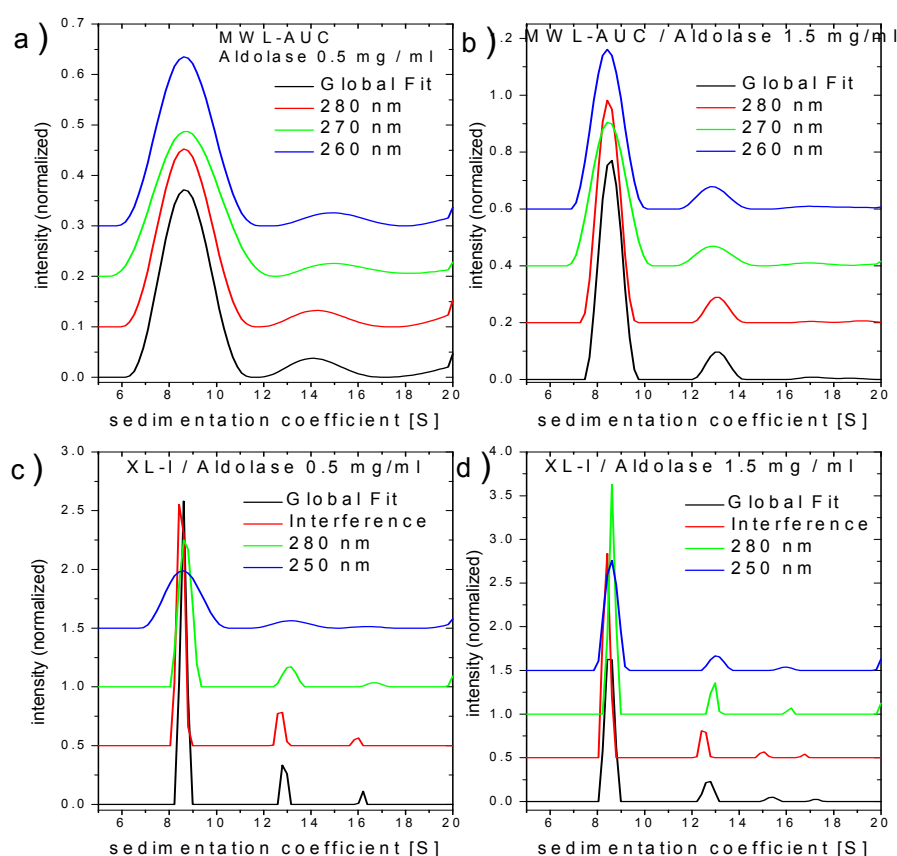


Figure 6-1: Comparison of Optima XL-I and MWL-AUC in c(s) and global fit of aldolase

Sedfit analyses of aldolase at different concentrations are shown in Figure 6-1. Figure 6-1(a) shows sedfit analysis of single wavelength of 280 nm, 270 nm and 260 nm that is taken from MWL data. So, in this chapter, we are not using all the wavelength information of MWL

data. In order to determine whether MWL data quality at a specific wavelength is better or worse than Optima XL-I, we are only selecting three specific wavelengths from the set of different wavelengths from MWL data. In Figure 6-1(a), c(s) analysis of aldolase with concentration 0.5 mg/ml is shown. The selected wavelengths are 260, 270 and 280 nm. These are selected point wavelengths from set of 500 wavelengths, ranging from 200nm to 550 nm. Also, global fit of the data including 260, 270 and 280 nm are shown in the graph. In Figure 6-1(c), c(s) and global fit of XL-I data are shown. Interference and absorbance of 250 nm and 280 nm are shown. If we compare absorbance data of Figure 6-1(a) and Figure 6-1(c), we can infer that both detectors produce similar peaks with the same peak positions. However, MWL data peaks look wider. In this kind of analysis, Balbo *et al.* concluded that wideness of the peaks can be attributed to regularization and noise in the data (Balbo et al. 2005). Consequently, wider peaks can be attributed to high noise ratio and low intensity of MWL-AUC in the UV region (this can also be seen in Figure 5-7 and Figure 5-8), which will be discussed later. Despite high noise ratio, these plots show that MWL-AUC in the UV region can be successfully used for single proteins. If we compare the global fit of Figure 6-1(a) and Figure 6-1(c), then the global fit of the Optima XL-I data can be attributed to interference optics that does not present in MWL-AUC.

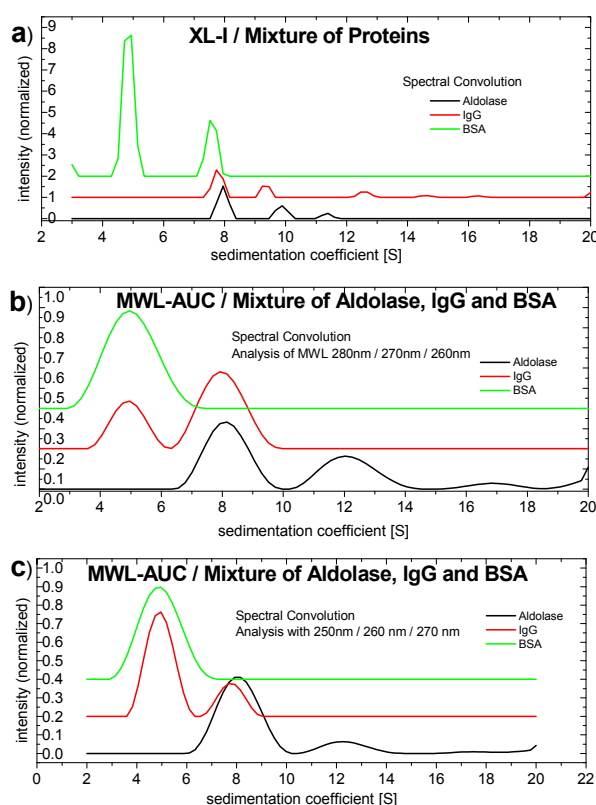


Figure 6-2: Three wavelengths, global multisignal analysis of MWL-AUC and Optima XL-I

In Figure 6-1(b), c(s) analysis and global fit of 1.5 mg/ml aldolase experiment with wavelengths of 260, 270 and 280 nm are shown. The peak positions of Figure 6-1(a) and Figure 6-1(c) are identical, but in Figure 6-1(b) the peaks are narrower. This is due to the high signal-to-noise ratio of highly concentrated aldolase in comparison with less concentrated aldolase. Noise makes the peaks wider (Balbo et al. 2005). In Figure 6-1(d), c(s) and global fit of 1.5 mg/ml aldolase with 250 nm, 280 nm, and interference optics of the Optima XL-I is presented. Similarly, in Figure 6-1(d) c(s) peaks of absorbance are at the same position as in Figure 6-1(b), but they are narrower. Consequently, the noise level of MWL-AUC is still higher than for the Optima XL-I. The thinner global fit of Figure 6-1(d) can also be attributed to interference analysis that does not exist in MWL-AUC.

As a next step, analysis of three protein mixtures of aldolase, IgG and BSA is presented in Figure 6-2. This analysis was performed by the global multisignal analysis module of Sedphat. Three different wavelength scans (250, 260 and 280 nm) were uploaded by the multisignal analysis module. This module tries to form spectra decomposition of different protein distributions from these signals. Figure 6-2(a) shows the result of this analysis with Optima XL-I data of absorbance at 250, 280 nm and interference. These results show successful decomposition of S distribution of the three different proteins. Peak position of the proteins agrees with previous study (Balbo et al. 2005). If we look at the result of analysis of MWL-AUC data with 250, 260 and 280 nm in Figure 6-2(b), we cannot achieve the same success. The S distribution of IgG shows a ghost peak at about 5 S. This is exactly the same position as the main peak of aldolase. Consequently, this peak shows that the system could not make spectral decomposition of three different proteins with three selected wavelengths of MWL-AUC. These ghost peaks are referred to noise in data in the previous study (Balbo et al. 2005). In Figure 6-2(c), the results of multisignal analysis of 250, 260 and 270 nm wavelengths are shown. This analysis is performed in order to see the wavelength dependence of the analysis result. However, changing the wavelength from 280 to 270 nm does not solve the problem. The resulting graph still has a ghost peak of IgG, which is bigger in this case.

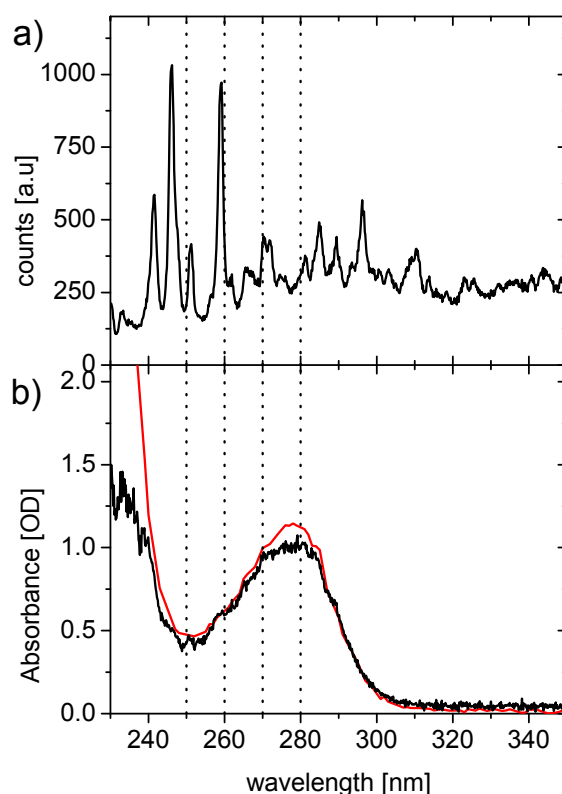


Figure 6-3: Reference intensity of MWL-AUC and wavelength scan of Optima XL-I and MWL-AUC
(a) Reference intensity of Xenon light taken from the reference sector of sample cell filled protein mixture; (b) Black Curve:UV/Vis spectra of the mixture sample with MWL-AUC; Red Curve: Wavelength Scans of mixture that is taken by XL-I with 5 replicates.

In order to observe the noise and the linearity problem of the MWL-AUC, we have prepared Figure 6-3. The reference intensity of MWL-AUC in this UV range is shown in Figure 6-3(a). UV sensitive USB2000 was used to conduct these experiments (see sub-section 3.3.5). Figure 6-3(a) shows the low intensity in this range. Low intensity reference light in UV region makes MWL-AUC data noisier than Optima XL-I data. The wavelength scan of the Optima XL-I in Figure 6-3 was taken with five replicates but MWL-DATA was taken as single reading. For a better noise comparison, we refer to the section of intrinsic noise of the data (sub-section 5.3.5). On the other hand, Figure 6-3(b) shows the linearity problem of MWL-AUC data. Between 270 nm and 290 nm in Figure 6-3(b), the MWL-AUC spectrum spectra differs from the Optima XL-I spectra, which indicates that linearity is lost in this range. This is clearly due to the low UV intensity of the system (see Figure 5-7 and Figure 5-8). Linearity in relation to intensity has been discussed in the section on absorbance accuracy and linearity (sub-section 5.3.4). Despite these disadvantages of the UV region of the MWL-AUC data, we obtained the correct S distribution for the single protein mixture.

This shows that MWL-AUC data is still useable to analyze any protein system without spectral decomposition. The results shown in Figure 6-2 depict that the UV region of MWL-AUC data cannot be used for the spectral decomposition algorithm of the Sedphat program, in which the result is highly affected by noise (Balbo et al. 2005).

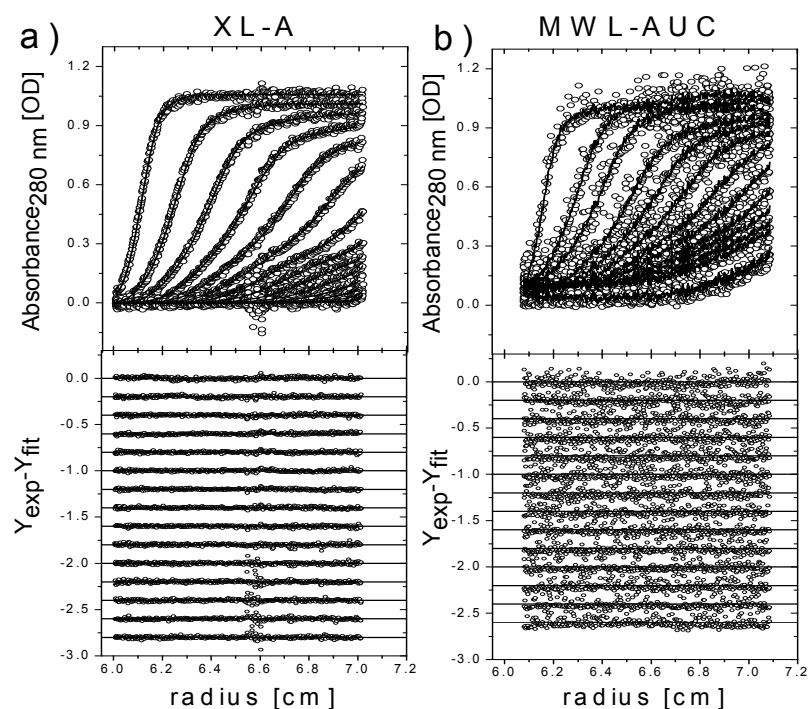


Figure 6-4: MWL-AUC and XL-I analysis residuals of 280 nm analysis

In Figure 6-4, residuals and c(s) fit of MWL-AUC data and Optima XL-I data of absorbance at 280 nm of mixture solutions are shown. The fit is compared. Optima XL-I data is less noisy in comparison with MWL-AUC data, which agrees with our previous discussion. Residuals are better in the Optima XL-I. This fact clearly shows the noise difference.

This design of detector is the first running prototype of a MWL-AUC which produces reasonable data. The main weak point of the system is low intensity in the UV region. The low intensity makes the system noisier and causes linearity problems. This type of noise can be identified as low intensity noise. Low intensity noise is the highest source of noise if there is low intensity. When there is high reference intensity, e.g., in the region of visible light, low intensity noise is not a part of the noise anymore. In high reference intensities, the greatest source of noise is wavelength independent noise, which is explained below. Although low intensity noise was present, the system measured aldolase protein successfully, can be seen in

Figure 6-1. As explained before, the amplitude of low intensity noise only prevents the usage of the spectral decomposition algorithm, but it does not prevent the usage of other analyses without any spectral decomposition.

Secondly, another type of noise in this system comes from the variation in intensity of the Xenon lamp. In MWL-AUC there is no intensity normalization. There are two well-known noise types in the AUC field; radial independent and time independent noise (section 5.3.5). The noise in our system is different from these classical types of noise. This new type of noise can be called “wavelength independent noise”. Due to our observations, wavelength independent noise is the second greatest source of noise in the low intensity conditions. In the presence of high intensity, wavelength independence becomes the main source of the noise. As explained above, wavelength independent noise is due to Xenon light fluctuations. In the Optima XL-I, this problem was solved by using a reflector in the absorbance optic system (Figure 2-6). This reflects a specific percentage of the incident light to an incident light detector, which is a simple diode detector. This diode detector normalizes the fluctuations in the Xenon flash lamp. This is easy to do in the Optima XL-I, because there is only one wavelength in each scan. However, this task is multi-dimensional and complex in MWL-AUC, since hundreds of wavelengths are recorded at once. The reflector and all optics will work differently at each different wavelength. Furthermore, the system cannot work with a diode incident light detector, as the incident diode detector can only detect one wavelength. A proper incident light detector for MWL-AUC can only be another USB2000 CCD spectrometer. However, there is not enough mechanical space inside the AUC vacuum chamber to insert another CCD spectrometer. Although the user manual of the light source we use (Hamamatsu L9546 Xenon flash lamp module) shows 5% intensity variation from flash to flash (Hamamatsu 2006), we have observed a higher ratio than is claimed. Despite the existence of wavelength independent noise, this noise is not the dominant source of noise in the presence of low intensity noise.

Finally, in this chapter, we only used three different wavelengths among 300 wavelengths (250–550nm). Comparison of only three wavelengths of MWL-AUC and the Optima XL-I, shows that data from the latter has less noise, due to the fact that MWL-AUC has low intensity in UV region. We conducted this test in order to repeat what was done by Balbo et al. (Balbo et al. 2005). This analysis does not use overall information content of MWL-AUC, due to the fact that the analysis uses just three different wavelengths among 300 wavelengths.

The reason for using only three wavelengths instead of 300 is due to the fact that Sedphat can only accept three wavelengths to apply spectral decomposition. Furthermore, Sedphat can only obtain information from a small portion of the MWL-AUC data content. This is why we are waiting for further development of analysis software that can appropriately take all the information content from MWL data, as Ultrascan can does very successfully with the CdTe nanoparticle system (see chapter 8).

Chapter 7 : Industrial Application of MWL-AUC: Investigation of β -Carotene-gelatin composite particles

7.1. Introduction

Combined with the fractionating power of the AUC, application of the MWL detector with its additional structural and/or compositional information on light-absorbing samples can yield distributions of the individual components in complex mixtures with respect to composition and size/density related to different chromospheres. This can start with relatively straightforward issues like sample homogeneity and purity but can then become increasingly complex in the case of composite and/or interacting samples. Especially for such complex samples, MWL-AUC has a huge potential, as spectral discrimination can synergistically enhance the hydrodynamic resolution (Balbo et al. 2005). In this chapter, we will show the capabilities of MWL-AUC for the analysis of an industrial composite sample of β -carotene and gelatin. This system was investigated previously with X-ray scattering, UV/Vis absorption spectroscopy, FOQELS (Fiber-optic quasi-classical light scattering), and micro electrophoresis and, on basis of these results, a core-shell structure was presented (Auweter et al. 1999), as shown in Figure 7-2. The core structure, with a diameter of 120 nm, consists of partially crystallized, partially amorphous β -carotene as the active ingredient. The shell structure consists of gelatin, functioning as a bio-degradable protection colloid. This hybrid structure self-assembles in a carefully tuned co-precipitation of gelatin (from an aqueous solution) and the active ingredient (from a lipophilic solvent). Such particulate formulations can transport an active ingredient that is not water soluble across an aqueous phase with high bioavailability, in this case provitamin A. These particles are not persistent, but disassemble and are digested quickly in biological media.

Two forms of hydrosol are explained by Auweter and colleagues (Auweter et al. 1999). β -carotenes can precipitate as H aggregate or J aggregate; these two morphologies do not interconvert and are regarded as being kinetically stable over years. The H aggregate is observed in precipitation from dilute solutions (0.3 weight %), whereas the J aggregate is observed at higher concentrations (1.0 weight %). Auweter calculated a 40 nm hypsochromic shift observed for an H aggregate and a bathochromic shift in J aggregates (Auweter et al.

1999). This results in a significant color change of the product from yellow to red depending on the precipitation conditions and hybrid particle size (Figure 7-1 and Figure 7-2). This color change is the basis for the industrial application of the β -carotenes as pigments for food applications.

What is of interest for industrial applications is not only the purity of the sample concerning the color characteristics (brilliance of color due to steep absorbance profiles) or the homogeneity of the sample (different species or unbound gelatin), but furthermore any possible transitions between different structures. This is a problem which can be advantageously solved in a single MWL-AUC experiment, which we will describe in this work.

7.2. Material and Methods

The β -carotene product was obtained in powder form as a laboratory sample from BASF AG, (Ludwigshafen, Germany). An aqueous dispersion in water was prepared with a concentration of 0.05 g/l. The UV/Vis spectrum of the dispersion and of the free gelatin is shown in Figure 7-1. Further details of AUC method and materials are explained in Appendix.

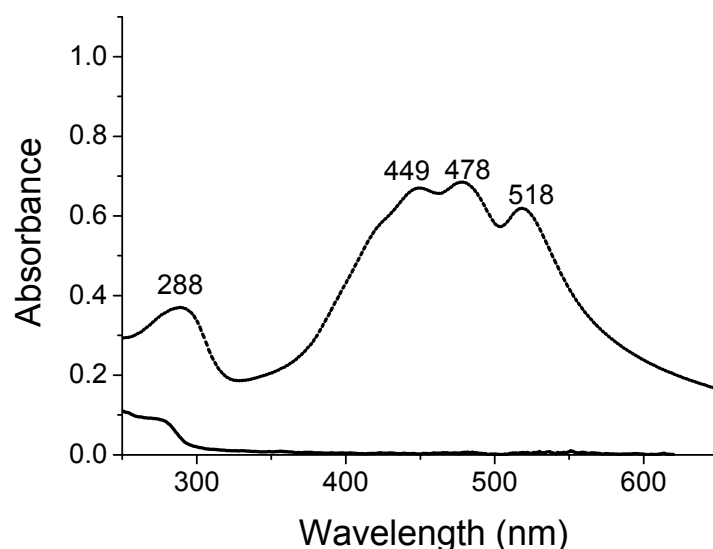


Figure 7-1: UV/Vis spectra of shell β -carotene/gelatin sample

Dashed line; UV/Vis spectrum of the core-shell β -carotene/gelatin sample with 0.05 g/l concentration; Solid line: UV/Vis spectrum of gelatin at 1 g/l.

7.3. Results and Discussion

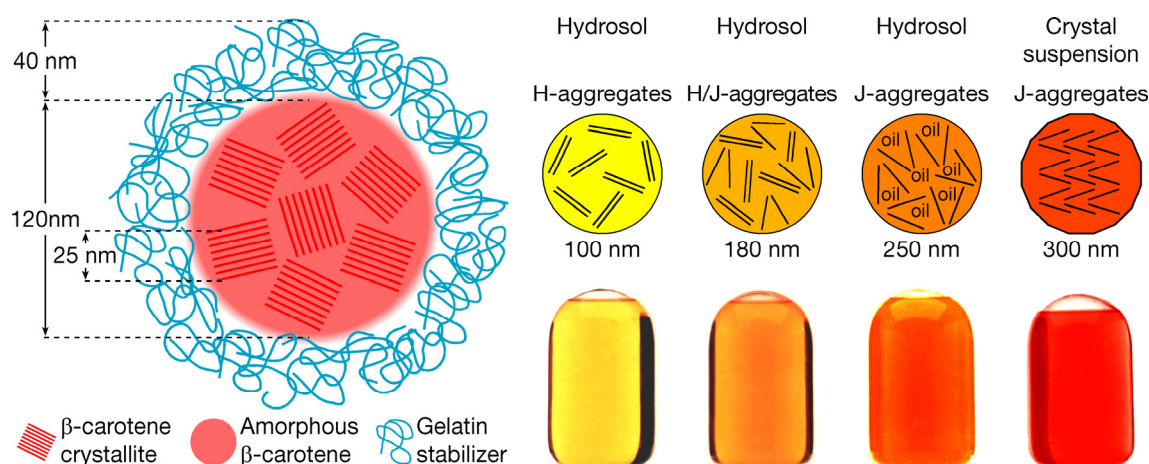


Figure 7-2 : Structure of β -carotene microparticle system

Left: Assumed structure of the β -carotene microparticle system (Auweter et al. 1999). Right: Color change of β -carotene/gelatin microparticles due to particle size and structure.

In principle, the entire dataset can be evaluated globally, and efforts are underway to incorporate such routines into the Ultrascan evaluation software package (Demeler, 2005). However, even then we are confronted with a confounded polydispersity of both optical and colloidal/hydrodynamic properties. On the left side of Figure 7-2, the assumed core-shell structure of a β -carotene microparticle is shown (Auweter et al. 1999). Such a complex hybrid particle exhibits several levels of polydispersity, which impact the distribution of sedimentation coefficients observed in an AUC:

- (1) Diameter of the inner core;
- (2) Chemical composition, especially oil content, of the inner core;
- (3) Concentration of the adsorbed protection colloid (gelatin);
- (4) Degree of swelling of the gelatin.

Parameters (1) and (2) determine the optical properties and bioavailability that are decisive for the commercial application profile. For the smallest particle sizes, β -carotene is an H aggregate, while for the biggest particle sizes, β -carotene forms J aggregates. Intermediate particle sizes are assumed to integrate H and J aggregates in differing ratios (Auweter et al. 1999). Parameters (3) and (4) determine the thickness of the protection colloid layer, which is typically 40 nm in pure water. The buoyant density of gelatin is rather high (above 1.3 g/cm³), and cannot be matched with a non-interfering solvent such as heavy water.

All parameters from (1) to (4) enter into the calculation of the effective density and the hydrodynamic diameter of the hybrid particle. The frictional force under sedimentation depends on the ion concentration and pH because the gelatin may collapse or swell, thus changing the effective frictional forces (and thus changing the observable sedimentation constant) although the chemical composition and buoyant density, which in principle could be measured in a Krattky gauge or density gradient, stay the same. The swelling of the gelatin corona alone impedes an exact conversion from measured sedimentation constants to hydrodynamic diameters. Considering that parameters (1) and (2) also contribute to the polydispersity in the observable distribution of sedimentation coefficients, we decided to limit ourselves to a conservative evaluation on the level of sedimentation fractions, not sizes.

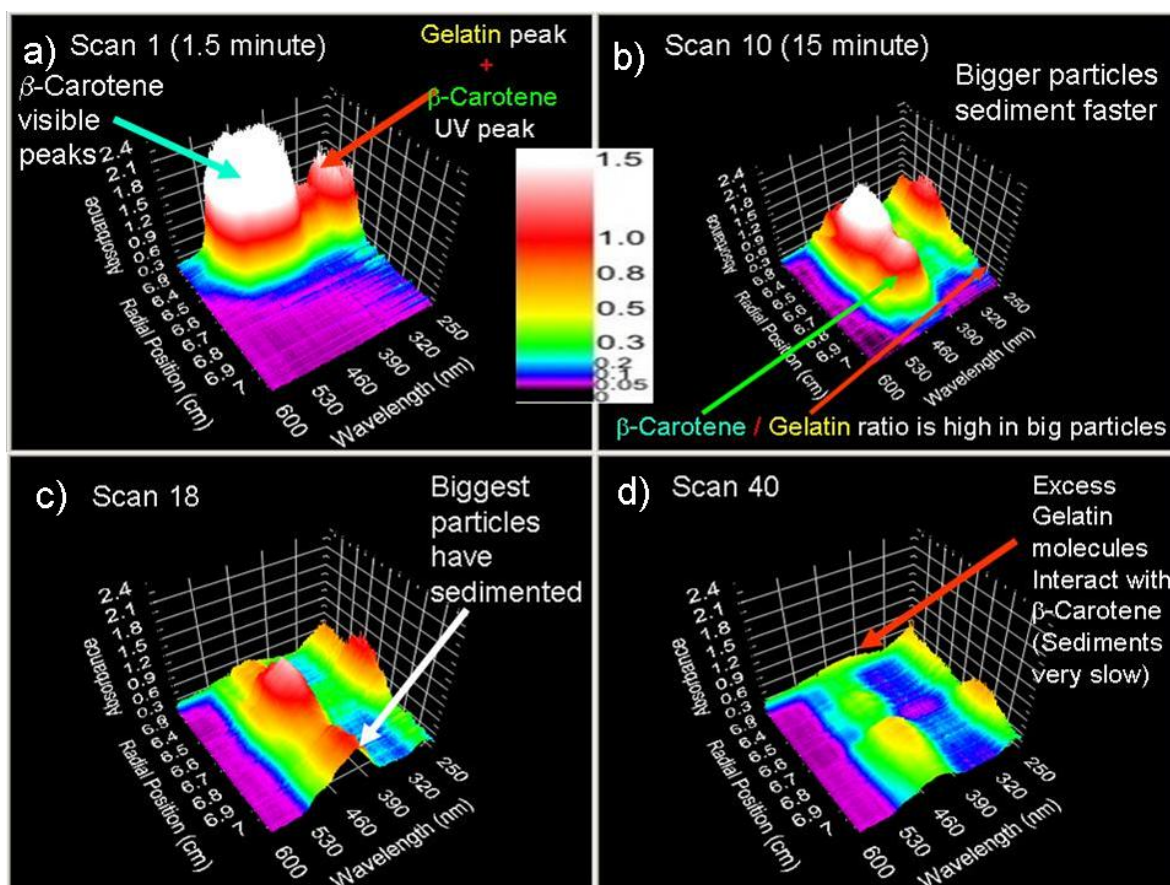


Figure 7-3: 3D sedimentation of β -carotene microsystem

Three-dimensional plots of the raw data from a band sedimentation experiment with β -carotene detected with the MWL detector. The axes are wavelength, absorbance and radial position. (a) Scan 1 (1.5 minutes); (b) Scan 10 (15 minutes); (c) Scan 18 (27 minutes); (d) Scan 40 (60 minutes).

We now discuss the optical properties that result from the specific colloidal microstructures as discussed above. Due to different preparation conditions, the morphology of the β -carotene

core changes. H and J aggregates have different UV/Vis spectra, shown as visual impression on the right of Figure 7-2. In Figure 7-1, the dotted line curve shows the UV/Vis spectrum of 0.05 g/l product without any ultracentrifugation. Four peaks, at 288nm, 449nm, 478nm and 518 nm, can be seen. The three peaks in the visible can be attributed to the $1A_g^- (S_0) - 1B_u^+$ (S_2) transition with the vibrational progression 2-0, 1-0, 0-0 of the C-C stretch vibration along the alternately double-bonded electronically conjugated backbone of the carotenoid (Polivka and Sundstrom 2004). The UV peak can also be attributed partially to the carotenoid transition $1A_g^- - 1A_g^+$, which is forbidden by symmetry, but becomes allowed in the crystalline assembly. The spectrum of the composite particle indicates the β -carotene J aggregate (Auweter et al. 1999). In Figure 7-1 the solid curve shows the pure gelatin spectrum for 1 g/l. It can be seen that gelatin only contributes to the UV region of the spectra below 280 nm. However, the contribution of gelatin is vanishing compared with the three times stronger absorption of the composite sample at 20 times lower overall concentration. Another component that presumably contributes to the UV absorption is the dispersing agent (a low-molar-mass organic acid) that is added during the co-precipitation.

Figure 7-3 shows four of the 40 experimental scans. If we put all these 40 scans in sequence, we can create a 3D movie of the sedimentation. Figure 7-3(a) shows scan 1, where particles have just been transferred from the reservoir to the sample column. The baseline offset is 0.05 (purple) due to the absorption calculation with an empty cell as reference. We see two main peaks. The peak in the visible region is assigned to β -carotene. In the UV range, there is an overlay of two peaks, one is the UV peak of β -carotene (see Figure 7-2) and the other is the UV signal of gelatin. After 15 min of sedimentation, fractionation of the sample was obvious and the first sedimentation fraction proceeds to the bottom of the cell. Scan 10 (15 min) is the last scan where the entire particle range can be seen before the first particles reached the bottom. If we compare the height of the peak in the UV and visible region at different radial positions, the ratio changes. For the faster sedimenting particles, the ratio of β -carotene to gelatin is higher. This is the first important result, demonstrating that the sample is not homogenous. Instead, the particles change their colloidal properties in correlation with the optical properties. The observed effect can be explained by a higher content of stabilizing agent that induces smaller particle sizes. Note that the shape of the peak at 288 nm (Figure 7-1) does not exactly match the gelatin absorption and that the expected contribution of gelatin is weak at the applied concentrations, hinting at a combined action of

both gelatin and the dispersing agent added during the co-precipitation in particle synthesis. The third part of Figure 7-3 shows the scan after 27 min. Here, the fastest particles have sedimented already. In the fourth part of Figure 7-3, we saw the last fraction that remained after 60 min of sedimentation, which is mainly composed of gelatin. However, some β -carotene absorption is still visible, which seems to be solubilized in small amounts by the excess gelatin or excess dispersing agent. We didn't detect free gelatin in the analysis. In an independent experiment we measured the characteristic sedimentation behavior of gelatin with the interference optics of the Beckman Optima XL-I AUC at 44,000 rpm. We found a sedimentation constant distribution from 2 to 10 Sved. This confirms our assignment that the last fraction cannot be pure gelatin.

To summarize the global evaluation, Figure 7-3 demonstrates the power of MWL-AUC. We can differentiate particles, observe the full UV/Vis spectra of the particles and draw conclusions about the different components in the complex sample mixture already without any further evaluation, as the Y-axis shows the full UV/Vis wavelength range. This is a key feature of MWL-AUC. Such analysis was impossible in analytical ultracentrifugation experiments before.

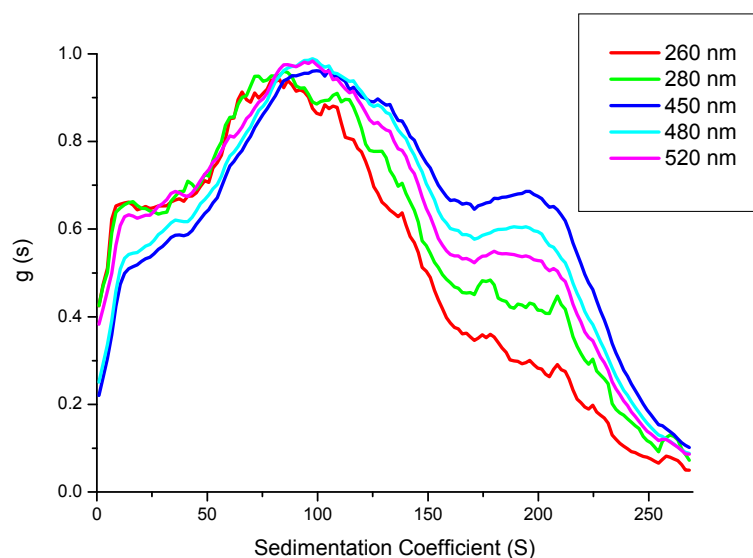


Figure 7-4: Sedimentation coefficient distributions at different wavelengths

We can also use projections of the data onto individual axes and proceed thus to a more quantitative evaluation. In order to calculate the full s-distribution of all particles, we have selected scan 10 for further evaluation, as this scan shows fractionation of the mixture while

no particles are yet lost due to complete sedimentation. More information is potentially available with a global evaluation of the entire dataset. In Figure 7-4, the s-distribution of the particles is shown for five different representative wavelengths out of 330 (250 nm to 750 nm with a wavelength resolution of 1.5 nm). We have selected the wavelengths according to the peaks of the β -carotene microparticles: 260, 280, 450, 480 and 520 nm in Figure 7-1.

The s-distribution is obviously very broad. Due to the chemical heterogeneity of the particles and the resulting density distribution, it is not possible to convert the sedimentation coefficient to the particle size. However, all important sample characteristics can be discussed for the s-distributions. From Figure 7-4 we conclude that there are at least three fractions in the sample; small hybrid particles with $s < 25$ S, a main fraction around 100 S, and larger particles around 200 S. Their absorption spectra (and chemical composition) are clearly different, as can be seen in Figure 7-5.

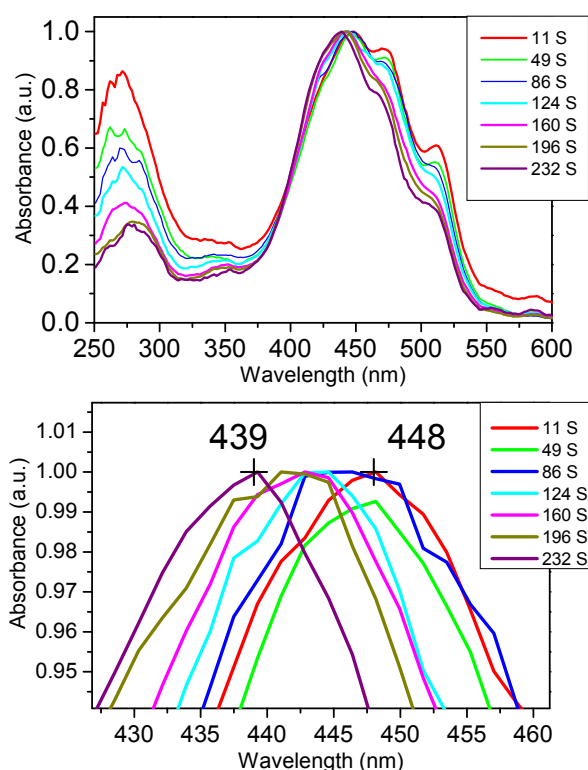


Figure 7-5: UV/Vis spectra of sedimenting β -carotene microsystem

Top: Normalized UV/Vis spectra of particles with different sedimentation coefficients, Bottom: Zoom the range around 450 nm and peak positions of 10.6 S (448 nm) up to 232 S (439 nm).

In Figure 7-5, seven representative UV/Vis spectra are shown. The spectra agree well with that of pure H aggregate (Auweter et al. 1999). However, the original sample contained J aggregates too (Figure 7-1, dashed line). We believe that the J aggregates were already precipitated before the first scan was taken in the AUC cell. Indeed precipitation of particulate material inside the reservoir of the Vinograd cell was observed visually after cell disassembly following the experiment. However, irrespective of the actual nature of the particulate material that remained in the Vinograd cell reservoir, the result speaks for itself that the coloristic polydispersity (Figure 7-1) is not due to an intra-particle but an inter-particle distribution of morphologies (Figure 7-6). This result is contrary to the previous assumption that is sketched in Figure 7-2, where H and J aggregates would coexist in the particles.

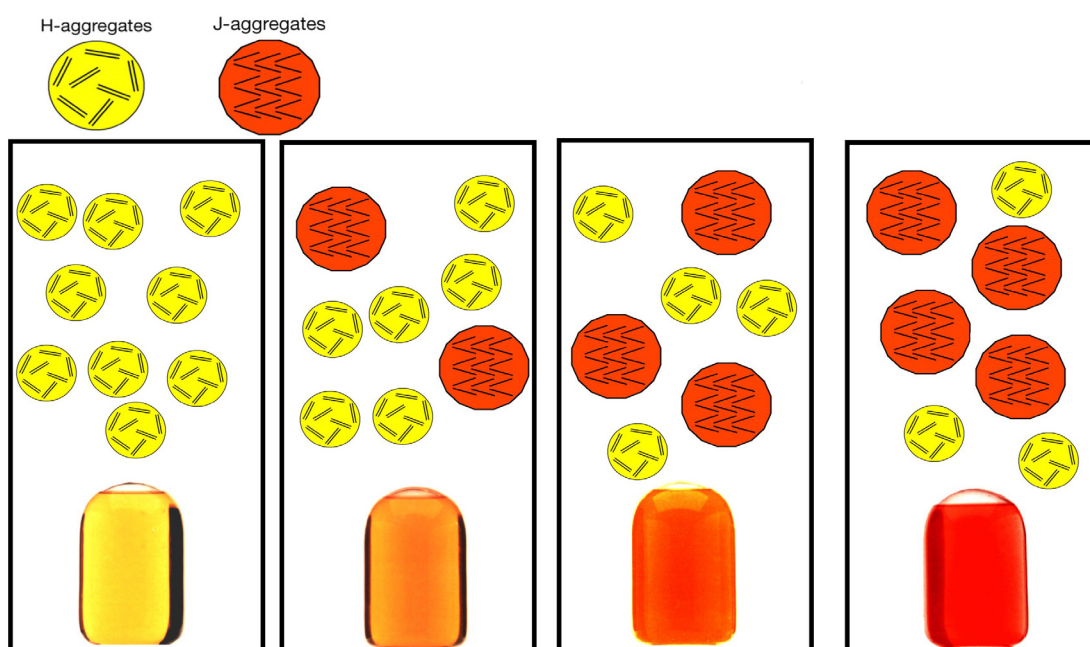


Figure 7-6: Structure model of the β -carotene microparticle system on the basis of the presented AUC results.

The different color of the samples does not originate from the intraparticle coexistence of H and J aggregates as previously assumed (Figure 7-2) (Auweter et al. 1999), but instead separate particles contain pure H or J aggregates and the concentration ratio between these particles determines the color of the final sample. Note the difference to Figure 7-2.

The peak around 520 nm shifts slightly to a lower wavelength with increasing sedimentation coefficient and the peak height also decreases. The same is true for the peak at 480 nm. Therefore, this excitation of β -carotene microparticles decreases with increasing sedimentation coefficient. For the peak at 450 nm, only the spectral shift to lower wavelength is observed with increasing sedimentation coefficient. The effects of this inhomogeneity were

not known before in such detail. We suspect that the displacement of the electronic potential energy surfaces changes, such that the Frank-Condon factors change for the vibrational progression, due to the changing incorporation of the chromophore into the partially crystalline assembly.

As discussed above, an overlay of the signal from β -carotene, gelatin and the dispersing agent was observed in the UV region. In this range, a shift of the peak maximum to higher wavelength with increasing sedimentation coefficient was detected. In addition, a drastic decrease of the peak height relative to the 450 nm peak was observed with increasing sedimentation coefficient. The particles that sediment more slowly show stronger UV absorption, which we attributed to a higher content of dispersing agent, and hence smaller particle diameters due to the formation process in co-precipitation (Auweter et al. 1999). To our knowledge, this is the first time that relatively small steps of spectral shift among an H aggregate have been shown for composite particles. All of the 200 different detected spectra follow the same trend. Although the spectral changes appear to be continuous, that does not exclude defined and different spectra for different particle populations as the detected raw signals are those of a sample band, which is broadened by polydispersity in size, composition and diffusional broadening.

Chapter 8 :Application of MWL-AUC in Chemistry: CdTe nanoparticles

8.1. Introduction

Semiconductors are of considerable importance in various key fields of (micro) electronic technology and nanotechnology. Semiconductor particles of nanometer dimensions change their optical and electronic properties with particle size, which allows for the design of tailor-made nanoelectronic materials, wavelength-selective sun blockers, color-tuneable and -adjustable LEDs, injection solar cells, and biological labels (Alivisatos 1996; Eychmüller 2000; Michalet et al. 2005).

Up to now, the dependence of the semiconductor band gap on particle size was determined for close-to monodisperse fractions of nanoparticles by independently determining the particle size and the absorption spectrum (Murray et al. 1993; Rogach et al. 1996). This is experimentally demanding and time consuming. Moreover, the correlation between absorption and particle size is impacted by the polydispersity of the samples. Especially for new systems these experiments are tedious and often impossible to perform since they require the synthesis of monodisperse nanoparticles with different sizes, which need to be determined in a second step. AUC is particularly well suited for determining the size of nanoparticles with the smallest accessible size, well below one nanometer (Cölfen and Pauck 1997; Cölfen et al. 2002). The very high resolution of AUC particle size distributions in the Angström range has already been demonstrated (Cölfen and Pauck 1997). On the basis of these findings, attempts have been reported to determine spectral changes with particle size by fractionation in a commercial AUC, however with severely limited resolution and quality (Cölfen and Pauck 1997; Niederberger et al. 2004). These previous limitations can now be overcome with the MWL-AUC, since the wavelength signal can now be acquired and interpreted simultaneously with the hydrodynamic signal (Bhattacharyya et al. 2006). Figure 8-1 shows the design and experimental raw data of this experiment.

8.2. Polydisperse TGA-capped CdTe nanocrystals

8.2.1. Experimental

The sample for the ultracentrifugation experiment was prepared by mixing eight different fractions of nanoparticles with absorbance maxima ranging from 450 to 620 nm. Absorbance spectra of eight initial colloids and the resulting mixture are shown in Figure 8-1(a) and 8.1(b). The final mixed solution had a particle concentration of ca. 3×10^{-5} M. For the details and synthesis and AUC method is explained in appendix.

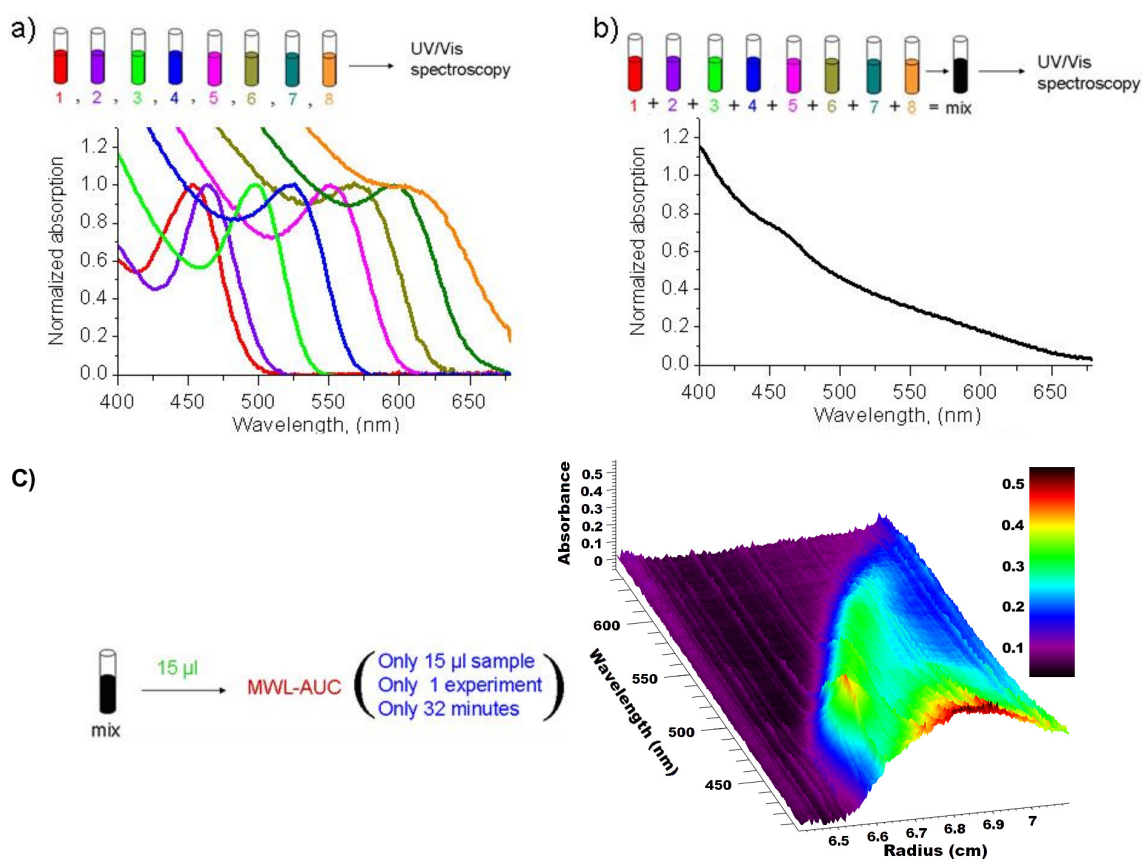


Figure 8-1: Presentation of CdTe experiment

(A) Eight different monodisperse CdTe samples were synthesized and the absorbance spectra of each sample were taken, spectra are normalized. (B) The particles were then mixed and the absorbance spectrum of the mixture was taken. (C) 15 µl of the mixture were measured by acquiring 20 sedimentation scans with the MWL-AUC. Shown here is scan 9 of 20 band sedimentation scans (scan time after 12 minutes). The red shift of the absorption with increasing radius is clearly visible in the experimental data, where the sedimenting boundary is found at increasingly higher radial positions with increasing wavelength. The color scheme encodes the absorbance. The 3D graph (c) illustrates the continuous quantum size effect detected already in a single MWL-AUC scan.

8.2.1.1. Analysis Method of the MWL-AUC data

To the best of our knowledge, our multiwavelength detector produces the first 3D data obtained in the history of AUC. Normally AUC data are 2D because they usually include one wavelength or other concentration-dependent signal. Consequently, all analysis software was based on single wavelength analysis. There is no AUC software that can analyze 3D data directly. That is why, at the beginning, we have performed an analysis with homemade programs and scripts omitting diffusion correction. We have obtained interesting results even without diffusion correction. These results are presented in sub-section 8.3.2. After we obtained interesting results with our analysis, Borries Demeler's group agreed to develop a software program that can further analyze 3D data including diffusion correction. They have developed their MWL module of the Ultrascan software further. Their findings are interesting and are presented in section 8.3.3 on diffusion corrected analysis.

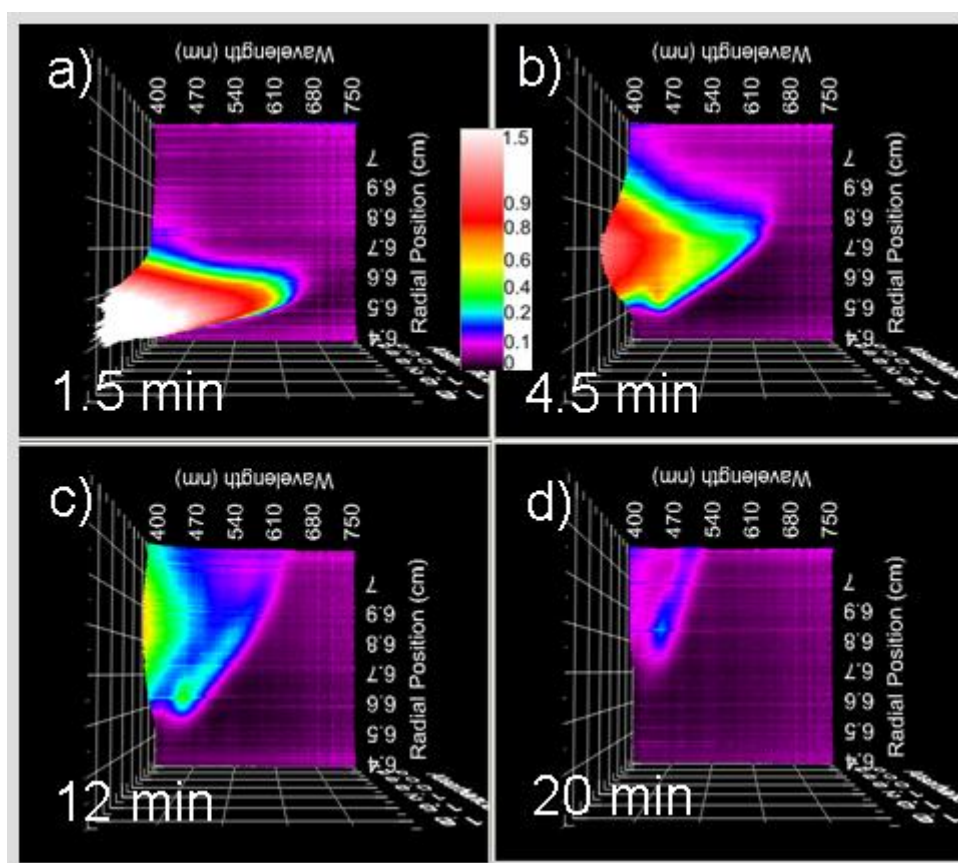


Figure 8-2 : Raw MWL-AUC Data: CdTe nanoparticles sedimentating with band centrifugation method; (Speed 55K, 20 radial scans 50 μ m step size)

8.2.2. Results and Discussions:

8.2.2.1. Raw MWL-AUC Data:

A general summary of the MWL-AUC experiment is shown in Figure 8-1. Eight different monodisperse samples of TGA-capped CdTe nanoparticles are synthesized (see sub-section 8.2.1). UV/Vis spectra of the samples are shown in Figure 8-1(a). All samples are mixed and UV/Vis spectra of the mixture are shown in Figure 8-1(b). Only 15 μl of the mixture sample is used for the whole experiment and the result was obtained in 32 minutes. Each scan produces 3D data with axes of wavelength, radius and absorbance. The ninth scan out of 20 is shown in Figure 8-2(c).

8.2.2.2. Analysis without Diffusion Correction

The cell was scanned 20 times with radial intervals of 50 μm , yielding a 3D moving image of sedimentation. Four of these scans can be seen in Figure 8-2. In one scan we have three dimensions, radial position, absorbance and wavelength. The radial axis can be converted to the particle size using the equations (Equation 8-1 and Equation 8-2) below:

$$s = \ln\left(\frac{\ln(r/r_m)}{\omega^2 t}\right)$$

Equation 8-1: Formula for calculation of the sedimentation coefficient

$$d_p = \sqrt{\frac{18\eta_s s}{(\rho_p - \rho_s)}}$$

Equation 8-2: Calculation of particle size from the sedimentation coefficient

where s : sedimentation coefficient, r : radial position, ω : angular speed, t : time, d : hydrodynamic particle diameter, η : viscosity of the solvent, ρ_p : density of the particle, ρ_s : density of the solvent.

One of the previous studies on the subject shows that these particles have spherical shapes in TEM measurements (Rogach et al. 2007). Therefore, Equation 8-2 can be used with the assumption that the particles are spherical. Hence, 20 scans in 3D with the axes of radial position, absorbance and wavelength (Figure 8-2) can be converted to 20 scans in 3D with the axes of particle size, absorbance and wavelength.

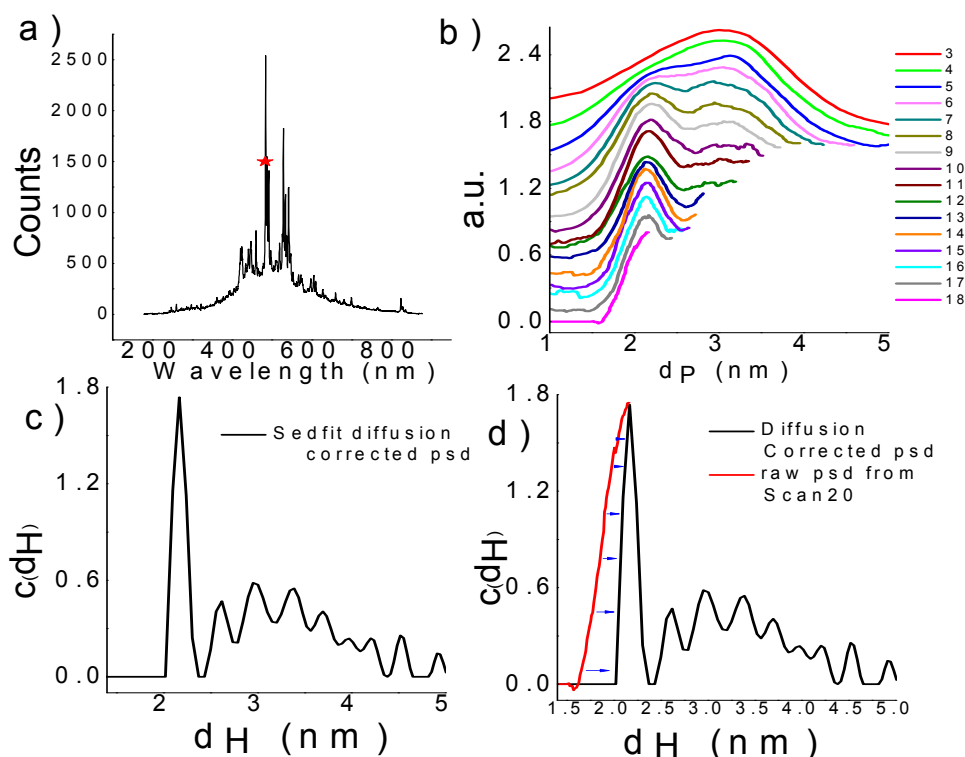


Figure 8-3 : Analysis of MWL-AUC data, reference intensity and psd

(a) Reference intensity taken from reference sector; (b) Apparent particle size distributions of CdTe nanoparticles detected at 483 nm obtained by conversion of radial position to particle size without any diffusion correction; (c) Diffusion corrected particle size distribution at 483 nm with Sedfit; (d) Graphs show particle size range correction for scan 20 without diffusion correction; red curve is scan 20; black curve is the same as (c).

To analyze the 3D data, as a first attempt, we focused on 2D slices of the scans. We selected one slice from each of the 20 scans for a single wavelength (483nm), due to the fact that we had a high intensity at 483 nm due to the spectrum of the Xenon lamp. The reference intensity of the experiment can be seen in Figure 8-3(a) with a red star at 483 nm. High intensity refers to a higher linear range (see sub-section 3.5.5). In Figure 8-3(b) we present 18 out of 20 2D slices of 20 3D data sets, which are the particle size distribution of particles obtained from different scans. However, it should be noted that this amount of slices corresponds to one slice out of 600, since we have selected only a single wavelength of 483 nm. Consequently, at each point in Figure 8-3(b) there is an additional wavelength axis that is not shown. At each point of particle size distribution, UV/Vis spectra of this point can be obtained, and this makes the MWL-AUC stronger over the other techniques.

Figure 8-3(b) presents the particle size distributions (psd) at different scans. In earlier scans, the psd looks bimodal and very broad. In later scans, the psd sharpens. This is due to the fact that the sedimentation transport prevails over diffusion transport, which is a well known effect in AUC. Since sedimentation is proportional to time but diffusion only to the square root of time. As a result, diffusion is more dominant in earlier scans whereas sedimentation is more dominant in later scans. The diffusion smears the bands of particles with different size. Therefore, we need to eliminate diffusion as much as possible. Having this fact in mind, we have concluded that the later scans are more valuable to obtain the psd and the UV/Vis spectra but bigger particles have already sedimented.

As is shown in Figure 8-3(b), every scan has its particle size range and later scans have a comparably limited particle size range. For example, the 3 nm particle cannot be seen in scan 18, because the 3 nm particle has already sedimented at scan 12. It is better to take the UV/Vis spectra of 3 nm particles from scan 12, since the latest scan where the 3 nm particle is visible in scan 12. In any UV/Vis spectrum of 3 nm particles from earlier scans the effect of diffusion is higher. Therefore, we decided to take the UV/Vis spectra of a particle from the latest scan possible. We call this the *latest scan principle* (lsp). We decided to form combined 3D data from the 20-scan set of 3D data, in the light of the latest scan principle. Thus, we get one UV/Vis spectrum for each particle instead of 20. Again with this combined 3D data (Figure 8-4), we obtain one psd at one wavelength instead of 20 psds (see Figure 8-3(b)). With this combined 3D data, we can assign any particle size to its UV/Vis spectra.

In order to obtain combined 3D data from 20 3D data, we started with scan 18, which is the latest scan in the linear range. Scan 18 has a particle size range from 1.5 nm to 2.3 nm. However, diffusion corrected particle size distribution at the same wavelength has a range minimum 2.03 nm (Figure 8-3(c)). Hence the range obtained below 2.03 nm at scan 18 is a result of diffusion broadening.

Consequently, we applied particle size range conversion for scan 18 to obtain a realistic particle size range. We converted the 1.500 nm–2.16 nm (0.66 nm interval) range of the 18th scan to a range of 2.02 nm–2.16 nm (0.14 nm interval), which is taken from the non-diffusion corrected raw data to the corresponding particle sizes in the diffusion corrected psd.

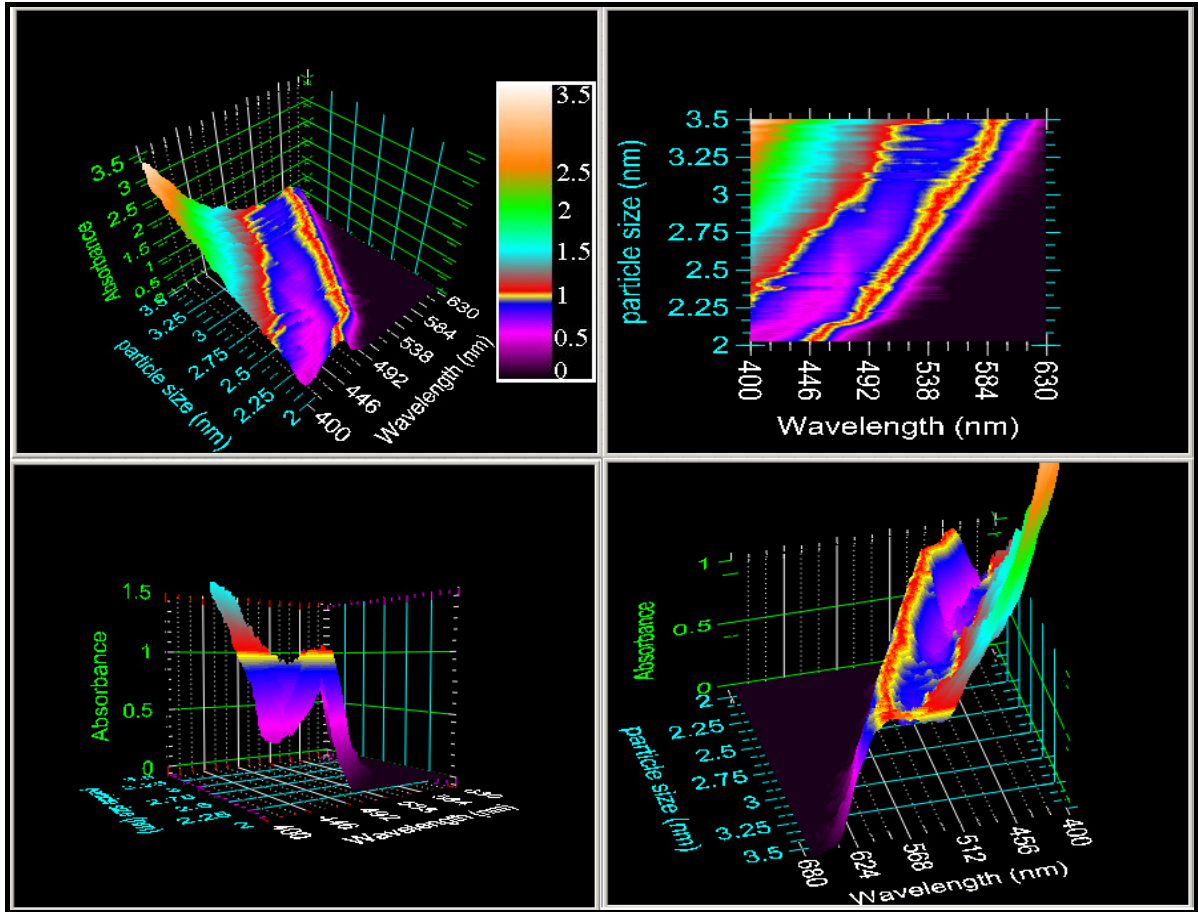


Figure 8-4: Combined 3D data, with axis, particle size, abs, wavelength

3D representation of the quantum size effect in a CdTe mixture consisting of eight monodisperse fractions. Spectra are normalized and the quantum size effect can be seen. All subgraphs are the different views of the same graph from different directions. The graph contains about 150 spectra. This corresponds to 0.1 Angstrom intervals in terms of particle size.

$$ps_{new} = ((ps_{old} - 1.5(nm)) * (0.14(nm) / 0.66(nm))) + 2.02(nm)$$

Equation 8-3: Particle size range correction equation for small particles at scan 18

Where ps_{new} : new particle size for the point; ps_{old} : particle size point that is in scan 18.

With the help of Equation 8-3, every particle size point at scan 18 in the range 1.500 nm–2.16 nm can be converted to a point in the range 2.02 nm–2.16nm. This corrects the particle size range of scan 18. The conversion is shown in Figure 8-3(d).

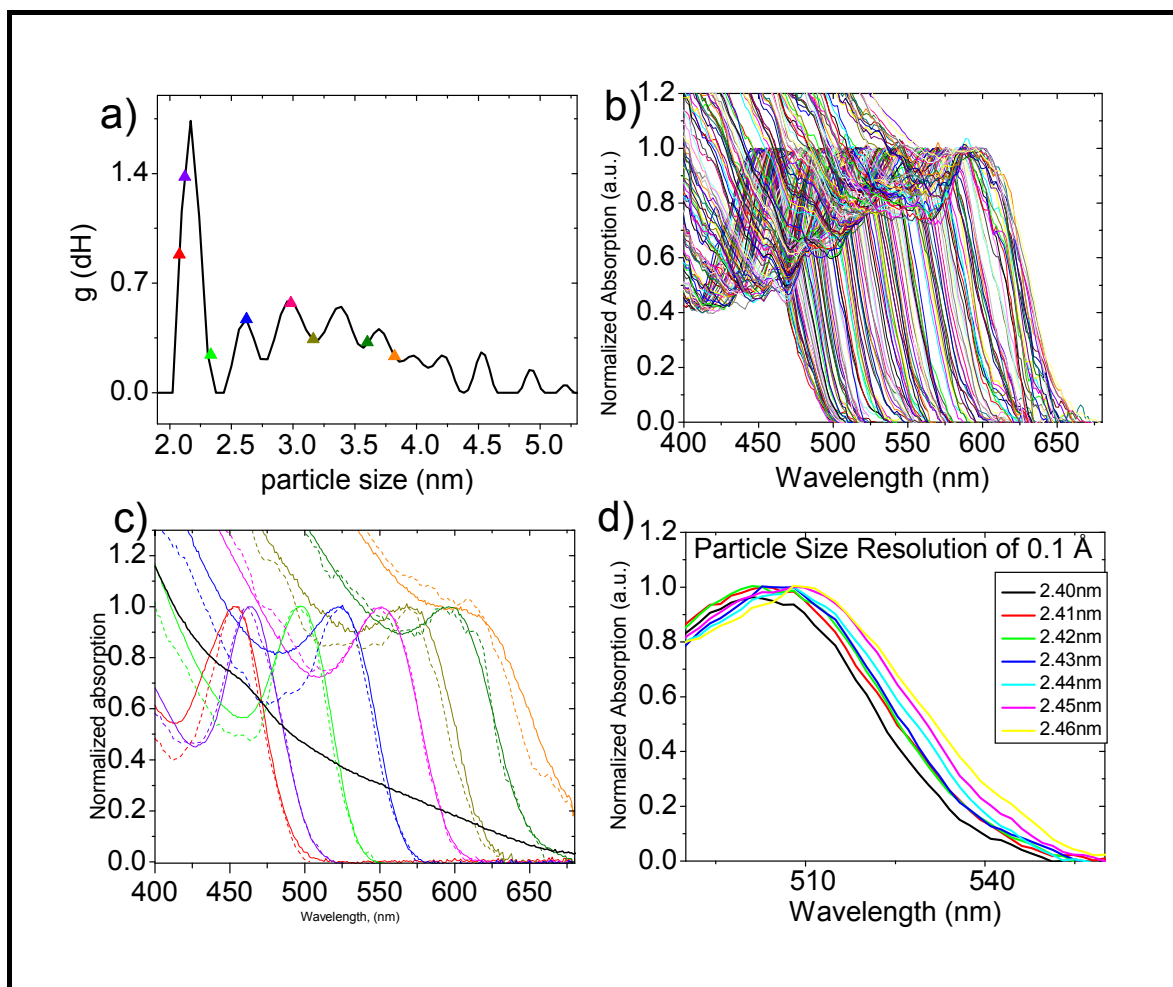


Figure 8-5: Spectral comparison of sample

(a) Particle size distribution calculated with the Sedfit program at 483 nm, triangles are the points whose spectras are shown with dashed lines in Figure 8-5(c), (b) 150 normalized UV/Vis spectra, from 2.02 nm to 3.5 nm with a resolution of 0.01 Å. Peak range changes from 444 nm to 595 nm. (c) UV/Vis spectra of the eight initial samples, from left to right, red: sample1; purple: sample2; green: sample3; blue: sample4; magenta: sample5; olive: sample6; dark yellow: sample7; orange: sample8, black is the spectrum of the mixture, solid lines indicate spectra before mixing and dashed lines are from combined 3D data with values shown in Figure 8-5(a) (triangles); d) Spectra with particle size resolution of 0.01 Å

After conversion we obtain the corrected particle size range and the UV/Vis spectra of each particle at scan 18. We keep this (corrected scan 18) data as the first part of our combined 3D data. Then we shift to scan 17, where we have the distribution of larger particles and their UV/Vis spectra, which were already sedimented in scan 18. We did not apply any range conversion to scan 17. Because for the particle size range >2.16 nm, it is not clear if the data point in the non-diffusion corrected distribution needs to be corrected to a lower or higher particle size. After scan 17, we shift to scan 16, and obtain the distribution of particles that were already sedimented in scan 17 and their UV/Vis spectra. We continue like this until the

UV/Vis spectra of CdTe nanoparticles do not show any reasonable spectra anymore. As a summary, this process includes the particles with sizes in the ranges: 2.02–2.16 nm from scan 18 with particle size range corrected; 2.165–2.333 nm from scan 17; 2.343–2.433 nm from scan 16; 2.444–2.52 nm from scan 15; 2.528–2.606 nm from scan 14; 2.61–2.668 nm from scan 13; 2.677–2.75 nm scan 12; 2.788–3.148 nm from scan 11; 3.15–3.284 nm from scan 10; 3.296–3.464 nm from scan 9; 3.467–3.513 nm from scan 8. At the end, we obtain combined 3D data, for a particle size range from 2.0 nm to 3.5 nm, a wavelength ranges from 350 to 620 nm, and absorbance data. In order to make the combined 3D data presentable, we normalized the absorbance of the peak point of the UV/Vis spectra to 1 in all 150 spectra. The combined 3D data is presented in Figure 8-4.

Figure 8-4 clearly shows the quantum size shift. This is a 3D plot of the combined 3D data explained above. The plot has an axis of particle size from 2 to 3.5 nm. In this range 150 different UV/Vis spectra were recorded. Consequently, particle size resolution is about 0.01 Å. Wavelength range is from 400 nm to 620 and its resolution is about 1 nm. Absorbance was normalized in order to visualize the data. Normalization was done to produce the peak point of the spectrum¹. All the information used here was obtained from a 15 µl sample in only 32 minutes. This shows the power of the MWL-AUC as an analytical technique in the field of semiconductor nanoparticles.

As a first step of reliability analysis of our combined 3D data, we compared this combined data with UV/Vis spectra of initial monodisperse samples. From 2 nm to 3.5 nm, we had 150 UV/Vis spectra. These 150 spectra are shown in Figure 8-5(b). Among these 150 spectra, we have selected the particle sizes whose spectra fit the spectra of eight monodisperse samples that were synthesized in the beginning (Figure 8-1(a)) and which are close to theoretically expected values much better than the previous results (Figure 8-6(b)). The selected particle sizes are shown as triangles in Figure 8-1(a). On the other hand, Figure 8-3(c) shows their spectra with dashed lines (Figure 8-5(c)). Solid lines are identical to the plots of Figure 8-1(a). As a result, Figure 8-5(c) shows that we reproduce the same spectra. Thus, MWL-AUC is able to differentiate the mixture into its initial monodisperse components.

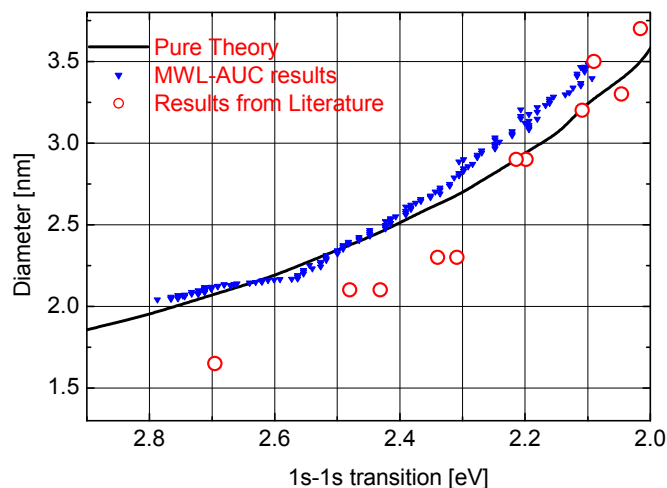


Figure 8-6: Comparison of the results with theory

The black line represents the theoretical curve (Rogach et al. 2007); open red circles are previous experimental results from the literature (Rogach et al. 2007); blue triangles are MWL-AUC data without diffusion correction.

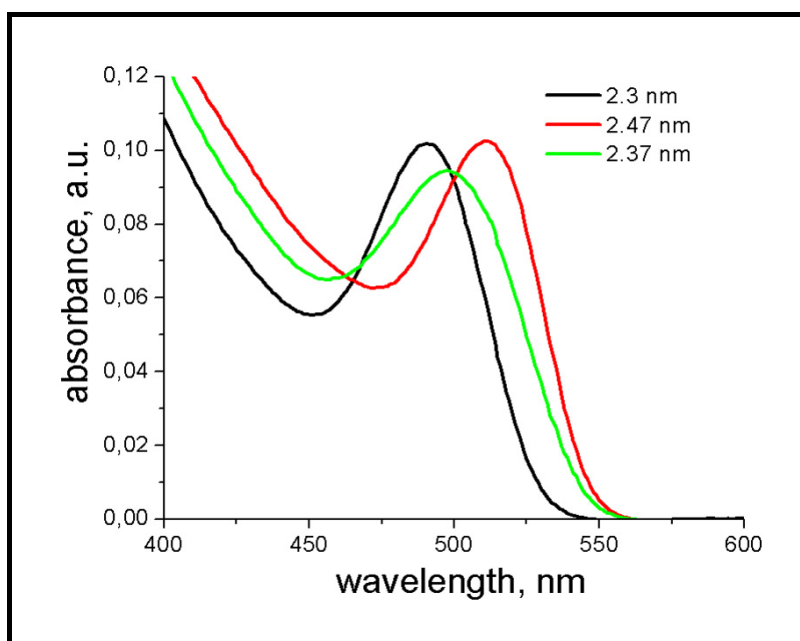


Figure 8-7 : Mixture effect of CdTe

Absorption spectra of two CdTe nanoparticle solutions of the average sizes of 2.3 (black line) and 2.47 (red line) nm and the spectra of their 1:1 mixture (green line). The latter shows the additivity of the spectra and an average particle size of 2.37 nm. The sizes are evaluated based on the calculated curves from refs (Rogach et al. 2007; Rogach et al. 1996)

The comparison of our 150 different spectra with the theoretical curve is shown in Figure 8-6. The black curve is a theoretical curve that was calculated by Rogach and colleagues without any empirical influence (Rogach et al. 2007; Rogach et al. 1996). Open circles are the

previous experimental points that were achieved so far. The red curve is the fit of previous experimental results that are shown as open circle points. The blue triangles are the results of our 150 spectra. The 1s–1s transition is calculated from the UV/Vis spectra of the sample. Wavelengths of peak points were converted to energy with the help of Planck's formula. The diameter of each particle is taken from our combined 3D data.

The particle size resolution of 0.01 Å in Figure 8-4 is an interesting result. Is the resolution of 0.01 Å realistic since the radius of Cd^{2+} and Te^{2-} are 0.095 Å and 0.0221 Å. This phenomenon can be explained by a mixture effect. Mixture effect is seen in Figure 8-7. In this figure, two fractions of particles with sizes of 2.3 nm and 2.47 nm are mixed. The spectra of the mixture are identical to spectra of a particle with 2.37 nm. In fact, the particle of size 2.37 nm does not exist; it is only a statistical effect. This effect can explain the resolution of 0.01 Å as, in the case of a particle mixture the spectrum will correspond to the weighted average particle size. The additivity of the spectra also allows us to calculate the average particle size from the maximum in the UV-Vis absorption spectrum for a mixture, as demonstrated in Figure 8-7. This opens up the possibility of calculating the particle size from each of the experiments (Figure 8-6), an approach allowing the direct correlation of the optical properties with the particle size. Only the band gap positions of the resolved species should be plotted in this plot. For each of these spectra the first absorption maximum corresponds to the energy of the 1s–1s transition or in other words to the band gap position. The bandgap-size data points are plotted in Figure 8-6. Those are compared with previously reported experimental data (estimated from the statistical analysis of the TEM images) and the calculated values as described in (Rogach et al. 2007; Rogach et al. 1996). From Figure 8-6, it can be seen that these data points fit the theoretical curve for CdTe (Rogach et al. 2007) very well and much better than the conventionally determined particle size dependence of the band gap (Rogach et al. 2007). In the presented experiment, we have 150 such correlations available. This number can be increased by scanning the solution column in the ultracentrifuge cell not with a 50 µm step size as is current practice (ca. 150 data pairs) but instead with 10 µm or even 1 µm, yielding 750 or 7500 data pairs respectively in a single experiment. Thus, the full particle size dependence of the band gap becomes directly experimentally accessible for the first time with steps as small as the addition of one Cd^{2+} or Te^{2-} ion to an existing particle.

8.2.2.3. Analysis with Diffusion Correction

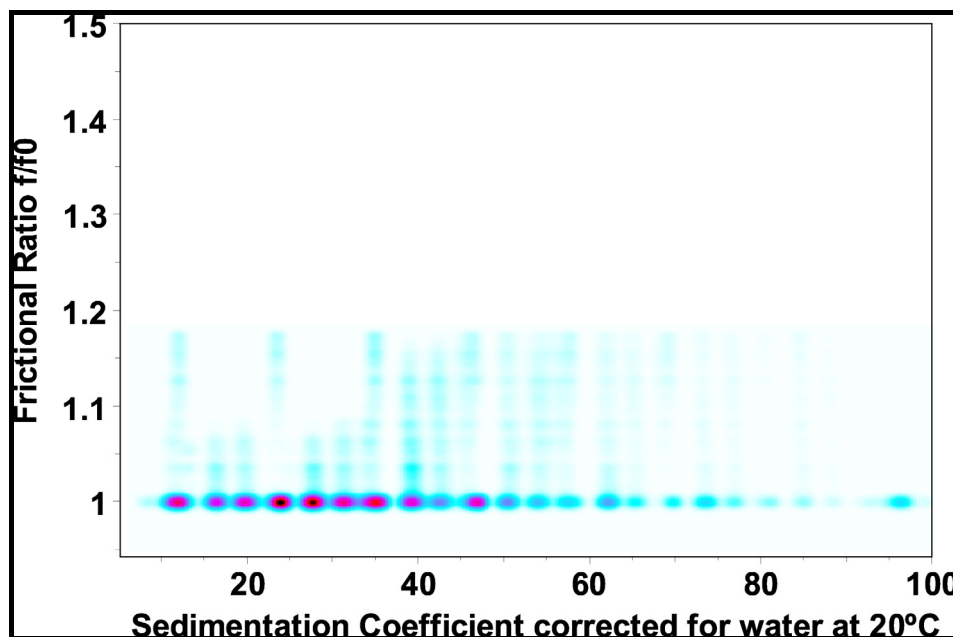


Figure 8-8 : Result of 2DSA analysis

Frictional ratio plotted for the diffusion-corrected sedimentation coefficient distribution for the CdTe mixture as a result of two-dimensional spectrum analysis. It is obvious that all particles in the discrete distribution of particles have a spherical shape ($f/f_0 = 1$).

Diffusion causes broadening of the sedimenting boundary (Figure 8-3) which makes the particle size distribution wider and obstructs from identifying individual species in a mixture. There are various strong algorithms to correct the diffusion effect. Recently, two-dimensional spectrum (2DSA) analysis has been developed (Brookes et al. 2006). With the help of Emre Brookes, the 2DSA has been employed to resolve the heterogeneity and analyze the MWL-AUC data. This method models sedimentation and diffusion processes for each species in the mixture with ASTFEM-RA (adaptive space-time finite element method-reversible associations) solution (Cao and Demeler 2008) of the Lamm equation (Equation 2-12). The method is built for a regular grid of species extending over all species contained in a mixture. By performing a non-negatively constrained linear least-squares optimization implemented on a super computer, it finds the amplitudes of the species that are present (Brookes and Demeler 2008).

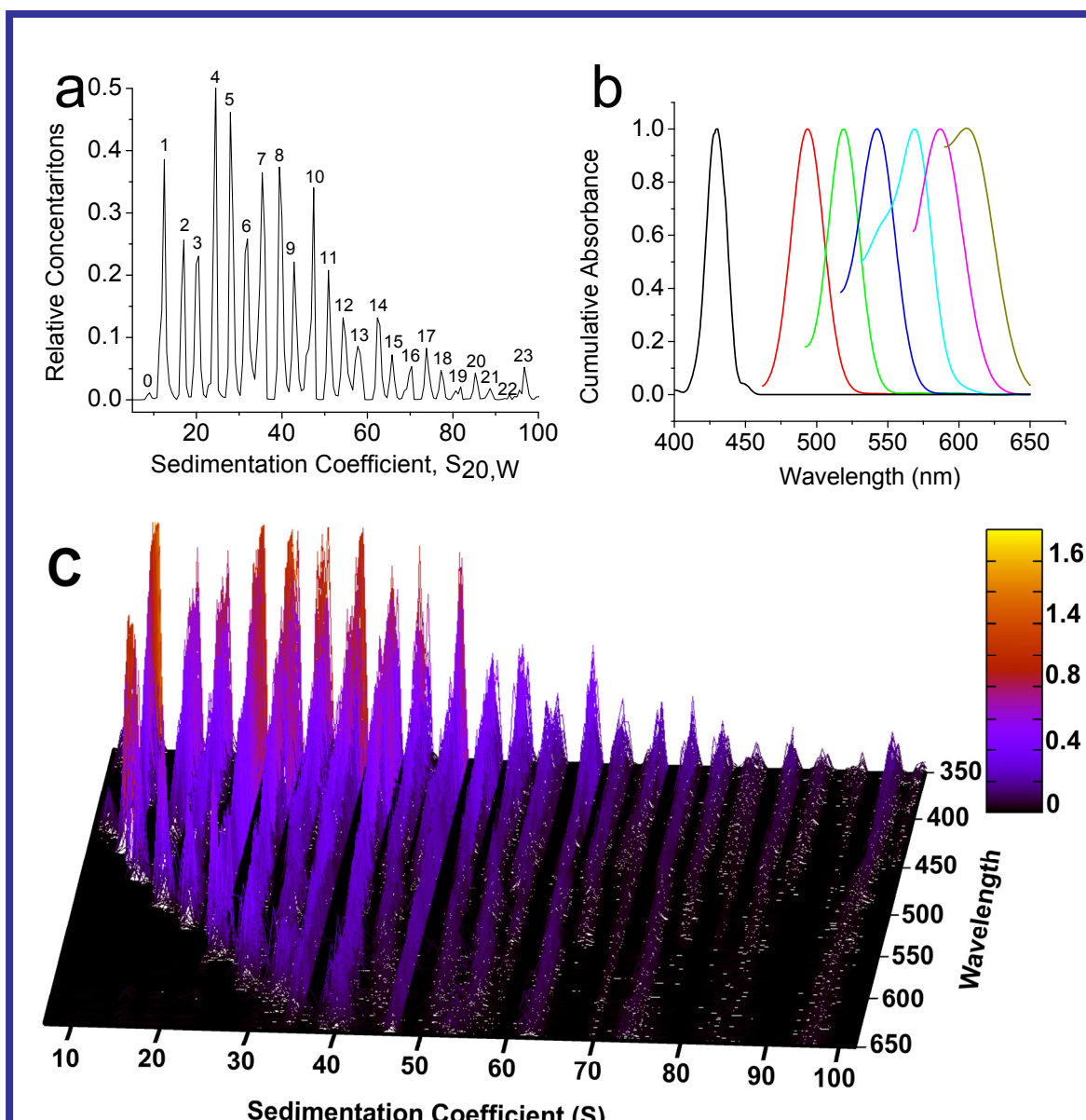


Figure 8-9: Diffusion-corrected results of the CdTe experiment

(a) Composite sedimentation coefficient ($S_{20,W}$: sedimentation coefficient corrected to 20°C and water density and viscosity) distribution plot of relative concentrations for all species and all wavelengths. The peak height represents partial concentration. Each peak is the summation of all concentrations from all wavelengths. The different species are labeled with numbers. Over 20 species can be clearly resolved. (b) The corresponding UV-Vis spectra for the first seven species. (c) Diffusion-corrected sedimentation coefficient distribution after 2DSA (Brookes et al. 2006) from 350 nm to 650 nm. The spectra are terminated at lower wavelengths due to higher absorption that exceeds the linear range. The Z-axis (peak height) indicates the partial concentration of each species in absorbance units. Data from all wavelengths were analyzed independently and showed identical solutes but with different partial concentration. The red shift with increasing particle size is clearly visible in the low S-value range (left side of plot) and extends from about 400 to 650 nm and 8 to 40 S. Smaller species are more abundant than larger species. The 2DSA analysis results in a clear baseline separation of 24 individual species consistently reproduced for all wavelengths. Overall analysis that is shown in this figure was performed by Borries Demeler and Emre Brookes using a modified ultrascan software for MWL-AUC data.

The frictional ratio (f / f_0) gives information about the shape of the particles. 2DSA has been performed for all wavelength separately and independently. To calculate the confidence limits for all determined hydrodynamic parameters of %95, Monte Carlo analysis has been performed (Demeler and Brookes 2008).

Results of the analysis gave very define and monodisperse species. According to these results, species which are below 40 S, have defined UV/Vis spectra. These species clearly prove the blue shift of the CdTe nps due to its size (Figure 8-9(c)). Smaller maxima in the spectra indicate a high monodispersity. Concentrations of species which are larger than 10-24, are less than %5, so they are also not very well resolved. Species 0, which is a magic cluster (Figure 8-12(a)), is shown in Figure 8-9(a). The relative low concentration of this species is due to its reactivity and we think that it plays a key role in growth mechanism (Figure 8-12) and therefore it is important to detect this smallest species.

An interesting property of the 2DSA analysis is that it gives the same sedimentation coefficients at different wavelengths (Figure 8-9). This is important because, each wavelength is analyzed independently. Therefore, the sedimenting coefficient distribution which is shown in Figure 8-9(a) is a very robust result. The first seven individual species's UV/Vis spectra are shown in Figure 8-9(b), which also show the blue shift of spectra.

8.2.2.4. Growth mechanisms of CdTe nanoparticles

Nearly periodic discrete species, as shown in Figure 8-9(c), is an unexpected result in terms of the growth mechanism of CdTe nanoparticles (nps), because the literature (Rogach et al. 2007) suggests Ostwald ripening for the growth mechanism of these nps. The Ostwald ripening mechanism cannot explain periodic discrete species in a polydisperse solution. Nearly periodic discrete species hint at a different particle growth mechanism. This section investigates the details of the growth mechanism of TGA capped CdTe.

Twenty-four periodic discrete species (Figure 8-6(c)) have S values ranging from 8.7 to 96.1 with intervals of 3–4 S. To further quantify the growth mechanism of CdTe nps, it is necessary to convert S values to molecular weight.

$$M = \frac{sRT}{D(1 - \bar{v}\rho_s)}$$

Equation 8-4: Svedberg Equation

Where s: sedimentation coefficient; M: molecular weight; T : temperature; R: gas constant; D : diffusion coefficient; \bar{v} : partial specific volume of particle; ρ_s : density of solvent.

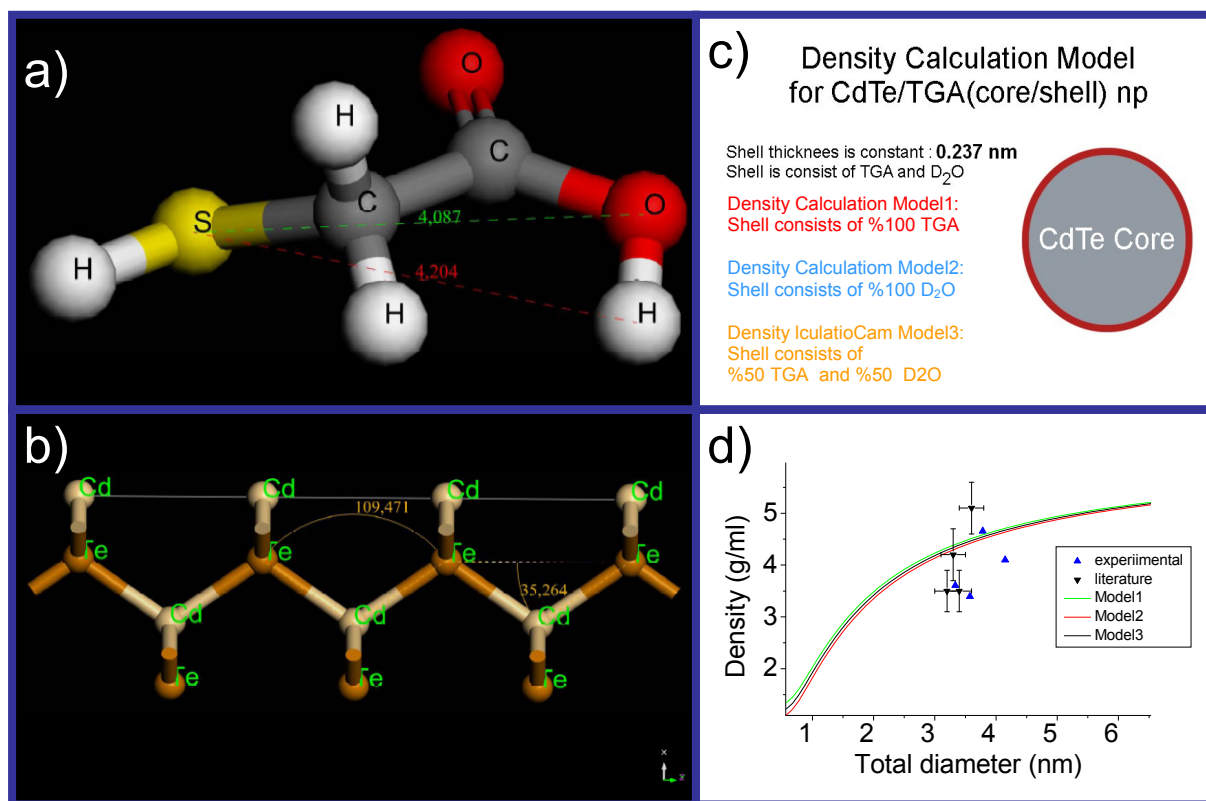


Figure 8-10: Density Model of CdTe/TGA

(a) Length of the TGA molecule that is calculated with MS-Modeling (Accelrys), 4,087 Å is without hydrogen; 4,204 Å is with hydrogen (chemical bonding to CdTe is assumed via S, which eliminates H of the –SH group) (b) Crystalline structure of CdTe, with angles between atoms; (c) Density model parameters; (d) Particle size dependence of TGA capped CdTe, blue triangles(experimental) are our measurements with density meter, black triangles(literature) with error intervals are from Lars Börger's PhD work. Model1, model2 and model3 are plotted with different colors.

The diffusion coefficient can be calculated with the equation below(Equation 8-5):

$$D = \frac{RT}{N_A f}$$

Equation 8-5: Calculation of diffusion coefficient

where f : the frictional ratio; N_A : Avogadro constant.

f/f_0 is 1 for all 24 species (Figure 8-8), thus the equation below (Equation 8-6) for spherical particles can be used to calculate f.

$$f = 6 \pi \eta r$$

Equation 8-6: Friction coefficient equation

where r : radius of particle; η : is viscosity of solvent.

The only missing parameter to calculate M with Equation 8-4 is the specific volume of the particle, which is the reciprocal of the particle density ρ_p . The bulk particle density of CdTe is 6.2 g/ml, however in the nano range, the particle size density deviates from bulk due to the different density of the shell which becomes significant for small particles (Börger *et al.* 2000). Hence in nanoparticles the density depends on the particle size. The relation of the particle size to the density is needed to calculate the molecular mass of discrete species.

Börger *et al* 2000 (Börger 2000), tried to calculate the particle size dependence of TGA capped CdTe nps with using a combination of Field Flow Fractionation FFF and analytical ultracentrifugation. He used particle size from FFF and sedimentation coefficient from AUC and combined them to determine the density of differently sized CdTe nps. His results are shown in Figure 8-10(d) with error intervals as black triangles. It was tried to measure the particle density of different monodisperse samples with using a density meter. Our values are shown as blue triangles in the graph. Börger's and our results shows a high error but are in the same range.

To get a more reliable particle size dependence of the density, it was tried to from a mathematical density model of CdTe/TGA using a core and shell model. The first parameter to determine is the thickness of the TGA shell. Its thickness depends on the length of TGA and also its angle with the core. TGA was constructed with MS-Modelling Software Ver4.1 (Accelrys). Distances were measured as shown in Figure 8-10(a). The length of the TGA molecule is 0,4204 nm in the protonated form and 0,4087 nm in deprotonated form. Since all of our solutions are basic and also the synthesis method includes basic pH range of pH 11.2-13.4 (Gaponik *et al.* 2002), TGA can be assumed to be deprotonated. This was also tested by checking the pH of the final solutions which was ranges from pH 9 to 13. We have used 4.1 Å as the length of 1 TGA molecule. Secondly we needed to determine the angle with which TGA attached to the surface Cd atom. The exact crystalline structure of CdTe, core shell nanoparticles has not been published yet. After extensive study of the magic cluster of CdTe/2-mercaptoethanol, Rockenberger *et al* (Rockenberger *et al.* 1998) concluded that its

structure is most probably similar to CdS structure with a different crystalline structure at core. Herron *et al* (Herron et al. 1993) and Vosmeyer *et al* (Vosmeyer et al. 1995a; Vosmeyer et al. 1995b) published the exact crystalline structure of CdS nanoparticles. In the structures it is shown that the stabilizer has an angle to the particle surface, which follows the core crystalline structure. The crystalline structure of bulk CdTe is shown in Figure 8-10(a). Rockenberger *et al* (Rockenberger et al. 1998) showed that the ligand is attached to surface Cd and that there are 2 ligands attached to 1 surface Cd atom. Therefore, the ligand most probably has the same angle as Cd to Te in the crystal lattice. These angles are calculated by MS-Modeling(Accelrys) and it is 35.2°. So we calculated the shell thickness as $0.4087\text{nm} \cdot \sin(35.2)$ which is 0.237 nm. Thus we took 0.237 nm as the thickness of the shell. We took this distance as constant. We know the core density as 6.2 gr/ml which is the density of bulk CdTe. Since we do not have exact information about the shell density, we employed three different models that are shown in Figure 8-10(c). With this conclusion, a density calculation model of TGA-capped CdTe nanoparticles have been developed .

Figure 8-10(d) illustrates the mathematical density calculation model that is used to obtain the particle size dependence of density. Models 1, 2 and 3 (Figure 8-11(c-d) produced very similar results, which indicates that the D₂O content of the shell does not have a big effect on particle density. This can be explained by the high density of the core CdTe. To further calculate the molecular masses of the periodic 24 discrete species (Figure 8-6(c)), Model 3 is used (50% TGA-50% D₂O). Molecular masses are calculated with Equation 8-4. The calculated molar masses are shown in Figure 8-11 as blue points. Molecular masses range from 17500 g/mol K Dalton to 373000 g/mol with nearly constant difference. The polynomial fit of the points gives an equation below (Equation 8-7):

$$M_x = 14343(g/mol) + 10358X(g/mol) + 230X^2(g/mol)$$

Equation 8-7: Equation obtained from Figure 8-12
where X is the species number (Figure 8-11(a)).

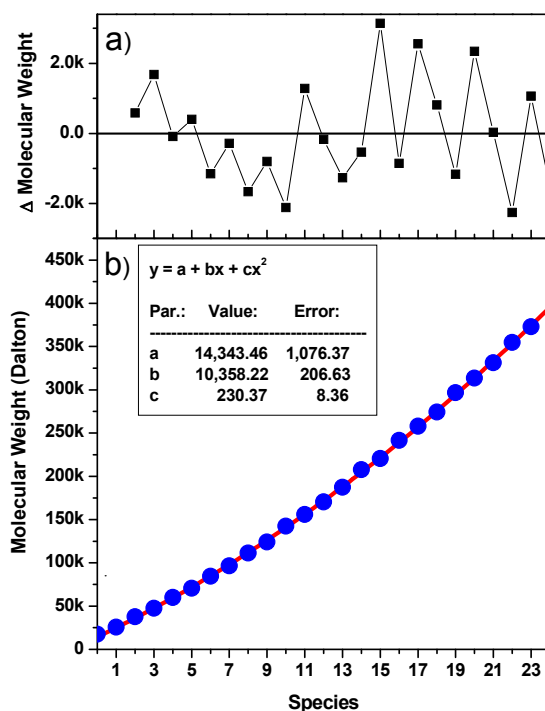


Figure 8-11: Molecular weight of 24 species (0-23)

(a) Residuals for fit in Figure 8-12(b); (b) Molecular weights of 24 discrete species (Figure 8-9(a)) calculated with the density calculation model3; red line is the polynomial fit of the molar masses of species.

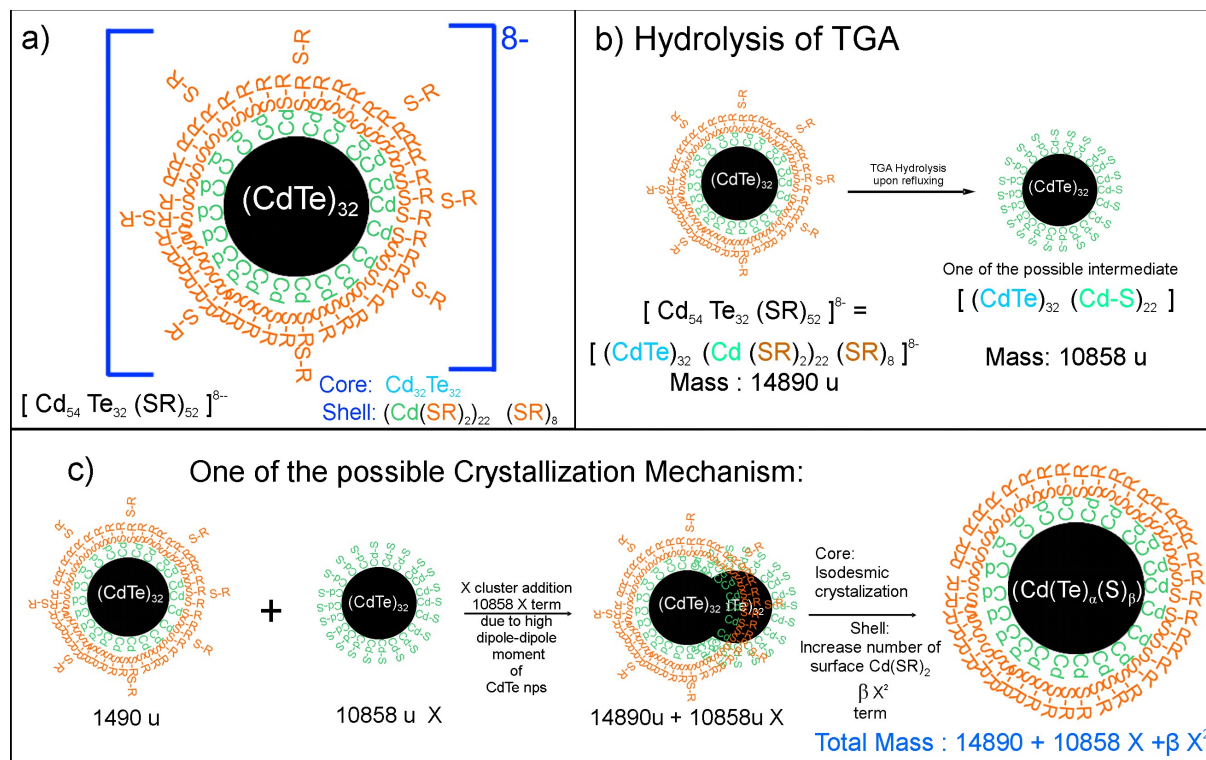


Figure 8-12: One of the possible mechanisms of CdTe nanoparticle crystallization

(a) One of the possible structures of a $[Cd_{54}Te_{32}(SR)_{52}]^{8-}$ cluster, S-R is the thiol that is used in synthesis; (b) One of the possible mechanisms of TGA hydrolysis; (c) Cluster coalescence mechanism.

Near to constant periodicity of molar masses is much better illustrated in Figure 8-11. There is a linear term of 10358 g/mol and a square term of 230 which is small in comparison with the linear term. A constant molar mass difference about 10400 g/mol between the detected species shows that the CdTe nanoparticles do not grow by classical crystal growth, implying ion by ion deposition onto the growing CdTe nanoparticle. Instead, the constant molar mass difference between the different, strictly monodisperse, growth species shows a nanoparticle-based growth mechanism. In our case, attaching nanoparticles are $[\text{Cd}_{54}\text{Te}_{32}(\text{SR})_{52}]^{8-}$ with a molar mass of 14890 g/mol with a deprotonated TGA stabilizing ligand. The smallest detected species is a 17500 g/mol, species which then grows by subsequent addition of one $[\text{Cd}_{54}\text{Te}_{32}\text{S}_{22}]$ (Figure 8-12). This growth mechanism was already detected earlier for Pt nanoparticles (Cölfen and Pauck 1997). The applied two-dimensional spectrum analysis is able to reveal the particle shape as well as the sedimentation coefficient distribution of the sample. As Figure 8-9 shows, for all wavelengths, consistent data were obtained, which reveal the discrete species already shown in Figure 8-8, but as additional information their spherical shape is revealed as $f/f_0 = 1$. Therefore, coalescing nanoparticles must have the opportunity to fuse and minimize their surface to a spherical shape later on. Having all this information, we illustrate one of the possible growth mechanisms in more detail in Figure 8-12.

Extensive study of the $[\text{Cd}_{54}\text{Te}_{32}(\text{SR})_{52}]^{8-}$ cluster in literature shows that the structure is; CdTe core, $\text{Cd}(\text{SR})_2$ layer at shell (Rockenberger et al. 1998). The cluster has a molar mass of 14890 g/mol. The exact crystalline structure is not yet published, but EAXS analysis (Rockenberger et al. 1998) shows a structure similar to that in Figure 8-12(a). Illustrative Figure 8-12(a) shows 32 units of core CdTe, 22 units of $[\text{C}(\text{SR})_2]$ in shell and 8 S-R^- in shell. Hydrolysis of TGA is also reported in TGA-capped CdTe nps which results in breaking of the S-R bond (Rogach et al. 2007), one of the possible mechanisms is shown in Figure 8-12(b). We suggest a possible intermediate stage in the process, which is the result of hydrolysis of all TGA in the shell. The intermediate species shown in Figure 8-12(b), has a molar mass of 10858 g/mol. Our cluster coalescence mechanism (Figure 8-12(c)) consists of the addition of intermediate species to the $[\text{Cd}_{54}\text{Te}_{32}\text{S}_{22}]$ cluster. After coalescence of two clusters, number of surface Cd atoms increases, and surface is covered by $\text{Cd}(\text{SR})_2$ minimization occurs because of the new surface-to-volume ratio. Each new coalescence of the cluster adds mass of 10858 g/mol to total mass. In the core of structure, CdTe crystals

dissolve and form a bigger CdTe crystalline core. These type of reactions are called isodesmic reactions. Isodesmic reactions are also common in nature, and the type that is presented here is called mesonucleation (Cölfen and Antonietti 2008). This may explain the linear 10358 X (g/mol) term in Equation 8-7, because the number 10860 of clusters that coalesce is linear to the species number. An increase in the number of surface Cd atoms, result in the increase of surface Cd(SR)₂ complex this may explain the 230 X² term in Equation 8-7. The total equation for molar mass calculation according to the mechanism in mechanism in Figure 8-12 results in the equation (Equation 8-8) below:

$$M_x = 14480(g/mol) + 10858X(g/mol) + \beta X^2(g/mol)$$

Equation 8-8: Equation of total particle mass due to growth mechanism (Figure 8-12)

Further extensive literature research on the growth mechanism of CdTe revealed small number of references indicating an aggregation mechanism at different conditions. However, the reported results are not as exact as ours, so the main accepted mechanism for CdTe growth was still Ostwald ripening. Therefore, a vast number of references refer to Ostwald ripening.

Dagtepe *et al* (Dagtepe et al. 2007), studied the CdTe growth mechanism at high temperature anhydrous synthesis. High temperature sythesis was used at 200 °C with in presence of hexadecylamine (HDA), hexylphosphonic acid (HPA), and trioctylphosphine oxide (TOPO) which is a different synthesis in comparison to the synthesis that we have used. UV/Vis spectra of the reactor solution were taken continuously during the synthesis. Multiple peaks were observed which was referred to quantized growth mechanism of CdTe. It was claimed that discrete species exists with UV/Vis absorption peaks of 410, 449, 491, 501, 539 and 588 nm. Species with 449, 539 nm and 588 nm peaks were observed with HRTEM. These species showed multiple domains which support the idea of aggregation based mechanism. However, the species with 501 and 449 nm peaks could not be solved with HRTEM. Also band gap dependence on particle size (as Figure 8-6) did not fit to the theoretical curve instead an empirical curve is plotted. Magic cluster were observed after stopping the reaction in the beginning, this yield CdTe with absorption peak at about 430 nm. Three different mechanism were claimed, monomer assisted growth, coalescence of magic-size CdTe and monomer with coalescence assisted growth of CdTe. They prefer the coalescence growth of the system, but

experimental results are not as detailed as in our case. Also a recent publication of Dagtepe *et al* (Dagtepe and Chikan 2008), computer simulation is performed for growth mechanism. As a result, coalescence mechanism of one magic cluster is ignored, and coalescence of two different magic clusters is introduced. But the existence of second magic cluster can not be shown experimentally. They also informed that observed sequential appearance of absorption peaks in reaction chamber is not due to aggregation mechanism but magic cluster formation.

An important publication about CdTe nanoparticle based structure formation is Tang *et al* (Tang et al. 2002). The authors showed how TGA capped CdTe nanoparticles forms 1D single crystal nanowire at room temperature after partial removal of the stabilizer via directional aggregation based mechanism. The reaction takes seven days at room temperature. They calculated the dipole-dipole moment of TGA capped CdTe nps and claim that the high dipole dipole moment of CdTe/TGA is the main driving force of directional aggregation. This dipole-dipole moment interaction of CdTe/TGA nps also supports the idea of our purposed aggregation based mechanism. This explains and supports how two nps come together in our growth mechanism as shown in Figure 8-12(c). Tang *et al* (Tang et al. 2002) also discussed, how it is possible that CdTe nps dissolve and recrystalline again at room temperature after aggregation, due to a low activation energy of phase transition of CdTe. This discussion also explains how is it possible to form a new crystalline structure when two CdTe nps come together in our mechanism (Figure 8-12). However, the aggregation mechanism was mainly accepted only for the formation of nanowires, not as growth mechanism of CdTe nps.

Gaponik *et al* (Gaponik et al. 2002) showed that different stabilizers produce different products, which shows that the stabilizer is the key factor for different particles obtained with the same synthesis method. With 2-mercaptoethanol, there is only one cluster which is called a magic cluster $[\text{Cd}_{54}\text{Te}_{32}(\text{SCH}_2\text{CH}_2\text{OH})_{32}]^{8-}$. Therefore, stabilizer 2-mercaptoethanol prevents aggregation mechanism, all mechanism that is shown in Figure 8-12 stops after magic cluster formation step. This also shows that hydrolysis of TGA is the key factor that affects and initiates the aggregation mechanism in our case. This supports our mechanism of TGA hydrolysis and intermediate particle formation. There are also various publications that studied the ligand effect on synthesis. Zhang *et al* (Zhang et al. 2008), studied the product dependence of CdTe synthesis due to pH used and at different salt concentrations. They show

that the ionic strength and pH of the solution affect rate of synthesis due to a change of the nature of ligand, which changes the electronic repulsive forces between particles. Wang *et al* (Wang et al. 2009), investigated the ligand effect on growth process of CdTe nps. They have developed a new method with sodium-citrate-assisted preparation of aqueous CdTe nanoparticles. They also theoretically simulate the nanoparticle growth dependence on the ligand used, which shows that the nature of the ligand affects the growth mechanism. Simulations also showed that the ligand modification changes the activation energy of nanoparticles, to form a transition complex, which affects the growth rate of CdTe nps. This simulation also supports our final mechanism (b part of Figure 8-12), which shows the formation of intermediate product.

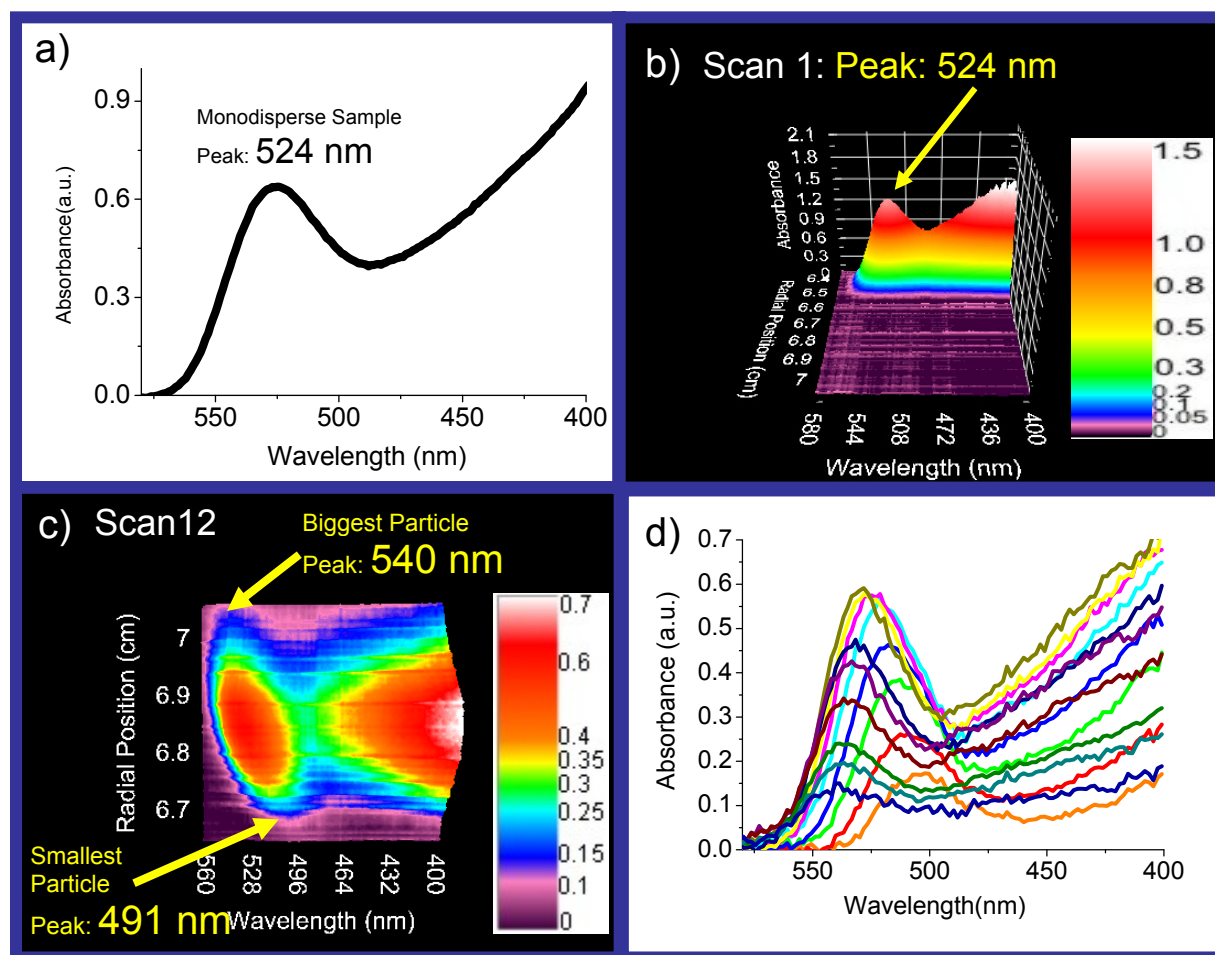


Figure 8-13: Raw MWL-AUC data of monodisperse sample

(a) UV/Vis spectra of monodisperse sample before MWL-AUC; (b) 1st scan of MWL-AUC data of the monodisperse sample; (c) 12th scan of MWL-AUC with monodisperse sample; (d) 15 selected different spectra among 80, taken from different radial positions of the 12th scan in Figure 8-13.c., clearly showing different peak positions.

8.3. Monodisperse TGA-capped CdTe nanocrystals

Monodisperse TGA-capped CdTe nanocrystals are synthesized as explained in the appendix. It is of interest whether monodisperse samples, which were synthesized, consist of a single particle species or not. We therefore subjected monodisperse samples to MWL-AUC.

8.3.1. Results and Discussion

8.3.1.1. Raw MWL-AUC of a monodisperse sample

The UV/Vis spectrum of a monodisperse CdTe nanoparticle is shown in Figure 8-13.a with a peak position of 524 nm. The 1st scan of MWL-AUC data on this sample also shows the identical spectrum with a peak of 524 nm. This is the first scan after sample is transferred to the sample column, in which fractionation has just started. Scan 12 of MWL-AUC is shown in Figure 8-13.c. which is the last scan before the start of pelleting the sample to bottom of the cell. In scan 12, monodisperse sample was clearly fractionated. A band gap shift was observed even in monodisperse sample as shown in the Figure 8-13(d). These figures prove that MWL-AUC can differentiate even in so far assumed monodisperse CdTe nanoparticles. MWL-AUC proves that these particles are not exactly monodisperse and include different particles. The biggest particle has a wavelength position of 540nm and the smallest particle has a wavelength 491 nm. MWL-AUC captured 80 different spectra between 491 nm to 540 nm. 15 spectra among these 80 spectra are shown in Figure 8-13(d), which clearly shows - spectrum at Figure 8-13(a) consist of different spectra.

8.3.1.2. Determination of CdTe mixture composition by spectrum of the sample

Spectral deconvolution is a method for the determination of the concentrations of the individual components in a mixture via simple UV/Vis spectra. As we found that the CdTe particles that are during growth are always of the same size, in this kind of synthesis of CdTe nanoparticles, we can also use the spectral deconvolution of the UV/Vis spectra of any CdTe spectra. Therefore, concentrations of each species can be obtained with this method from a simple

UV/Vis spectrum of the mixture followed by spectral deconvolution with reasonable accuracy. Figure 8-14.a shows the initial spectrum of the monodisperse CdTe nanoparticle.

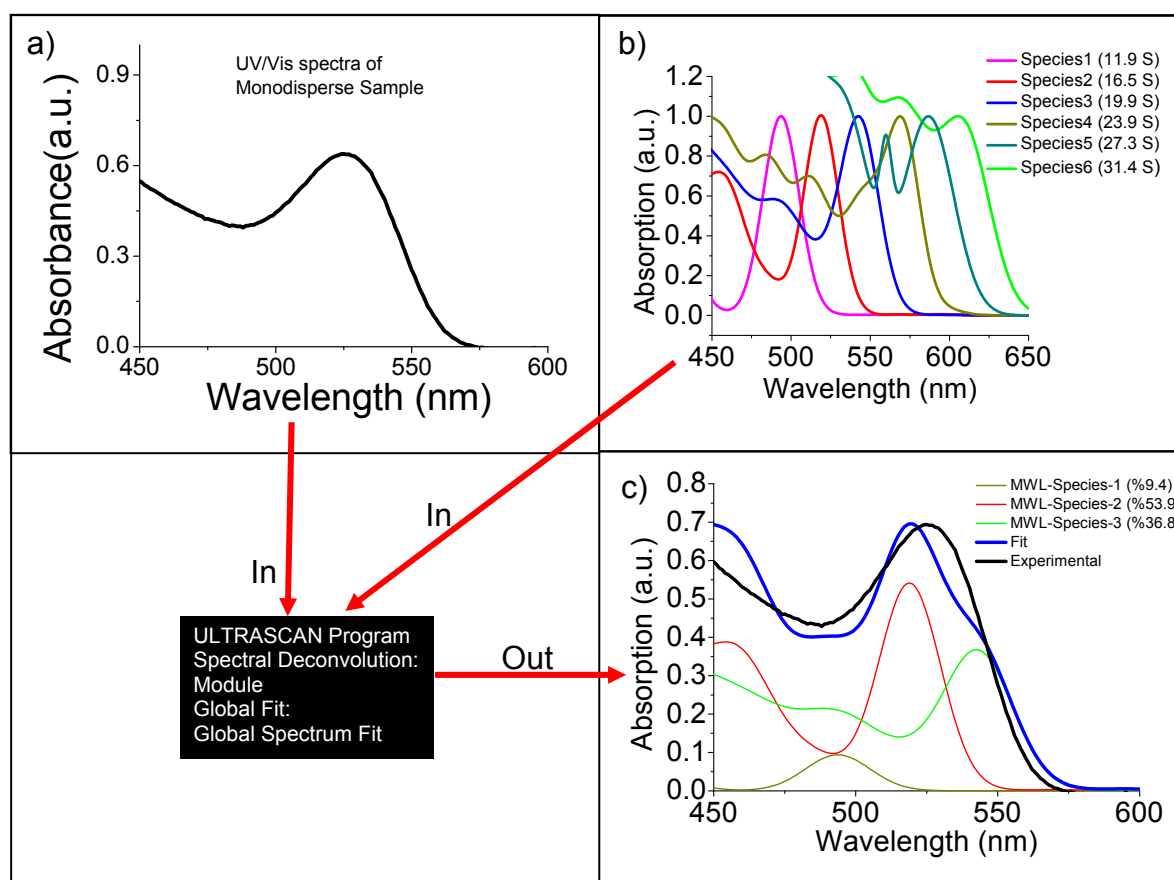


Figure 8-14: Spectral deconvolution of monodisperse CdTe sample

a) UV/Vis spectrum of monodisperse CdTe nanoparticle; b) UV/Vis spectra of 1-6 species; c) Result of spectral deconvolution calculated with Ultrascan Software Global Fit: Global Spectrum; calculation gives 9.4%, 53.9% and 36.8% percent of Species 1, 2 and 3 (Figure 8-14.b). The calculation of the species changes for every wavelength. Hence Figure 8-14.c also shows the particle concentrations at 524 nm wavelength. At 524 nm concentrations are 0.04%, 73% and 26% for Species1, 2 and 3.

8.3.1.3. Comparison of MWL-AUC results and Spectral Deconvolution results

Comparison of spectral decomposition and MWL-raw data is shown in Figure 8-15. Spectral decomposition shows that there are 3 species included in the spectra, whose peak positions are 494, 519 and 542 nm with a relative ratio of 9.4%, 53.9% and 36.8%. Spectral decomposition module has only used single UV/Vis spectra of the sample. In the right side of Figure 8-15, the 12th scan is shown, which is taken after 15 minutes at 60 Krpm. In the raw MWL-AUC data is shown that sample is not monodisperse and includes particles whose peaks change from 491nm and 540 nm.

This proves the spectral decomposition correctly determined the peaks of the sample, even the raw data shows the same range. MWL-AUC determined the nature of the growth mechanism. Furthermore, MWL-AUC determined that there are always identical particles formed in different syntheses. This opened up the possibility of determining the particle composition with using only single UV/Vis spectra of sample. Figure 8-15 proves that.

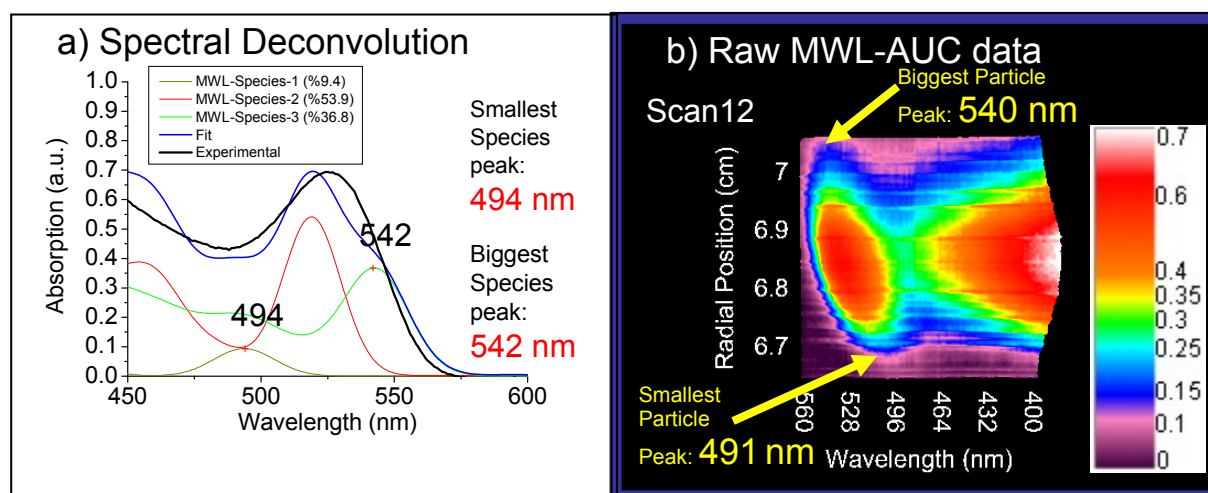


Figure 8-15: Comparison of Spectra deconvolution result and raw MWL-AUC results

a) Spectral deconvolution showing the peak position of smallest and largest particles which shows 494 nm peak for smallest particle and 542 nm peak for biggest particles; b) Scan 12 of MWL-AUC data (Figure 8-13.c); MWL data shows that the biggest particle has a peak of 540 nm and the smallest particle has a peak of 491 nm.

Chapter 9 : Conclusion

A prototype Static Light Scattering Detector for the analytical ultracentrifuge (SLS-AUC) was constructed. The detector consists of a large area avalanche photodiode (LAAPD) and a solid-state red laser. This system replaces the interference detector of the Optima XL-I. Successful raw data measurements were taken for latex particles. Our prototype is fast, and adaptable to the Optima XL-I. However, protein BSA could not be detected with this setup. This shows the limitation of its sensitivity. It is concluded that further improvement of the laser is needed. A new green laser to be tested was ordered for this purpose.

First prototype of the CCD-C-AUC has been developed. It has been proven to be rapid, sensitive, having high resolution and adaptable to the Optima XL-I. The prototype CCD-C-AUC is capable of gaining the absorbance of a real sample cell at all radial positions within the time constraints of the working AUC. We are very pleased to have finalized the pre-construction stage of this detector.

The new generation MWL-AUC is developed, whose performance is comparable or already superior to the Optima XL-I, currently the only ultracentrifuge commercially available. This is remarkable, as the MWL-AUC is still very much an experimental prototype and the Optima XL-I is a finished product, for which clear specifications exist. Again, this can be taken as an indication that we are only starting to gain glimpses of the speed, accuracy, resolution and precision that will be possible with an optimized version of our design. It should be pointed out that this increased performance does not come at a higher price. It is estimated the total investment in an MWL machine to be about half the cost of purchasing an Optima XL-I. As the design of the MWL-AUC is such that other detectors can be accommodated as well, a cheap, precise and multidetector analytical ultracentrifuge appears within reach. Also, each XL-I can be reversibly transferred to a MWL machine. The more serious limitations of the current design are the absence of flash-to-flash-normalization, which would increase the baseline accuracy of the absorbance readings at low degrees of averaging, and the reliance on software for multiplexing the flash lamp. In our hands, this has proven to be extremely sensitive to minor flaws in cables, insulations, soldering, etc. A computer-independent hardware trigger is very much desired. Chromatic aberration is still an issue which should be dealt with in future developments by the application of mirror optics.

From a practical point of view, however, as the radial resolution already achievable is equal or superior to the Optima XL-I, this should not hinder the first experiments already taking advantage of the increased information available with the MWL-AUC. It should also encourage other users of the centrifuge to start building their own MWL-AUCs as it is a modular system, which can be easily adapted to any of the Beckman XL ultracentrifuges and probably also many older machines. Ideally the new users can contribute their ideas and practical experiences to the development process and therefore make it available to the scientific community.

For the analysis of proteins, MWL-AUC is so far only partly successful, as their s-distribution was artificially broadened even with single wavelength data that are taken from the multiwavelength data of MWL-AUC. Single wavelength data of MWL-AUC is shown to be noisier than the single- wavelength data in the UV region in the Optima XL-I due to low intensity of MWL-AUC in this region. The noise level of MWL-AUC data prevents the usage of the spectral decomposition module of Sedphat which is a highly noise-affected method (Balbo et al. 2005). Low intensity of reference light is the main source of noise which prevents the usage of the spectral decomposition module of Sedphat, but it does not affect the usage of $c(s)$ and other analysis.

Industrial β -carotene-gelatin composite particles are a highly heterogeneous system, both in particle size and chemical composition. Fractionation of this mixture in MWL-AUC makes it possible to resolve individual components in the mixture and detect compositional changes in an experiment which takes only one hour. This proves the power of MWL-AUC as a direct technique that can differentiate particles with respect to size and UV/Vis spectra. Although our current analysis does not make it possible unambiguously to assign the spectra to defined particles, as the particle density, swelling, composition and size may be varying simultaneously, the presented multiwavelength analysis allows insights into this complex system which were not previously possible using other techniques. We do not evaluate further the directly experimentally determined sedimentation coefficients as, for our sample, in addition to the above mentioned polydispersity, pH effects as well as charge interactions between the colloids also have to be taken into account.

Despite these restrictions, we have shown the existence of H aggregates inside a sample that was previously known as J aggregate, and detected spectral changes of different H-aggregate

populations as well as changes in the electronic potential energy surfaces of different hybrid particles. We restricted ourselves to a semi-quantitative evaluation based on simple model-free transformations of the data of one out of 40 scans without any prior knowledge. Clearly, even richer phenomena can potentially be discovered with a global evaluation of the entire dataset.

For CdTe nanoparticles, we have described a novel AUC technique allowing for the direct experimental determination of the particle size dependence of optical and electronic properties of CdTe semiconductor nanoparticles with atomic resolution. Furthermore, the method determined the growth mechanism of CdTe/TGA nps. In addition, the particle size distribution could be resolved hydrodynamically with Angström resolution together with the UV-Vis spectra of the monodisperse species. Also continuous determination of band gap dependence on particle size can be obtained. As the spectra of the individual components are additive, this now makes it possible to determine the composition of CdTe mixtures by a simple measurement of a UV-Vis spectrum and fitting to the concentration of individual species. We need to show this by fitting the individual spectra to sums of Gaussians and then fit the sums to the composite spectrum. From the high resolution particle size distribution, the growth mechanism via coalescence of $[\text{Cd}_{54}\text{Te}_{32}(\text{SR})_{52}]^{8-}$ clusters could be revealed. Two-dimensional spectrum analysis also showed that all CdTe nanoparticles are spherical in good agreement with TEM data (Rogach et al. 2007). The presented technique is universally applicable with very high resolution and adaptable to any system which shows particle-size dependent optical properties. This is a significant advance, as MWL-AUC separates and characterizes nanoparticles with Angström resolution (Cölfen and Pauck 1997) down to particle sizes < 1 nm (Cölfen et al. 2002). It works directly in dispersion, has a very high statistical accuracy as every nanoparticle is detected, has no principal solvent restrictions, needs a very low amount of sample (15 μl) and does not require prior sample fractionation (in fact, it even works better with polydisperse samples as this gives a broader data range, thus reducing the synthetic requirements for analysis). Furthermore, MWL-AUC showed that monodisperse sample is not really monodisperse and includes discrete species. Additionally it is fast, with typical experimental times of less than one hour. Within the same time span, standard multi-hole rotors can analyze up to three colloidal mixtures with the same accuracy in parallel, and seven mixtures are envisaged for parallel experiments in the future using an eight-hole rotor. The described capabilities of our new AUC technique are a major

breakthrough for the analysis of small nanoparticles, as highly resolved particle size distributions allow conclusions about the nanoparticle growth mechanism (Cölfen and Pauck 1997; Cölfen et al. 2002), which is important knowledge for rational synthesis design. Therefore, application of our technique to a large number of different nanoparticle systems can be envisaged.

Further reflections, MWL-AUC can be used to detect interactions of biopolymers (proteins-DNA, protein-protein etc), size dependent colloid properties. MWL-AUC can also be used as multi-sensitive turbidity detector as scattered intensity (I) is proportional to $1 / \lambda^4$ (λ is the wavelength of the light).

CCD-C-AUC can detect crystallization reactions faster than cyclotron detection systems. Because cyclotron detector systems have time resolution of 50 ms (Bolze et al. 2002), while CCD-C-AUC detector can detect a signal in the interval of 2 ms.

Future of AUC looks brilliant after announcement of Open AUC project. Open AUC project is a combined project of all groups that are working on development of AUC. New machine will have an open architecture, hardware standards and application interfaces for detector developments. Software will be modular and open source so that everyone can improve the control software by his or her own. In the future AUC will be modular based, so every user will be able to adapt a detector to AUC, leading to their particular need. New technologies would be easy to adapt with Open AUC project.

APPENDIX

Material and Methods of Protein Mixture

This work is a partial recapitulation of a study published earlier (Balbo et al. 2005). The mentioned gel-filtration standard kit has been discontinued by the manufacturer. Therefore, BSA, IgG and rabbit muscle aldolase were purchased as individual components in lyophilised form from SigmaAldrich. Single protein solutions were prepared by weighting the desired protein amount and dissolving it in phosphate buffered saline (PBS) and used without further manipulation. Protein concentrations were 1.5 mg/mL for BSA, 0.45 mg/mL for IgG and 1.5 mg/mL for aldolase and were chosen such that the stock solutions yielded an OD280 nm of around 1 in the standard 12 mm optical path length centerpieces used for AUC. A mixture of these three proteins was prepared by mixing the stock solutions to equal volume and hence signal fractions, based on OD280 nm. Single proteins were examined undiluted and at 1:3 dilutions to mimic the signal amplitude in the mixed sample. A quantity of 400 μ L of the solution and buffer were filled in the sample and reference sector of 12 mm, double-sector Ti centerpieces (Nanolytics, Potsdam, Germany) and capped with sapphire windows. Experiments were simultaneously performed in a Beckman Coulter Optima XL-I and the prototype MWL-AUC described earlier (Strauss et al. 2008) at 25 °C and 40,000 rpm on the same solution to ensure comparability of the results. For the XL-I, sedimentation traces were acquired at 250 nm, 280 nm and with the interference optics simultaneously. Wavelength spectra were recorded from 230 to 350 nm with a nominal wavelength resolution of 1 nm and five replicates for every datum point. Data from the MWL-AUC were saved over the same wavelength range. Individual data files were created for wavelengths of 260, 270 and 280 nm by the data acquisition software. Absorption data were acquired as fast as the respective instrument would allow with a radial increment of 0.003 cm. Data were analyzed with Sedfit or Sedphat. A confidence level of 0.9 was used for Thikonov-Phillips regularization.

Multi-wavelength analytical ultracentrifugation (MWL-AUC) method of β -carotene microparticle system

A Multiwavelength AUC as described in (Bhattacharyya et al. 2006; Strauss et al. 2008) was used at 25 °C. We applied a band centrifugation experiment using a Vinograd cell. In contrast to conventional sedimentation velocity experiments, where the sample between the boundary and the bottom of the cell is only diluted by radial dilution, in band centrifugation the sample is diluted additionally by fractionation in the pure solvent. The reservoir is filled with a small amount of the concentrated sample. Column and sample sectors are filled with D₂O with a density which is higher than that of the sample solution and lower than the density of the dispersed solute. We prepared a 20 g/l solution and deposited 15 microliters of the solution into the cell reservoir. After preliminary experiments, this concentration was chosen to ensure that the individual components of the mixture are detected in as many scans as possible with ODs < 1.4 in the experiment without too much dilution, which might cause noisy data.

After cell assembly, the AUC was accelerated to 5000 rpm for three minutes to transfer the sample in the reservoir via capillaries to overlay the D₂O column. Afterwards, the speed was increased to 55,000 rpm. Forty scans were taken with a time interval of 90 seconds and a radial step size of 50 μ m to observe the full sedimentation of the sample. The selected wavelength range was from 250 nm to 750 nm. In the prototype setup, we apply the spectrum acquired for an empty cell as a reference for the calculation of the absorption leading to a baseline offset of 0.05 OD (see Figure 7-3(a)) After the experiment, while cleaning the cell, we saw some precipitate in the cell reservoir. Thus, not all particles were transferred to the sample column, but some large particles remained in the reservoir as they must have completely sedimented already upon speeding up the rotor to 5000 rpm.

Each of the 40 scans produces a three-dimensional graph. We have radial position as x-dimension, wavelength as y-dimension and absorbance as z-dimension. In the present contribution, we will perform a semi-quantitative evaluation based on simple model-free transformations of the data without any prior knowledge.

For evaluation, we have converted the radial position (r) to the sedimentation coefficient s by using Equation 8-1.

The 3D absorption dataset can now be projected either onto the wavelength or the sedimentation coefficient axis to visualize better the spectral changes with different sedimentation coefficients or sedimentation coefficient distributions at different wavelengths.

Synthesis of TGA-capped CdTe nanocrystals and sample preparation for AUC

CdTe samples were obtained from Professor Dr. Alexander Eychmüller's group at Dresden Technical University. They were prepared using a technique previously reported (Gaponik et al. 2002). Thioglycolic acid (TGA) was used as the stabilizer. The molar ratio of $\text{Cd}^{2+}/\text{Te}^{2-}/\text{TGA}$ was 1/0.5/1.3, and pH of the synthetic mixture was adjusted to 12 (Shavel et al. 2006). The nucleation and growth of the nanocrystals proceeded by refluxing at 100 °C under open-air conditions. The particle size was controlled by the reflux time. The as-prepared colloids underwent post-preparative size-selective precipitation according to the procedure described (Gaponik et al. 2002). The method consists of the gradual precipitation of the NCs (nanocrystals) induced by setwise addition of a non-solvent (2-propanol) into a preliminary concentrated CdTe nanoparticle solution. This technique allows separation of the initial colloid into several fractions of nanoparticles having narrowed size distributions.

Ultracentrifuge Method of CdTe/TGA system

A solution of 15 µl CdTe was filled into the reservoir of a Vinograd zone centrifugation cell (Figure 2-4(e)). The sample column was filled with 270 µl of D_2O , the reference column with 290 µl. The experiments were performed at 25 °C on the modified Beckman Optima XL-80 K centrifuge (Beckman Coulter, Palo Alto, California) equipped with a multiwavelength detector, as described in (Strauss et al. 2008). The experiment was started with a speed of 4000 rpm for 3 minutes in order to layer the sample in the reservoir onto the D_2O in the sample column. Then the speed was increased to 55,000 rpm. 20 radial scans with 50 µm step size were taken at intervals of 1.5 min.

ABBREVIATIONS

2DSA	2 dimensional spectrum analysis
AD/DA	Analog to digital / digital to analog
APD	Avalanche photodiode
ASTFEM-RA	Adaptive Space-Time Finite Element Method - Reversible Associations
AUC	Analytical Ultracentrifuge
BSA	Bovine Serum Albumin
CCD	Charge-coupled device
CCD-C-AUC	CCD camera UV/Vis absorption detector for AUC
CdTe	Cadmium Telluride
FOQELS	Fiber-optic quasi-classical light scattering
HDA	Hexadecylamine
HPA	Hexylphosphonic acid
IgG	Agarose
LAAPD	Large area avalanche photodiode
LS	Light scattering
MWL	Multiwavelength
MWL-AUC	Multiwavelength detector for AUC
OD	Optical density
PBS	Phosphate buffered saline
PMT	Photomultiplier tube
SEC	Size exclusion chromatography
SDS	Sodium dodecyl sulfate polyacrylamide gel electrophoresis
SLS-AUC	Static light scattering detector for AUC
TGA	Thioglycolic acid
TOPO	Trioctylphosphine oxide
UV/Vis	Static light scattering detector for AUC

REFERENCES

- Alivisatos AP (1996) Semiconductor clusters, nanocrystals and quantum dots. *Science* 271:933-937
- Auweter H, Haberkorn H, Heckmann W, Horn D, Luddecke E, Rieger J, Weiss H (1999) Supramolecular structure of precipitated nanosize beta-carotene particles. *Angewandte Chemie-International Edition* 38:2188-2191
- AvivBiomedical (2008) The first commercially available fluorescence detector for analytical ultracentrifuges, Web page of Aviv Biomedical Company www.avivbiomedical.com
- Balbo A, Minor KH, Velikovsky CA, Mariuzza RA, Peterson CB, Schuck P (2005) Studying multiprotein complexes by multisignal sedimentation velocity analytical ultracentrifugation. *Proceedings of the National Academy of Sciences of the United States of America* 102:81-86
- Beams JW, Dixon HMI (1953) An ultracentrifuge double cell. *Review of Scientific Instruments* 24:228
- BeckmanCoulter (1991) XL-A manual, Fullerton, USA
- Bhattacharyya SK (2006) Development of detector for analytical ultracentrifuge. Max Planck Institutes of Colloids and Interfaces, vol PhD. Potsdam University, Potsdam
- Bhattacharyya SK, Maciejewska P, Börger L, Stadler M, Gülsun AM, Cicek HB, Cölfen H (2006) Development of a fast fiber based UV-Vis multiwavelength detector for an ultracentrifuge. *Progress in Colloid and Polymer Science, Analytical Ultracentrifugation VIII* 131:9-22
- Bolze J, Peng B, Dingenouts N, Panine P, Narayanan T, Ballauff M (2002) Formation and growth of amorphous colloidal CaCO_3 precursor particles as detected by time-resolved SAXS. *Langmuir* 18:8364-8369
- Börger L (2000) Biomimetische mineralisationsprozesse und deren charakterisierung. Wissenschaftsdisziplin Physikalische Chemie, vol PhD. Univesitat Potsdam, Potsdam
- Börger L, Cölfen H, Antonietti M (2000) Synthetic boundary crystallization ultracentrifugation: a new method for the observation of nucleation and growth of inorganic colloids and the determination of stabilizer efficiencies. *Colloids and Surfaces A:Physicochemical and Engineering Aspects* 163:29-38
- Brookes E, Demeler B (2005) Genetic algorithm optimization for obtaining accurate molecular weight distributions from sedimentation velocity experiments. In: Wandrey C, Cölfen H (eds) 14th International Symposium on Analytical Ultracentrifugation. Springer-Verlag Berlin, Lausanne, Switzerland, pp 33-40
- Brookes E, Demeler B (2008) Paralel computational techniques for the analysis of sedimentation velocity experiments in Ultrascan. *Colloid & Polymer Science* 286:138-148
- Brookes EH, Boppana RV, Demeler B (2006) Computing large sparse multivariate optimization problems with an application in biophysics. Conference on High Performance Networking and Computing Proceedings of the 2006 ACM/IEEE conference on Supercomputing ACM 0-7695-2700-0/06
- Brown PH, Schuck P (2006) Macromolecular size and shape distributions by sedimentation velocity analytical ultracentrifugation. *Biophysical Journal* 90:4651-4661
- Cao WM, Demeler B (2008) Modeling analytical ultracentrifugation experiments with an adaptive space-time finite element solution for multicomponent reacting systems. *Biophysical Journal* 95:54-65
- Cölfen H, Antonietti M (2008) Mesocrystals and nonclassical crystallization. John Wiley & Sons Ltd., West Sussex

- Cölfen H, Pauck T (1997) Determination of particle size distributions with angstrom resolution. *Colloid and Polymer Science* 275:175-180
- Cölfen H, Pauck T, Antonietti M (1997) Investigation of quantum size colloids using the XL-I ultracentrifuge. *Progress in Colloid and Polymer Science, Analytical Ultracentrifugation IV*, vol 107, pp 136-147
- Cölfen H, Schnablegger H, Fischer A, Jentoft FC, Weinberg G, Schlogl R (2002) Particle growth kinetics in zirconium sulfate aqueous solutions followed by dynamic light scattering and analytical ultracentrifugation: Implications for thin film deposition. *Langmuir* 18:3500-3509
- Dagtepe P, Chikan V (2008) Effect of Cd/Te ratio on the formation of CdTe magic-sized quantum dots during aggregation. *Journal of Physical Chemistry A* 112:9304-9311
- Dagtepe P, Chikan V, Jasinski J, Leppert VJ (2007) Quantized growth of CdTe quantum dots; Observation of magic-sized CdTe quantum dots. *Journal of Physical Chemistry C* 111:14977-14983
- Demeler B (2005) UltraScan: A comprehensive data analysis software package for analytical ultracentrifugation experiments. In: Scott DJ, Harding SE, Rowe AJ (eds) *Modern Analytical Ultracentrifugation: Techniques and Methods*. Royal Society of Chemistry, Cambridge, pp 210-229
- Demeler B, Brookes E (2008) Monte carlo analysis of sedimentation experiments. *Colloid & Polymer Science* 286:139-137
- Demeler B, van Holde KE (2004) Sedimentation velocity analysis of highly heterogeneous systems. *Analytical Biochemistry* 335:279-288
- Eychmüller A (2000) Structure and photophysics of semiconductor nanocrystals. *Journal of Physical Chemistry B* 104:6514-6528
- Gaponik N, Talapin DV, Rogach AL, Hoppe K, Shevchenko EV, Kornowski A, Eychmüller A, Weller H (2002) Thiol-capping of CdTe nanocrystals: An alternative to organometallic synthetic routes. *Journal of Physical Chemistry B* 106:7177-7185
- Giebel R (1992) The Optima XL-A: A new analytical ultracentrifuge with a novel precision absorption optical system. In: Harding SE, Rowe AJ, Horton J (eds) *Analytical ultracentrifugation in biochemistry and polymer science*. Royal Society of Chemistry, Cambridge, pp 16-25
- Hamamatsu (2006) User Manual of Compact 5-Watt Xenon Flash Lamp Module; L9456. In: Hamamatsu (ed), Iwata city
- Herron N, Calabrese JC, Farneth WE, Wang Y (1993) Crystal-structure and optical-properties of $\text{Cd}_{32}\text{S}_{14}(\text{SC}_6\text{H}_5)_{36}\text{DMF}_4$, a cluster with a 15-angstrom CdS core. *Science* 259:1426-1428
- Kegeles G (1952) A boundary forming technique for the ultracentrifuge. *Journal of the American Chemical Society* 74:5532
- Kim H, Deonier RC, Williams JW (1977) Investigation of self-association reactions by equilibrium ultracentrifugation. *Chemical Reviews* 77:659-690
- Lamm O (1929) Theory and methods of ultra-centrifuging. *Zeitschrift für Physikalische Chemie* 143; 21 B:177; 1-190; 4
- Laue TM (1996) Choosing which optical system of the optima™ XL-I analytical ultracentrifuge to use. Beckman Instruments Inc, Fullerton
- Lavrenko P, Lavrenko V, Tsvetkov V (1999) Shift interferometry in analytical ultracentrifugation of polymer solutions. In: Cölfen H (ed) *11th Symposium on Analytical Ultracentrifugation*. Springer-Verlag Berlin, Potsdam, Germany, pp 14-22
- Lloyd PH (1974) *Optical methods in ultracentrifugation, electrophoresis and diffusion: with a guide to the interpretation of records*. Clarendon Press, Oxford

- MacGregor IK, Anderson AL, Laue TM (2004) Fluorescence detection for the XLI analytical ultracentrifuge. *Biophysical Chemistry* 108:165-185
- Mächtle W (1984) Charakterisierung von disperisionen durch gekopplete H₂O/D₂O-ultrazentrifugenmessungen. *Macromol Chem* 185:1025
- Mächtle W (1992) Analysis of polymer dispersions with an eightcell-auc-multiplexer: high resolution particle size distributions and density gradient techniques. In: Harding SE, Rowe AJ, Horton J (eds) *Analytical Ultracentrifugation in Biochemistry and Polymer Science*. Royal Society of Chemistry, Cambridge, pp 147-175
- Mächtle W (1999a) High-resolution, submicron particle size distribution analysis using gravitational-sweep sedimentation. *Biophysical Journal* 76:1080-1091
- Mächtle W (1999b) The installation of an eight-cell Schlieren optics multiplexer in a Beckman Optima XLI/XL analytical ultracentrifuge used to measure steep refractive index gradients. *Progress in Colloid and Polymer Science* 113:1 - 9
- Mächtle W, Börger L (2006) *Analytical ultracentrifugation of polymers and nanoparticles*. Springer, Berlin
- Medelson M, Stahl FW (1958) The replication of DNA in Escherichia Coli. *Proceedings of the National Academy of Sciences* 44:671-682
- Michalet X, Pinaud FF, Bentolila LA, Tsay JM, Doose S, Li JJ, Sundaresan G, Wu AM, Gambhir SS, Weiss S (2005) Quantum dots for live cells, in vivo imaging, and diagnostics. *Science* 307:538-544
- Müller HG (1989) Automated determination of particle-size distributions of dispersions by analytical ultracentrifugation. *Colloid and Polymer Science* 267:1113-1116
- Murray CB, Norris DJ, Bawendi MG (1993) Synthesis and characterization of nearly monodisperse CdE (E = S, Se, Te) semiconductor nanocrystallites. *Journal of the American Chemical Society* 115:8706-8715
- Niederberger M, Garnweitner G, Krumeich F, Nesper R, Cölfen H, Antonietti M (2004) Tailoring the surface and solubility properties of nanocrystalline titania by a nonaqueous in situ functionalization process. *Chemistry of Materials* 16:1202-1208
- OceanOptics (2008) Choosing a Grating & Wavelength Range: "USB" Optical Bench; http://www.oceanoptics.com/Products/bench_grating_usb.asp
- Planken KL (2008) *Analytical ultracentrifugation of inorganic colloids; sedimentation velocity of interacting and non-interacting particles*, vol PhD. Universitei Utrecht, pp 166
- Polivka T, Sundstrom V (2004) Ultrafast dynamics of carotenoid excited states - From solution to natural and artificial systems. *Chemical Reviews* 104:2021-2071
- Ralston G (1993) *Introduction to analytical ultracentrifugation*. Beckman, California
- Rockenberger J, Troger L, Rogach AL, Tischer M, Grundmann M, Eychmüller A, Weller H (1998) The contribution of particle core and surface to strain, disorder and vibrations in thiolcapped CdTe nanocrystals. *Journal of Chemical Physics* 108:7807-7815
- Rogach AL, Franzl T, Klar TA, Feldmann J, Gaponik N, Lesnyak V, Shavel A, Eychmüller A, Rakovich YP, Donegan JF (2007) Aqueous synthesis of thiol-capped CdTe nanocrystals: State-of-the-art. *Journal of Physical Chemistry C* 111:14628-14637
- Rogach AL, Katsikas L, Kornowski A, Su DS, Eychmüller A, Weller H (1996) Synthesis and characterization of thiol-stabilized CdTe nanocrystals. *Berichte Der Bunsen Gesellschaft Physical Chemistry Chemical Physics* 100:1772-1778
- Schachman HK (1992) Is there a future for the ultracentrifuge? In: Harding SE, Rowe AJ, Horton J (eds) *Analytical ultracentrifugation in biochemistry and polymer science*. Royal Society of Chemistry, Cambridge, pp 3-31
- Schmidt B, Riesner B (1992) A fluorescence detection system for the analytical ultracentrifuge and its applicaton to proteins, nucleic acids, viroids and viruses. In:

- Harding SE, Rowe AJ, Horton J (eds) Analytical Ultracentrifugation in Biochemistry and Polymer Science. Royal Society of Chemistry, Cambridge, pp 176-207
- Scholtan W, Lange H (1972) Determination of particle size distribution of latices with ultracentrifuges. *Kolloid Zeitschrift und Zeitschrift Fur Polymere* 250:782
- Schuck P (1998) Sedimentation analysis of noninteracting and self-associating solutes using numerical solutions to the Lamm equation. *Biophysical Journal* 75:1503-1512
- Schuck P (2000) Size-distribution analysis of macromolecules by sedimentation velocity ultracentrifugation and Lamm equation modeling. *Biophysical Journal* 78:1606-1619
- Shavel A, Gaponik N, Eychmüller A (2006) Factors governing the quality of aqueous CdTe nanocrystals: Calculations and experiment. *Journal of Physical Chemistry B* 110:19280-19284
- SpinAnalytical (2008) <http://www.spinanalytical.com/Centerpieces.html?mode=preview>. Spin Analytical, Durham
- Stafford WF (1992) Boundary Analysis in sedimentation transport experiments - A procedure for obtaining sedimentation coefficient distributions using the time derivative of the concentration profile. *Analytical Biochemistry* 203:295-301
- Stafford WF, Sherwood PJ (2004) Analysis of heterologous interacting systems by sedimentation velocity: curve fitting algorithms for estimation of sedimentation coefficients, equilibrium and kinetic constants. *Biophysical Chemistry* 108:231-243
- Strauss HM, Karabudak E, Bhattacharyya S, Kretzschmar A, Wohlleben W, Colfen H (2008) Performance of a fast fiber based UV/Vis multiwavelength detector for the analytical ultracentrifuge. *Colloid and Polymer Science* 286:121-128
- Svedberg T (1926) Nobel Lecture; http://nobelprize.org/nobel_prizes/chemistry/laureates/1926/svedberg-lecture.pdf
- Svedberg T, Nichols JB (1923) Determination of size and distribution of size of particle by centrifugal methods. *Journal of the American Chemical Society* 45:2910-2917
- Svedberg T, Pederson KO (1940) *The Ultracentrifuge*. Clarendon Press, Oxford
- Tang ZY, Kotov NA, Giersig M (2002) Spontaneous organization of single CdTe nanoparticles into luminescent nanowires. *Science* 297:237-240
- Vinograd J, Bruner R, Kent R, Weigle J (1963) Band-centrifugation of macromolecules and viruses in self-generating density gradients. *Proceedings of the National Academy of Sciences* 49:902-910
- Vistica J, Dam J, Balbo A, Yikilmaz E, Mariuzza RA, Rouault TA, Schuck P (2004) Sedimentation equilibrium analysis of protein interactions with global implicit mass conservation constraints and systematic noise decomposition. *Analytical Biochemistry* 326:234-256
- Vossmeyer T, Reck G, Katsikas L, Haupt ETK, Schulz B, Weller H (1995a) A double diamond superlattice built up of $\text{Cd}_{17}\text{S}_4(\text{SCH}_2\text{CH}_2\text{OH})_{(26)}$ clusters. *Science* 267:1476-1479
- Vossmeyer T, Reck G, Schulz B, Katsikas L, Weller H (1995b) Double layer superlattice structure built up of $\text{Cd}_{32}\text{S}_{14}(\text{SCH}_2\text{CH}(\text{OH})\text{CH}_3)_{(36)} \cdot 4\text{H}_2\text{O}$ clusters. *Journal of the American Chemical Society* 117:12881-12882
- Wang CL, Zhang H, Xu SH, Lv N, Liu Y, Li MJ, Sun HZ, Zhang JH, Yang B (2009) sodium-citrate-assisted synthesis of aqueous CdTe nanocrystals: giving new insight into the effect of ligand shell. *Journal of Physical Chemistry C* 113:827-833
- Zhang H, Liu Y, Zhang JH, Wang CL, Li MJ, Yang B (2008) Influence of interparticle electrostatic repulsion in the initial stage of aqueous semiconductor nanocrystal growth. *Journal of Physical Chemistry C* 112:1885-1889

Acknowledgements:

First of all, I would like to thank Prof. Dr. Markus Antonietti, for giving me an opportunity to do my PhD at one of the most prestigious institutes not only in Germany but worldwide.

My supervisor, Dr. habil Helmut Coelfen, is sincerely acknowledged, believing me from the very beginning, correcting the thesis, for numerous both scientific and non-scientific discussions and for his kindness and keeping promises.

I am indebted to Borries Demeler, of the Center for Analytical Ultracentrifugation of Macromolecular Assemblies, Texas, USA, for Ultrascan software, for the fruitful discussions and his valuable comments.

I would like to thank Wendel Wohlleben from BASF AG, BASF SE; for his constant support for the project, and discussions.

Prof. Dr. Tom M. Laue is thanked for the strong discussion about the constant light source and about the detector development.

I would like to thank Dr. Glen Ramsay for his help while setting up the constant light source and Jochen Mentges from LOT-Oriel Europe, for his help while testing a possible light source.

Great gratitude goes to Antje Voelkel; thanks to Antje not only for AUC Measurements but also her numerous scientific comments, very nice ideas and friendship.

I would like to express my sincere gratitude to Holger Strauss of Nanolytics, Potsdam, Germany, for his help in conducting the tests and helping with his experience of earlier designs of MWL-AUC, as well as his great help while doing experiments and analyzing the results with Sedphat.

I would like to thank Emre Brookes, of the Center for Analytical Ultracentrifugation of Macromolecular Assemblies, Texas, USA, for developing the multiwavelength developing module for our data analysis.

Andreas Kretzschmar is thanked for his excellent work during the production of mechanical parts and mechanical constructions.

The excellent work of Hendrik Pitas from the electronic workshop (Max Planck Institute of Colloids and Interfaces) during the whole detector development is sincerely acknowledged.

Prof. Dr. Eychmuller, Dr. Nikoli Gaponik and Dr. Vladimir Lesynak of Dresden Technical University are acknowledged for the synthesis of CdTe nanoparticles.

Arne Stark is thanked for his help while making the setup functional and for the contributions with his knowledge of light scattering.

The companies, Advanced Photonix Inc. and Laser Components, are thanked for modifying the LAAPD power supply for our design.

I would like to thank to my office mates; Denis Gebauer, Ruiqi Song for the friendly and enjoyable working atmosphere.

One big thanks goes to my little Turkish community: Rezan & Mehmet, Emre, Ozlem, Yusuf, Yasemin, Ozgur and Prof. Dr. A. Levent Demirel. And I also would like to thank all my former/present friends and colleagues here at the institute: Antje, Michael, Arne T., Jelena, Farnoosh, Jong, Philipp, Magda, Christine.

I want to express my gratitude to my family, Ayhan Karabudak, Vicdan Karabudak, Levent Karabudak, Tulin Karabudak, who provided continuous understanding, patience, and energy. They enabled the way for my education and allowed me great freedom in deciding my future. Last but not least, I would like to thank Ozlem for her love, support and encouragement which have sustained and uplifted me throughout this thesis.

BASF AG, BASF SE and the Max-Planck Society are also gratefully acknowledged for the financial support of the Multiwavelength Detector project.

List of Publications

This thesis is partly based on the following publications

Published or Accepted Articles:

“The Open AUC Project”, Helmut Cölfen, Thomas N. Laue, Wendel Wohlleben, Kristian Schilling, Engin Karabudak, Bradley W., Langhorst, Emre Brookes, Bruce Dubbs, Dan Zollars, Mattia Rocco, Borries Demeler, (accepted to European Biophysics Journal)

“Investigation of β -Carotene-gelatin composite particles with a Multiwavelength UV/Vis detector for the Analytical Ultracentrifuge”, Engin Karabudak, Wendel Wohlleben, Helmut Cölfen, (accepted to European Biophysics Journal)

“Performance of a fast fiber based UV/Vis multiwavelength detector for analytical *Ultracentrifugation*”, Strauss HM., Karabudak E., Bhattacharyya S., Kretzschmar A., Wohlleben W., Coelfen H. , Colloid and Polymer Science, Volume 286, Issue 2, Pages 121-128, Feb 2008.

Articles to be submitted:

“Determination of semiconductor band gap dependence on particle size with atomic resolution”, Engin Karabudak, Emre Brookes, Holger Strauss, Vladimir Lesnyak, Nikolai Gaponik, Alexander Eychmüller, Wendel Wohlleben, Borries Demeler, and Helmut Cölfen